UNIVERSITÀ
degli STUDI
di CATANIA

Dipartimento
di Fisica
e Astronomia
"Ettore Majorana"

PhD programme in complex systems

Luca Gallo

Coupled dynamical systems in presence of higher-order
interactions

PhD thesis

Supervisors:
Prof. Vito Latora
Prof. Mattia Frasca
Prof. Timoteo Carletti

To all the beautiful people that made this possible.

Acknowledgements

I would like to express my deepest gratitude Professor Vito Latora, for having me taught that how to tell a story is as crucial as the story itself.

I could not have undertaken this journey without Professor Mattia Frasca, the patience and the involvement of whom cannot be expressed by words.

I am deeply indebted to Professor Timoteo Carletti, who have shown me how freeing is doing research for the sake of it.

I would like to acknowledge Professor Jesús Gómez-Gardeñes, and Professor Mario Chavez, for having reviewed this thesis.

I am extremely grateful to Professor Giovanni Russo, with whom working together has been a privilege.

I would like to extend my sincere thanks to Doctor Lucia Valentina Gambuzza, whose help and dedication I have always found fundamental.

I had the pleasure of working with Riccardo Muolo, whose commitment and friendship have been precious since the very first day.

Special thanks to Federico Malizia, whose value as a researcher and as a person is greater than what he believes.

Many thanks to my colleagues at the University of Catania, and in particular to Giulio Giacomo Cantone, Alessandra Corso, Andrea Russo, and Cinzia Tomaselli, the discussion with whom have always been stimulating.

Special thanks to my colleagues at the University of Namur, and in particular to Carolina Charalambous, Jérôme Daquin, Jean-François de Kemmeter, Lorenzo Giambagli, Martin Moriamé, Rémi Pédenon-Orlanducci,

Abstract

In the past decades, many complex systems, either natural, social, or artificial, have been modeled as networks of coupled dynamical systems, with the links describing interactions among couples of units. However, recent evidence shows that various systems are characterized by many-body, group interactions, that cannot be captured by a network description. In the last few years, a vast literature aimed at understanding how these higher-order interactions influence the global behavior of coupled systems has raised. Among other phenomena, the study of synchronization has received a lot of interest. Yet, most of the research focuses on phase oscillators, with the synchronization of nonlinear chaotic oscillators receiving less consideration. Additionally, these studies are restricted to numerical simulations, or provide an analytical solution for simplified cases only. On the other hand, little attention has been given to the investigation of pattern formation in presence of many-body interactions. Particularly, an extension of Turing's instability theory to the case of higher-order networks is still lacking. The objective of this thesis is to fill the existing gaps in the literature, by developing a general theory for studying the collective behavior of coupled dynamical systems in presence of higher-order interactions. We focus on synchronization of chaotic oscillators and on pattern formation in reaction-diffusion systems. We introduce a new formalism to describe coupled dynamics in a general framework, and we demonstrate that it can be used to describe both phenomena under study, enabling the derivation of the necessary conditions for their onset. The results here presented pave the way to further studies

of dynamical systems in presence of many-body interactions.

Contents

Introduction

Many complex systems, either natural or artificial, can be modeled as networks of interacting units [1]. For instance, various technological systems, like power grids [2, 3] or Internet [4], are designed as a network of communicating elements. The human brain itself is ultimately a network of neurons connected by the synapses [5]. Our society can also be modeled as a network, as each of us is involved in a web of relationships of different kinds, with acquaintances, friends, coworkers, and so on [6, 7]. The effectiveness of networks as a tool for modeling complex systems have attracted the scientific community, triggering the interest of researchers across various disciplines, from physics and engineering, to social science and ecology [8, 9, 10].

In many cases, each of the elements constituting a network can be modeled as a dynamical system, whose evolution in time is determined by the interactions with other units. Elucidating how the interplay between the dynamics of the single units, the structure and the form of their interactions shapes the behavior of the system as a whole is a fundamental problem that has important applications in several research fields. In facts, a variety of fascinating and complex phenomena in nature occurs as a collective behavior emerging from the interactions among simple units [11, 12]. From superconductivity [13] to ferromagnetism [14], from bird-flocking [15] to epidemic outbreaks [16], emergence is everywhere [17]. Among various collective phenomena, we will here concentrate on two that are relevant in many applications, namely the *synchronization* of coupled oscillators, and *pattern formation* in networked systems.

Synchronization is a process wherein a system of units, either identical or not, adjust their motion, due to mutual interactions or to external forcing, into a common dynamics [1]. Many natural, social, and artificial systems show a synchronous behavior. A well known example comes from a species of fireflies living in Southeast Asia, whose flashes synchronize, generating a spectacular phenomenon [18]. Human activities also tend to synchronize. From stock market exchanges [19], to pedestrians walking [20], from audience clapping [21], to dancing [22] and music playing [23], synchronization is ubiquitous in human ensembles [24]. In power grids, all units operate at the same frequency, and synchronization is the normal operating condition of the system [25, 26].

Though the first description of synchronization can be traced back to Christiaan Huygens, in the seventeenth century [27], the recent interest in complex networks have encouraged a vast literature on the relationship between the topological characteristics of a coupled system and its dynamical behavior [26]. Synchronization has been investigated in small-world [28], weighted [29], directed [30], temporal [31], multilayer [32], and adaptive networks [33, 34]. Many of these studies focus on the case of *complete* or *general synchronization*, which occurs when each unit of the system asymptotically follows the exact same trajectory [26]. However, other kinds of synchronization have been analyzed, including remote [35, 36], and cluster synchronization [37, 38]. Also, phenomena such as the emergence of chimera [39, 40] and Bellerophon states [41, 42], or the Benjamin–Feir instability [43, 44], have been throughly investigated in complex networks.

In this thesis we will focus on complete synchronization of nonlinear chaotic oscillators. Synchronization of chaos has triggered the interest of researchers for different reasons. First, it is a rich and intriguing phenomenon, as chaotic oscillators may synchronize in various forms [26]. Second, different applications require the synchronization between chaotic systems, such as secure communication of signals, and chaos anticipation [45]. For their nature, chaotic systems would seem to be systems defying synchronization, as two identical *autonomous* oscillators starting at nearly the same initial conditions will follow trajectories that exponentially diverge in time. However, two *interacting* chaotic systems can synchronize, so that their coherent dynamics is stable [46, 47]. To an-

alyze the synchronization of a network of chaotic oscillators, a commonly used approach is that of the Master Stability Function [48]. In a nutshell, this method consists in quantifying the exponential rate at which a perturbation transverse to the so-called *synchronization manifold*, namely the subspace in the phase space where the synchronous trajectory lies, grows in time. If the growth rate is negative, i.e., the perturbation shrinks in time, than the system can achieve synchronization, while a coherent state can not emerge otherwise [48, 49]. This framework will be the main mathematical tool we will rely on in this work.

Another intriguing phenomenon recurring in various natural systems is the presence of patterns. From stripes, rosettes and the spots on the shells and the fur of animals, to bacteria aggregates, from mammalian territory formation, to neural firing, patterns seem to appear all over the place [50]. Understanding how they form is, therefore, a fundamental question in various research fields. In a seminal paper [51], Alan Turing set the mathematical basis of morphogenesis, i.e., the biological process responsible for the development of the shape in cells, tissues, and organisms, discussing a microscopic mechanism to explain how patterns form. The impact of the theory proposed by Turing has been substantial not only in developmental biology, but also in other research fields. Indeedm, it is nowadays considered a paradigmatic model of self-organization [52, 53], with examples ranging from autocatalytic chemical reactions [54, 55, 56], to biological morphogenesis [57, 58, 59, 60, 61], from ecological systems [62, 63] to atomic monolayers [64]. At a glance, Turing's instability mechanism consists in the combined effect of two processes, namely a local *reaction*, coupled with a long-range *diffusion*, involving two species, namely an activator and an inhibitor species [65]. Interestingly, while each process, considered separately, would drive the system to a homogeneous state, the combination of the two allows for a heterogeneous solution, namely for patterns.

Initially developed to study pattern formation in continuous domains, and in 1D and 2D lattices [66], Turing's theory has been recently extended to the case of complex networks, paving the way for novel analyses of the phenomenon [67, 68]. In particular, it has been shown that, whereas the instability mechanism remains essentially the same, the properties of the emergent patterns can be very different. For instance, due to the dis-

crete nature of networks, the spontaneous differentiation of nodes takes place only on a fraction of them [67]. As for synchronization, in later years Turing pattern formation has been investigated in directed [69, 70], non-normal [71], time-varying [72], and multiplex [73, 74] networks. In this thesis we will generalize these results, as well as those on complete synchronization, extending them to the case of *higher-order networks*.

Despite their effectiveness in modeling complex systems, networks have an important limitation. Indeed, they are able to capture pairwise, i.e., two-body, interactions exclusively. However, recent evidences show that various natural and social systems are characterized by *higher-order*, *group interactions*. For instance, in competitive ecological networks, the effect of one competitor on another can depend on the presence of a third species [75]. Another example comes from neuroscience, as it has been shown that pairwise models are not sufficient to describe neuronal dynamics [76, 77, 78]. The co-authorship network itself is inherently higher-order, as it is characterized by group interactions, i.e., the scientific publications, which usually involve more than two authors [79].

Over the last few years, a vast literature aimed at developing novel mathematical frameworks that can naturally encode group interactions has raise. In particular, an increasing research interest for more complex mathematical structures, such as simplicial complexes [80] and hypergraphs [81], has emerged [82, 83]. Recent studies have used these structures to review different dynamical processes, such as epidemic [84] and social contagion [85, 86, 87], random walks [88, 89, 90], consensus [91, 92], in the presence of many-body interactions, finding that they may greatly influence the global behavior of the system. For example, nonlinear higher-order interactions can lead to the emergence of multi-stability among different states, hysteresis loops, and abrupt (explosive) transitions [93, 94]. These findings highlight that higher-order interactions can be the foundational mechanism underlying many natural and social phenomena, such as bistable visual perception [95], epileptic seizures in the brain [96], and critical mass phenomena in the emergence of social convention [97].

This wave of enthusiasm for higher-order interactions has also hit the studies of synchronization and of pattern formation. Concerning the phenomenon of synchronization, it has been shown that multi-body in-

teractions can dramatically affect the collective dynamics of a system of either phase oscillators or chaotic systems [82]. For instance, the Kuramoto model [98] may exhibit abrupt desynchronization and multistability when three-body interactions replace [99], or are added to [100], pairwise interactions in globally coupled, i.e., all-to-all, oscillators. Moreover, the presence of many-body interactions generates explosive switches between synchronized and incoherent states in complex higher-order structures [101]. In these woks, it is assumed that the nodes represent the phase oscillators, while links and higher-order structures encode pairwise and many-body interactions among them. However, a completely different approach can be considered. In facts, an extension of the Kuramoto model, in which the oscillators are placed not only on the nodes but also on the higher-order structures, has been formulated [102, 103]. Interestingly, when the dynamics on the different structures are coupled, the transition to synchronization is once again explosive. Most of these studies are limited to numerical simulations only, or provide an analytical treatment for simplified cases, such as the all-to-all configuration. A few attempts to provide a mathematical framework for analyzing synchronization in the presence of multi-body interactions have been recently made. For instance, complete synchronization of chaotic oscillators has been analyzed for uniform hypergraphs [104]. Moreover, an analytical framework to study the Kuramoto model with higher-order interactions of any order, and for any complex topology, has been also proposed [105]. Yet, a general mathematical framework for the study of synchronization of nonlinear oscillators in presence of higher-order interactions is still lacking. In this direction, very recently, the necessary conditions under which global synchronization of identical topological signals, i.e., defined on nodes, links and other higher-order structures, can occur have been derived [106].

In contrast to the vast literature regarding the phenomenon of synchronization, little attention has been given to the investigation of pattern formation in reaction-diffusion systems with higher-order interactions. In facts, only a few attempts aimed at extending Turing's instability theory to the case of higher-order structures have been made. For instance, it has been show that when higher-order interactions are considered spatio-temporal patterns can emerge, whereby they can not be observed when

reducing all interactions to pairwise [107]. However, the proposed analytical framework is limited to the case of linear coupling functions. Hence, the development of a more general theory for Turing pattern formation in higher-order networks remains an open problem. Similarly to what has been done for synchronization, reaction-diffusion processes involving topological signals have been recently examined, and the conditions for the emergence of patterns in the case dynamics defined on nodes and links only have been established [108].

The objective of our work is to fill the existing gaps in the literature, developing a general mathematical theory that allows us to study the collective behavior of coupled dynamical systems in presence of higher-order interactions. In particular, we focus our attention on the two phenomena described above, namely synchronization of chaotic oscillators and pattern formation in reaction-diffusion systems. Crucially, we will demonstrate that our mathematical framework can be used to describe both. Interestingly, we will show how these two phenomena can be seem, from a mathematical point of view, as each other's opposite, with synchronization representing a homogeneous state that is stable, while the formation of patterns corresponding to an unstable homogeneous equilibrium.

This thesis is organized as follows. In Chapter 1, we present the mathematical framework. We introduce the notions of simplicial complexes and hypergraphs, describing the most important metrics for encoding their structure. We then develop a general model to describe the dynamics of a system of units coupled through many-body interactions, and we show how it is possible to study its behavior via a linear stability analysis. In Chapter 2, we study the synchronization of chaotic oscillators coupled through reciprocal higher-order interactions. We start from the most general case, discussing an application to neural dynamics. We then analyze a few special cases, which allow us to extend the Master Stability Function approach to the case of higher-order structures. In Chapter 3, we extend the results presented in the previous chapter, by discussing how nonreciprocal interactions impact the synchronization behavior of a system of coupled units. In Chapter 4, we analyze the phenomenon of pattern formation in reaction-diffusion systems in presence of many-body interactions. We extend Turing's instability theory to the case of higher-

order structures, by demonstrating how higher-order terms can modify the necessary conditions for the emergence of patterns. In Conclusions, we discuss and summarize the main results, discussing the possible future directions of our work.

Chapter 1

Dynamical systems with higher-order interactions

In this chapter, we introduce the mathematical framework that will allow us to study the dynamics of system of units coupled through higher-order interactions. First, we will introduce the notions of higher-order structures, and in particular those of simplicial complexes and hypergraphs. We will generalize to the higher-order case the main metrics defined for encoding graphs, namely those of adjacency matrix, of node degree, and of Laplacian matrix. In the first part of the section, we will consider the case of undirected structure, modeling systems where the interactions among the units are reciprocal. In the second part, we will discuss directionality in hypergraphs, which will turn out useful to describe systems characterized by nonreciprocal interactions. In the following section, we use these concepts to study dynamical systems unfolding on higher-order structures. We begin by describing the differential equations governing the dynamics of the system of coupled units, distinguishing between the general case and a particular case useful for the analysis of Turing pattern formation. Then, we show how it is possible to study the dynamical behavior of the system via a linear stability analysis that extends the Master Stability Function approach to the case of higher-order structures. In particular, we will discuss a few special cases, relying on particular assumptions either on the higher-order topology or on functional form of the interactions, allowing us to derive the necessary conditions for the

19

emergence of synchronization in networks of oscillators, and for the formation of patterns in reactive-diffusive systems.

1.1 Higher-order structures: graph and tensor representation

In this section, we present the higher-order structures we will work with, namely simplicial complexes and hypergraphs. In particular, we will present how their topology can be encoded in a set of adjacency tensors, generalizing the concept of adjacency matrix. On the basis of this, we will define the generalized degree of a node and that of a link, which will allow us to construct a collection of Laplacian matrices, each one related to a different order of interaction. We will first focus on the case of undirected higher-order structure, which can be used to model a system where reciprocal many-body interactions are present. Then, we will extend these concepts to the case of directed topologies, so to account for phenomena characterized by nonreciprocal higher-order interactions.

1.1.1 Undirected higher-order networks

Networks have proven to be an effective framework to model natural and artificial systems where the constituent units interact in pairs. From a mathematical point of view, we can represent a network as a graph $\mathcal{G} = (\mathcal{V}, \mathcal{E})$, where $\mathcal{V}$ is a set of $N = |\mathcal{V}|$ elements called nodes (or vertices), and $\mathcal{E}$ is a set of $K = |\mathcal{E}|$ elements called links (or edges), each of them given by a couple (i, j) of nodes, with $i, j \in \{1, \dots, N\}$. Despite their effectiveness in modeling various natural and artificial systems, networks fall short in capturing many-body interactions, i.e., group of more than two units interacting together. For instance, let us consider the simple case of three nodes, i, j, and k, interacting through a single three-body interaction. As networks are only able to describe pairwise interactions, such a case would be represented as a graph composed by three links, (i, j), (j, k), and (i, k). However, this representation is indistinguishable from that of three nodes i, j, and k, interacting through three different two-body interactions. Hence, to differentiate between these two configurations, we
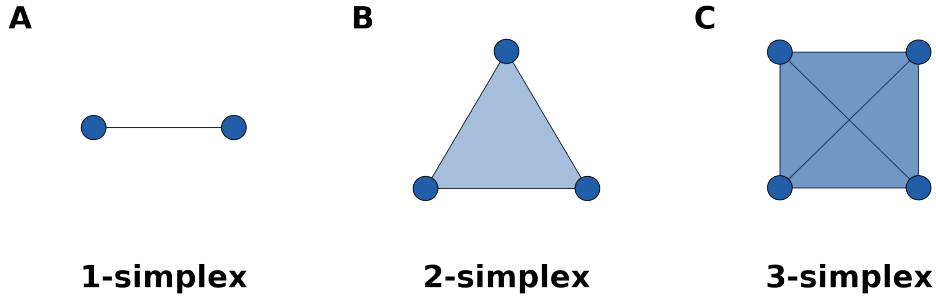
Figure 1.1: Graphical representation of simplices of different orders. Panel A displays a 1-simplex, which is a simple link, panel B a 2-simplex, while panel B a 3-simplex. In the rest of this work, we will represent simplices as triangles, tetrahedrons, and so on, so to emphasize the inclusion constraint that characterizes the simplicial complex structure.

need a to account for more complex structures that allow us to naturally capture many-body interactions.

Simplicial complexes and hypergraphs represent the proper mathematical structures to describe higher-order interactions. A *simplicial complex* is a collection of *simplices*, mathematical objects that extend the notion of links. In particular, while a link represents a pairwise interaction, a simplex can represent an interaction of any order. Formally, we can define a *m*-simplex, or a simplex of dimension *m*, as a set of $m + 1$ nodes. Therefore, a 0-simplex is a node, a 1-simplex is a link, a 2-simplex is a two-dimensional object formed by three nodes, and so on. Simplices allow us to distinguish between a a single three-body interactions, and three pairwise interactions. In facts, while the two-body interactions can be represented as links, i.e., as 1-simplices, a three-body interaction can be encoded by a 2-simplex. More in general, we can represent an interaction among $(m + 1)$ nodes as a *m*-simplices. As a graph is a collection of links, a simplicial complex $\mathcal{S}$ on a set of nodes $\mathcal{V}$, with $N = |\mathcal{V}|$, is a collection of Q simplices, namely $\mathcal{S} = \{\varsigma_1, \varsigma_2, \ldots, \varsigma_Q\}$. We define the order M of the simplicial complex as the dimension of the largest simplex in $\mathcal{S}$, namely $M = \max_\varsigma |\varsigma|$. Differently from graphs, which have no extra requirements, a simplicial complex has a further *inclusion constraint*, namely

A **B** **C**

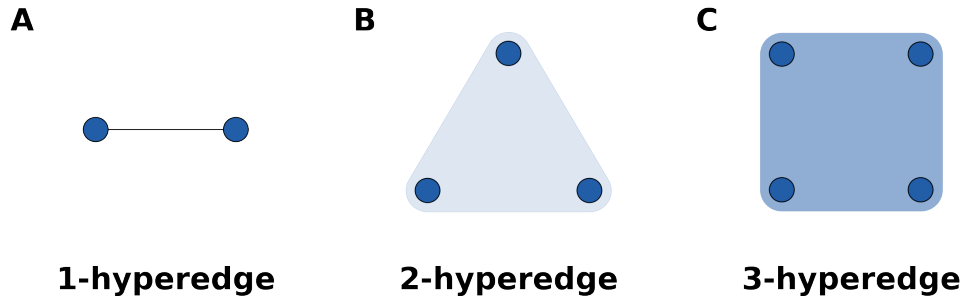**1-hyperedge** **2-hyperedge** **3-hyperedge**

Figure 1.2: Graphical representation of hyperedges of different orders. Panel A displays a 1-hyperedge, which is a simple link, panel B a 2-hyperedge, while panel B a 3-hyperedge. In the rest of this work, we will represent hyperedges as polygons with rounded corners, so to emphasize the absence of the inclusion constraint, as in the case of simplicial complexes.

that for any simplex $\varsigma \in \mathcal{S}$, all the sub-simplices $\varsigma' \subset \varsigma$ are also part of the simplicial complex, i.e., $\varsigma' \in \mathcal{S}$. For instance, if a 2-simplex (i,j,k) is part of a simplicial complex $\mathcal{S}$, then all the included 1-simplices, i.e., (i,j), (j,k), and (i,k), and all the included 0-simplices, i.e., i, j, and k, are also part of $\mathcal{S}$. Though this extra requirement on the sub-simplices is in some cases justifiable, for instance when modeling social systems [85], or the brain functional networks [77], it may result too restrictive in others. In particular, the inclusion constraint does not allow to model those systems where the existence of a many-body interaction does not necessarily imply the presence of all the possible sub-interactions. A classical example is that of scientific collaboration. Indeed, the fact that three researchers have authored a paper, which we could represent as a 2-simplex, does not necessarily imply that the three possible pairs of authors have also published a paper [82].

To overcome these limitations, we can rely on hypergraphs, which are the most general mathematical structure for describing higher-order interactions. Similarly to a simplicial complex, a *hypergraph* is a collection of *hyperedges*, which, as the simplices, generalize the concept of link, allowing to represent many-body interactions. From a mathematical point

of view, a *m*-hyperedge, or an hyperedge of dimension *m*, is a set of $m + 1$ nodes, encoding an interaction among the same number of units. Hence, a three-body interaction can be represented as a 2-hyperedge, a four-body interactions as a 3-hyperedge, and so on. Let us remark that such a notation is different from the one usually adopted for hypergraphs, for which a *m*-hyperedge is a set of *m* nodes [107, 109]. However, as it will become clear in what follows, we decided to use the current notation so to emphasize the similarities between simplicial complexes and hypergraphs in their tensor representation. Finally, an hypergraph $\mathcal{H}$ defined on a set of nodes $\mathcal{V}$, with $N = |\mathcal{V}|$, is a collection of Q hyperedges, namely $\mathcal{H} = \{h_1, h_2, \ldots, h_Q\}$. As for the simplicial complexes, we define the order M of the hypergraph as the dimension of its largest hyperedge, namely $M = \max_h |h|$. Let us remark that, given the definitions of simplicial complex and of hypergraph here provided, the former is a particular case of the latter for all intents and purposes.

Given a graph $\mathcal{G} = (\mathcal{V}, \mathcal{E})$, we can associate to it an adjacency matrix **A**, which encodes the connections among the nodes. In particular, the element a_{ij} of the matrix is equal to one if the pair $(i, j) \in \mathcal{E}$, namely if nodes *i* and *j* are connected, while it is equal to zero otherwise. Hence, our aim is to generalize the notion of the adjacency matrix of a network to simplicial complexes and hypergraphs, so to encode many-body interactions. Let us observe that the following definitions hold for both simplicial complexes and hypergraphs. For the sake of brevity, we will always refer to the hypergraph-related terminology, though the same applies for simplicial complexes. We will point out the differences between the two structures when required. For each dimension *m*, we can define a $N \times N \times \cdots \times N$, with N repeated $m + 1$ times, *adjacency tensor* $\mathbf{A}^{(m)}$, whose element $a^{(m)}_{i_1 \ldots i_{m+1}}$ are given by

$$a^{(m)}_{i_1 \ldots i_{m+1}} = \begin{cases} 1 & \text{if } (i_1, \ldots, i_{m+1}) \in \mathcal{H} \\ 0 & \text{otherwise} \end{cases}, \tag{1.1}$$

Note that, as we are here considering the case of reciprocal many-body interactions, each tensor is symmetric with respect to its $m + 1$ indexes, meaning that

$$a^{(m)}_{i_1 \ldots i_{m+1}} = 1 \Rightarrow a^{(m)}_{\pi(i_1 \ldots i_{m+1})} = 1, \tag{1.2}$$

for any $m \in \{1, \ldots, M\}$, and for any permutation π of the tensor indexes. In the next section, we will study how these definition change as we account for nonreciprocal higher-order interactions. Given definition (1.1), the $N \times N$ matrix $\mathbf{A}^{(1)}$, which coincides with the standard adjacency matrix, characterizes the structure of the two-body interactions, the $N \times N \times N$ tensor $\mathbf{A}^{(2)}$ captures the three-body interactions, and so on. Hence, given a set of M adjacency tensor $\mathbf{A}^{(m)}$, with $m \in \{1, \ldots, M\}$, we are able to encode the connectivity patterns of a higher-order structure, either a hypergraph or a simplicial complex. It is worth noting that the inclusion constraint that characterizes the latter is reflected in the elements of the adjacency tensor. In particular, if the tensor $a^{(m)}_{i_1 \ldots i_{m+1}} = 1$, the tensors associated to order $m' < m$ will have nonzero elements in correspondence to every permutation of m' of the indexes $i_1, \ldots i_{m+1}$. For instance, if $a^{(2)}_{ijk} = 1$, i.e., nodes i, j, and k interact in triples, then $a^{(1)}_{ij} = a^{(1)}_{jk} = a^{(1)}_{ik} = 1$, and $a^{(1)}_{ji} = a^{(1)}_{kj} = a^{(1)}_{ki} = 1$ i.e., the nodes also interact in pairs.

In a graph, a node i can be characterized by its degree $k(i)$, namely by the number of links incident in it. The degree represents the number of two-body interactions in which a unit is involved. In a higher-order structure, however, this is no longer sufficient. In facts, a unit can be involved not only in two-body interactions, but also in three-body interactions, four-body interactions, and so on. Therefore, we need to generalize the concept of degree of a node, so to account for the number of m-hyperedges incident in a node. In a graph, the standard degree, $k(i)$, of a node i is defined as

$$k(i) = \sum_{j=1}^{N} a_{ij}. \tag{1.3}$$

For higher-order structure, we define the *generalized m-degree*, $k^{(m)}(i)$, of a node i as

$$k^{(m)}(i) = \frac{1}{m!} \sum_{j_1=1}^{N} \sum_{j_2=1}^{N} \cdots \sum_{j=m}^{N} a^{(m)}_{ij_1 j_2 \ldots j_m}, \tag{1.4}$$

with $m \in \{1, \ldots, M\}$. In particular, $k^{(1)}(i)$ coincides with the standard degree $k(i)$, so it represents the number of links incident to node i, $k^{(2)}(i)$

counts instead the number of 2-hyperedges incident in node i, $k^{(3)}(i)$ the number of 3-hyperedges, and so on.

For higher-order structure, it is also useful to define another quantity, namely the number of m-hyperedges of which a pair of nodes (i, j) is part of. We call this quantity the *generalized m-degree*, $k^{(m)}(i, j)$, of a node pair (i, j). This is given by

$$k^{(m)}(i, j) = \frac{1}{(m-1)!} \sum_{l_1=1}^{N} \sum_{l_2=1}^{N} \cdots \sum_{l=m-1}^{N} a_{ijl_1l_2\ldots l_{m-1}}^{(m)}, \qquad (1.5)$$

where $m \in \{1, \ldots, M\}$. Straightforwardly, for $m = 1$ we have $k^{(1)}(i, j) = a_{ij}^{(1)}$, as the number of 1-hyperedges, i.e., of links, a pair of nodes is part of can either be zero or one. Then, $k^{(2)}(i, j)$ counts the number of 2-hyperedges the pair of nodes (i, j) is part of, $k^{(3)}(i, j)$ the number of 3-hyperedges, and so on.

Finally, given the definition of the m-degrees of nodes and links, we can generalize the notion of Laplacian matrix to higher-order interactions. The Laplacian of a graph is widely used to study dynamical processes on networks, as it is associated to diffusion [110]. In particular, the graph Laplacian has been exploited to describe consensus [111], random walk [112], synchronization [1], Turing pattern formation [67], among many others. Different generalizations of the Laplacian matrix to higher-orders interactions have been recently proposed. Among them, we can crucially distinguish between two categories. On the one hand, we find those generalizations used to describe *hypergraph signals* and *topological signals*, namely coupled systems in which the dynamics is defined not only on nodes, but also on links and higher-order structures [113, 114]. These include the Laplacians used to describe processes on uniform hypergraphs [115, 116], i.e., structures where all hyperedges have the same size, and Hodge Laplacians, which govern dynamics unfolding on simplicial complexes [88, 102]. On the other hand, we have generalized Laplacians governing systems where the dynamics is only defined on nodes [105], with link and higher-order structures solely representing the interactions among the system units. In this work, we will consider this latter case. Hence, given Eqs. (1.4) and (1.5), we define the *generalized Laplacian of*

order m, $\mathbf{L}^{(m)}$, as the matrix whose elements are given by

$$L_{ij}^{(m)} = \begin{cases} m! k^{(m)}(i) & \text{if } i = j \\ -(m-1)! k^{(m)}(i,j) & \text{if } i \neq j \end{cases},$$

(1.6)

with $m \in \{1, \dots, M\}$. Let us note that $\mathbf{L}^{(1)}$ recovers the standard Laplacian matrix. It is here worth remarking that, in the case of undirected higher-order structures, the Laplacians are all symmetric, real-valued, and zero-row-sum. Therefore, they are all diagonalizable, their eigenvalues are real and nonnegative, the corresponding set of eigenvectors constitutes a orthonormal basis of $\mathbb{R}^N$. Furthermore, they all share, as the smallest of their eigenvalues, $\lambda_1^{(m)} = 0$, whose associated eigenvector is $[1, 1, \dots, 1]^T / \sqrt{N}$. As we will see in the next sections, these properties of the generalized Laplacian matrices will turn out useful in the analysis of dynamical systems with higher-order interactions. Before that, we will extend the concepts introduced in this section to the case of directed structures, which will allow us to study the case of systems characterized by nonreciprocal higher-order interactions.

1.1.2 Directed higher-order networks

In the last section, we have provided the most important concepts for describing undirected higher-order topologies, which are useful to model systems where reciprocal many-body interactions are present. However, different natural and artificial systems are characterized by group interactions that are intrinsically asymmetric. A first example comes from social systems. In particular group pressure has an asymmetric nature, as group interactions that are addressed toward one or more individuals are not necessarily reciprocated [117]. Another instance of higher-order processes where a privileged direction is present is represented by (bio)chemical reactions, as they can be irreversible due to thermodynamics [118, 119]. Lastly, a further example comes from the ecology of microbial communities, where the action of a species on another can be mediated by a third species [120, 121]. To provide a mathematical framework to deal with such cases, in this section we define directed higher-order networks,

characterizing their adjacency tensors and the quantities that one can derive from them. In what follows, we will consider directed hypergraphs only. In facts, while for undirected structures the similarities between hypergraphs and simplicial complexes were straightforward, i.e., the latter can be considered a constrained version of the former, this is not the case for directed structures. In particular, a crucial aspect to discuss in order to generalize the notion of simplices from undirected to directed is whether and how the inclusion constraint can be extended to the directed case. A first (negative) answer comes from the case of oriented simplicial complexes [102], for which a simplex and its sub-simplices can have either concordant or opposite orientation. However, the notions of orientation and directionality are generally different, so the definition of directed simplicial complexes remains disputable. Hence, in the present work we will only focus on hypergraphs, leaving the discussion on how to define directed simplicial complexes for future research.

It is here worth remarking that the notion of directed hypergraphs that we will hereby discuss is different from that of oriented hypergraph proposed in [122, 123, 124]. In facts, oriented hypergraphs are fundamentally symmetric structures, while directed hypergraphs are not. In particular, oriented hypergraphs are *undirected* higher-order structures, where the nodes of each hyperedge are partitioned into two sets, namely the input and the output set. However, these two roles are not distinguished as it is for directed hypergraphs [122], which is the feature making the latter an asymmetric structure.

From a mathematical point of view, we can represent a network of nonreciprocal, pairwise interactions as a directed graph $\mathcal{G} = (\mathcal{V}, \mathcal{E})$, where $\mathcal{V}$ is a set of $N = |\mathcal{V}|$ nodes, and $\mathcal{E}$ is a set of $K = |\mathcal{E}|$ directed links, which are given by an ordered couple (i, j) of nodes, with $i, j \in \{1, \dots, N\}$. As for undirected graphs, we can associate to a directed graph an adjacency matrix $\mathbf{A}$. However, differently from the undirected case, the element a_{ij} of the matrix is equal to one if the *ordered pair* $(i, j) \in \mathcal{E}$, namely if it exists a link "pointing" from node j to node i are connected, while it is equal to zero otherwise. Crucially, we note that the elements a_{ij} and a_{ji} of the adjacency matrix encode two different interactions. In facts, the former describes whether unit j influences unit i, while the latter characterize the opposite interaction, i.e., i to j. Hence, the property of symmetry in undi-
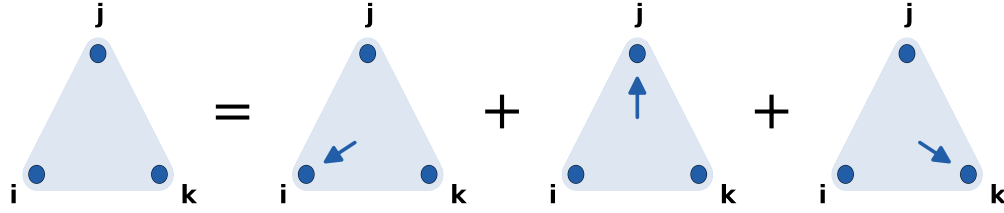
Figure 1.3: Graphical representation the elementary decomposition of an undirected 2-hyperedge in three directed hyperedges.

rected graphs, $a_{ij} = a_{ji}$, models the fact that *both* "directions" of interaction are present, as each interaction is reciprocal. This idea of considering a single undirected link as the combination of two directed links, which models the fact that a reciprocal, two-body interaction can be seen as the combination of two opposite two-body interactions, is the core feature that allows us to generalize the notion of directionality to higher-order structures.

We start by defining a 1-*directed m-hyperedge* as a set of $(m+1)$ nodes, m of which, called "source nodes", point toward the remaining one, called "target node". Such a mathematical object represents an interaction among $(m+1)$ units where m of them jointly influence a further one, without necessarily an opposite action of the target unit. Generalizing the concept of an undirected link as the combination of two directed links, we can see an undirected m-hyperedge as the union of $(m+1)$ directed ones. We will refer to this idea as the *elementary decomposition* of a m-hyperedge. A graphical representation of the case $m = 2$, i.e., three-body interactions, is represented in Fig. 1.3. For each order of interaction, m, we can define an adjacency tensor $\mathbf{A}^{(m)}$, whose element $a_{ij_1...j_m}^{(m)}$ represents the 1-directed m-hyperedge having $j_1, j_2, \ldots, j_m$ as the source nodes and i as the target node. As we are studying the case where m units of the system act together on a further one, without necessarily a reciprocal interaction, and with no distinction in the order in which the influencing units are considered, the corresponding adjacency tensors are characterized by the property

$$a_{ij_1...j_m}^{(m)} = 1 \Rightarrow a_{i\pi(j_1...j_m)}^{(m)} = 1, \tag{1.7}$$

for any permutation π of the indexes j_1, j_2, ..., j_m. We observe that a generic permutation involving all tensor indexes does not necessarily imply a nonzero entry in the adjacency tensor, as it was in the case of undirected structures (see Eq. (1.2)), encoding the fact that higher-order interactions are not necessarily reciprocated. Moreover, we note that $(m + 1)$-th rank tensors obtained by fixing the first index of $\mathbf{A}^{(m)}$ are symmetric, representing the fact that there is no distinction among the influencing units. Lastly, we call 1-*directed M-hypergraph* a hypergraph formed by 1-directed m-hyperedges of any size $m \leq M$.

The 1-directed hyperedge defined above is able to model those interactions where many source units of a system influence a single target unit. However, this may result a strong limitation. In facts, there might be cases for which in a group of m interacting units, t of them are jointly influenced by the remaining $s = m + 1 - t$. To describe mathematically such a scenario, we can define a *t-directed m-hyperedge*, with $t \leq m$, as a set of $m + 1$ nodes, a subset of which (formed by s units) points toward the t remaining ones. Again, to encode such a structure, we can define an adjacency tensor $\mathbf{A}^{(m)}$, whose element $a^{(m)}_{i_1...i_t j_1...j_s}$ represents the t-directed m-hyperedge having j_1, ..., j_s as the source nodes, and i_1, ..., i_t as the target nodes. As no distinction in the order in which both the influencing and the influenced units are considered, the adjacency tensors will be characterized by a symmetry property similar to that in Eq. (1.7), namely

$$a^{(m)}_{i_1...i_t j_1...j_s} = 1 \Rightarrow a^{(m)}_{\pi^t(i_1...i_t)\pi^s(j_1...j_s)} = 1, \tag{1.8}$$

for any permutation π^t of the indexes, i_1, ..., i_t, relative to the target nodes, and for any permutation π^s of the indexes, j_1, ..., j_s, relative to the source nodes. Similarly to the case of 1-directed hyperedges, we note that a permutation where one or more of the indexes associated to the target nodes appear in a position other than the first t, may result in a zero entry of the adjacency tensor, which once again encodes the fact that the corresponding higher-order interaction is not necessarily reciprocated. Finally, by indicating with T the largest value of t, we define the *T-directed M-hypergraph*.

Let us here remark that the definitions given above represent a tensor representation of the directed hyperedges introduced to account for

various problems arising in computer science and in combinatorial optimization [125, 126, 127]. In particular, the notions of 1-directed hyperedge and 1-directed hypergraph recall those of *backward-hyperarc*, or B-arc for simplicity, and *B-hypergraph* introduced in [126]. However, most of the literature dealing with directed hypergraphs is related to the development of algorithms for various applications in database theory [125, 128], propositional logic [129], and urban transportation [130], to name a few, while our work deals with modeling higher-order interactions in system of coupled dynamical units.

Our next step consists in generalizing the notion of m-degree to the case of directed higher-order topologies, from now on focusing on 1-directed hypergraphs. In facts, as we will see in the next section, the structural properties of 1-directed hypergraphs, i.e., Eq. (1.7), will permits to analyze the dynamical behavior of systems of units coupled through nonreciprocal interactions. In particular, it will allows us to derive analytically the necessary conditions either for the synchronization of chaotic systems and for the formation of Turing patterns in coupled chemical oscillators. Nonetheless, the definitions hereby provided for 1-directed hypergraphs can be straightforwardly generalized to T-directed structures. In a directed graph, a node i can be characterized by its in-degree $k_{\text{in}}(i)$, namely by the number of links pointing toward it, as well as its out-degree $k_{\text{out}}(i)$, i.e., the number of links pointing out from it. For the purpose of our work, here we are interested only in the generalization of the former to the case of higher-order structures. In particular, we define the *generalized m-in-degree*, $k^{(m)}(i)$, of a node i, namely the number of m-hyperedges pointing toward node i as

$$k_{\text{in}}^{(m)}(i) = \frac{1}{m!} \sum_{j_1=1}^{N} \sum_{j_2=1}^{N} \cdots \sum_{j=m}^{N} a_{ij_1j_2\cdots j_m}^{(m)} , \qquad (1.9)$$

with $m \in \{1, \ldots, M\}$. $k^{(1)}(i)$ coincides with the standard in-degree $k_{\text{in}}(i)$, $k_{\text{in}}^{(2)}(i)$ represents the number of 2-hyperedges pointing toward node i, $k_{\text{in}}^{(3)}(i)$ the number of 3-hyperedges, and so on. Then, we define the *generalized m-in-degree*, $k_{\text{in}}^{(m)}(i,j)$, of a node pair (i,j), characterizing the number of 1-directed m-hyperedges having i as the target node, and j as one of its

source nodes. We define it as

$$k_{\text{in}}^{(m)}(i,j) = \frac{1}{(m-1)!} \sum_{l_1=1}^{N} \sum_{l_2=1}^{N} \cdots \sum_{l=m-1}^{N} a_{ijl_1l_2\ldots l_{m-1}}^{(m)},$$ (1.10)

where $m \in \{1,\ldots,M\}$. For $m = 1$ we simply have $k_{\text{in}}^{(1)}(i,j) = a_{ij}^{(1)}$, while $k_{\text{in}}^{(2)}(i,j)$ counts the number of 1-directed 2-hyperedges pointing toward i and having j as one of the source nodes, $k_{\text{in}}^{(3)}(i,j)$ the number of 1-directed 3-hyperedges with the same configuration, and so on. Crucially, given property (1.7) and differently from the undirected case, we generally have that $k_{\text{in}}^{(m)}(i,j) \neq k_{\text{in}}^{(m)}(j,i)$, which somehow extends the fact that in directed graphs $a_{ij} \neq a_{ji}$, in general.

Lastly, with the definition of the m-in-degrees of nodes and links, we can extend the definition of the generalized Laplacians to the directed case. In particular, we define the generalized Laplacian associated to the $(m+1)$-body interactions as the matrix whose elements are given by

$$L_{ij}^{(m)} = \begin{cases} m! k_{\text{in}}^{(m)}(i) & \text{if } i = j \\ -(m-1)! k_{\text{in}}^{(m)}(i,j) & \text{if } i \neq j \end{cases},$$ (1.11)

with $m \in \{1,\ldots,M\}$. As for the undirected case, the Laplacians are real-valued, and zero-row-sum. However, differently from the previous case, $\mathbf{L}^{(m)}$ is not symmetric, as in general $L_{ij}^{(m)} \neq L_{ji}^{(m)}$, which makes definition (1.11) a natural generalization to hypergraphs of the Laplacian matrix associated to directed graphs [69].

In this section, we have presented the most important metrics to encode higher-order structures. In particular, we have extended to the case of hypergraphs and simplicial complexes, the notions of adjacency and Laplacian matrices, distinguishing between the cases of undirected and directed structures. In the next section, we will use these concepts to study the dynamics of system of units coupled through higher-order interactions.

1.2 Dynamics of a system of units coupled with higher-order interactions

We want to study the dynamics of a system of N identical units, coupled through both pairwise and higher-order interactions. We consider a higher-order structure of order M, where two-body up $(M+1)$-body interactions are present. We write the equations governing the temporal evolution of the system as follows:

$$
\dot{\mathbf{x}}_i = \mathbf{f}(\mathbf{x}_i) + \sigma_1 \sum_{j_1=1}^{N} a_{ij_1}^{(1)} \mathbf{g}^{(1)}(\mathbf{x}_i, \mathbf{x}_{j_1}) + \sigma_2 \sum_{j_1=1}^{N} \sum_{j_2=1}^{N} a_{ij_1j_2}^{(2)} \mathbf{g}^{(2)}(\mathbf{x}_i, \mathbf{x}_{j_1}, \mathbf{x}_{j_2})
$$
$$
+ \cdots + \sigma_M \sum_{j_1=1}^{N} \cdots \sum_{j_M=1}^{N} a_{ij_1\ldots j_M}^{(M)} \mathbf{g}^{(M)}(\mathbf{x}_i, \mathbf{x}_{j_1}, \ldots, \mathbf{x}_{j_M}),
$$

(1.12)

where $\mathbf{x}_i$ is the d-dimensional vector describing the state of unit i, while $\mathbf{f} : \mathbb{R}^d \longrightarrow \mathbb{R}^d$ is a nonlinear function describing the dynamics of the isolated system. Notice that $\mathbf{f}$ is assumed to be identical for each unit i. $\sigma_1, \ldots, \sigma_M$ are real positive numbers representing the coupling strength, $a_{ij_1\ldots j_m}^{(m)}$ are the entries of the adjacency tensor $\mathbf{A}^{(m)}$, while $\mathbf{g}^{(m)} : \mathbb{R}^{(m+1)\times d} \longrightarrow \mathbb{R}^d$, with $m \in \{1, \ldots, M\}$ are coupling functions ruling the interactions at different orders. We will assume the coupling functions to be *non-invasive*, meaning that

$$
\mathbf{g}^{(m)}(\mathbf{x}, \mathbf{x}, \ldots, \mathbf{x}) = 0, \ \forall \mathbf{x} \in \mathbb{R}^d, \ \forall m \in \{1, \ldots, M\}. \tag{1.13}
$$

In the context of synchronization, the assumption of non-invasiveness guarantees the existence of a synchronous state, i.e., the synchronization manifold. Indeed, when $\mathbf{x}_i = \mathbf{x}^s$, $\forall i \in \{1, \ldots, N\}$, when property (1.13) holds we can write Eqs. (1.12) simply as $\dot{\mathbf{x}}_i = \mathbf{f}(\mathbf{x}^s)$, which is equivalent for each unit i, meaning that all units have the same dynamics. Similarly, in the case of Turing pattern formation, assuming the existence of a fixed point $\mathbf{x}^*$ for the isolated system, i.e., $\mathbf{f}(\mathbf{x}^*) = \mathbf{0}$, the non-invasiveness of the coupling functions $\mathbf{g}^{(m)}$ guarantees the existence of an homogeneous equilibrium point solution for the coupled system, namely $\mathbf{x}_i = \mathbf{x}^*$, $\forall i \in \{1, \ldots, N\}$. An example of non-invasive couplings are

the sinusoidal functions used in the Kuramoto model [98] and its higher-order generalizations [105, 101], though, in this case, the oscillators are not identical, so one can not define a synchronization manifold.

A largely examined class of non-invasive functions, especially in the study of Turing patterns, is that of diffusive-like couplings. In particular, a function $\mathbf{g}^{(m)}$ is diffusive-like if there is a function $\mathbf{h}^{(m)} : \mathbb{R}^{m \times d} \longrightarrow \mathbb{R}^d$ such that

$$\mathbf{g}^{(m)}(\mathbf{x}_i, \mathbf{x}_{j_1}, \ldots, \mathbf{x}_{j_m}) = \mathbf{h}^{(m)}(\mathbf{x}_{j_1}, \ldots, \mathbf{x}_{j_m}) - \mathbf{h}^{(m)}(\mathbf{x}_i, \ldots, \mathbf{x}_i), \qquad (1.14)$$

for every $m \in \{1, \ldots, M\}$. From definition (1.14) it is straightforward to verify that diffusive-like functions are non-invasive. Let us remark that in the context of networks the linear case of diffusive coupling, i.e., $\mathbf{h}^{(1)}(\mathbf{x}) = \mathbf{x}$ has been extensively studied both in synchronization [49] and in Turing pattern formation [67]. Moreover, although less analyzed in networked systems, nonlinear diffusions have been vastly used to model a large variety of physical processes [131, 132], included plasma diffusion [133], melting and evaporation processes in metals [134], and Turing pattern formation [135, 136]. In this work, we will largely rely on non-linear diffusive-like functions, as linear higher-order interactions can be reduced to pairwise interactions by defining a proper weighted adjacency matrix encoding all the existing interactions among the units (see [91] for details).

Despite relying on a similar mathematical framework, the analysis of the synchronization stability and that of Turing pattern formation usually account for different assumptions on the systems. As already anticipated, the study of synchronization consists in analyzing the stability of a synchronous state $\mathbf{x}^s$, which can be either a limit cycle or a chaotic attractor. On the other hand, for the analysis of Turing patterns, one usually studies the stability of a stable fixed point $\mathbf{x}^*$. This is reflected in the properties of the local dynamics function $\mathbf{f}$. In particular, in the case of synchronization one considers systems for which the maximum Lyapunov exponent associated to $\mathbf{f}$ is either zero, in the case of limit cycles, or positive, in the case of chaotic oscillators. For Turing pattern formation, however, one accounts for systems whose associated maximum Lyapunov exponent is negative. Note that, as we are considering the case of a fixed point, the latter coincides with the largest eigenvalue of the Jacobian matrix of $\mathbf{f}$.

Let us observe that the study of Turing pattern formation is commonly done in a more restrictive framework compared to the one adopted for synchronization. In particular, one usually assumes two species activator-inhibitor systems, i.e., $\mathbf{x}_i = [u_i, v_i]^T$ coupled through diffusive-like functions. Moreover, it is often assumed that no cross-diffusion occurs, namely that the coupling functions are given by

$$
\begin{aligned}
\mathbf{h}^{(1)}(u,v) &= [D_u^{(1)} h_u^{(1)}(u,v), D_v^{(1)} h_v^{(1)}(u,v)]^T \\
&= [D_u^{(1)} h_u^{(1)}(u), D_v^{(1)} h_v^{(1)}(v)]^T, \\
\mathbf{h}^{(2)}(u_1, v_1, u_2, v_2) &= [D_u^{(2)} h_u^{(2)}(u_1, v_1, u_2, , v_2), D_v^{(2)} h_v^{(2)}(u_1, v_1, u_2, v_2)]^T \\
&= [D_u^{(2)} h_u^{(2)}(u_1, u_2), D_v^{(2)} h_v^{(2)}(v_1, v_2)]^T,
\end{aligned}
\tag{1.15}
$$

$$
\vdots
$$

$$
\mathbf{h}^{(M)}(u_1, v_1, \ldots, u_M, v_M) = [D_u^{(M)} h_u^{(M)}(u_1, \ldots, u_M), D_v^{(M)} h_v^{(M)}(v_1, \ldots, v_M)]^T,
$$

where $D_u^{(m)}, D_u^{(m)}$, with $m \in \{1, \ldots, M\}$, are real non-negative numbers representing the diffusion coefficients at different orders of interaction. Though we will limit our analysis to this case, it is worth remarking that multispecies diffusion has been thoroughly investigated [137, 138]. Under these assumptions, Eq. (1.12) can be written as

$$
\begin{aligned}
\dot{u}_i =& f_u(u,v) + \sigma_1 \sum_{j_1} a_{ij_1}^{(1)} D_u^{(1)} \left[h_u^{(1)}(u_{j_1}) - h_u^{(1)}(u_i) \right] \\
&+ \sigma_2 \sum_{j_1, j_2} a_{ij_1 j_2}^{(2)} D_u^{(2)} \left[h_u^{(2)}(u_{j_1}, u_{j_2}) - h_u^{(2)}(u_i, u_i) \right] \\
&+ \cdots + \sigma_M \sum_{j_1, \ldots, j_M} a_{ij_1 \ldots j_M}^{(M)} D_u^{(M)} \left[h_u^{(M)}(u_{j_1}, \ldots, u_{j_M}) - h_u^{(M)}(u_i, \ldots, u_i) \right], \\
\dot{v}_i =& f_v(u,v) + \sigma_1 \sum_{j_1} a_{ij_1}^{(1)} D_v^{(1)} \left[h_v^{(1)}(v_{j_1}) - h_v^{(1)}(v_i) \right] \\
&+ \sigma_2 \sum_{j_1, j_2} a_{ij_1 j_2}^{(2)} D_v^{(2)} \left[h_v^{(2)}(v_{j_1}, v_{j_2}) - h_v^{(2)}(v_i, v_i) \right] \\
&+ \cdots + \sigma_M \sum_{j_1, \ldots, j_M} a_{ij_1 \ldots j_M}^{(M)} D_v^{(M)} \left[h_v^{(M)}(v_{j_1}, \ldots, v_{j_M}) - h_v^{(M)}(v_i, \ldots, v_i) \right],
\end{aligned}
\tag{1.16}
$$

where we have considered a more compact notation for the summations.

In the following sections, we will consider the more general mathematical framework of Eq. (1.12), pointing out the most relevant differ-

ences between the analyses of synchronization and Turing pattern formation where needed. In Chapter 4, when studying pattern formation in details, we will instead account for the specific case of system (1.16).

1.3 Linear stability analysis in higher-order structures

To investigate both the onset of synchronization and the formation of Turing patterns, we here perform a linear stability analysis of Eq. (1.12). In particular, our goal is to study how a small perturbation around the synchronous state $\mathbf{x}^s$ or the fixed point $\mathbf{x}^*$ evolves in time. In the case of synchronization we aim to understand the conditions under which perturbations transverse to $\mathbf{x}^s$ shrink in time, i.e., the system remain on the synchronization manifold. On the other hand, in the case of Turing patterns our objective is to find when a perturbation around $\mathbf{x}^*$ does not go to zero, meaning that the system moves away from the homogeneous solution. Hence, we can analyze both phenomena in terms of the (in)stability of a linearized system. We will use the notation $\bar{\mathbf{x}}$ to indicate the state, which may correspond either to the synchronous state $\mathbf{x}^s$ and to the fixed point $\mathbf{x}^*$, around which we perform the linearization.

Let us thus consider small perturbations $\delta\mathbf{x}_i = \mathbf{x}_i - \bar{\mathbf{x}}$, whose dynamics is governed by the system of equations

$$
\begin{aligned}
\delta\dot{\mathbf{x}}_i =& J\mathbf{f}(\overline{\mathbf{x}})\delta\mathbf{x}_i + \sigma_1 \sum_{j_1} a_{ij_1}^{(1)} \left[\frac{\partial\mathbf{g}^{(1)}(\mathbf{x}_i,\mathbf{x}_{j_1})}{\partial\mathbf{x}_i}\bigg|_{\overline{\mathbf{x}}} \delta\mathbf{x}_i + \frac{\partial\mathbf{g}^{(1)}(\mathbf{x}_i,\mathbf{x}_{j_1})}{\partial\mathbf{x}_{j_1}}\bigg|_{\overline{\mathbf{x}}} \delta\mathbf{x}_{j_1} \right] \\
&+ \sigma_2 \sum_{j_1,j_2} a_{ij_1j_2}^{(2)} \left[\frac{\partial\mathbf{g}^{(2)}(\mathbf{x}_i,\mathbf{x}_{j_1},\mathbf{x}_{j_2})}{\partial\mathbf{x}_i}\bigg|_{\overline{\mathbf{x}}} \delta\mathbf{x}_i \right. \\
&\qquad\qquad + \frac{\partial\mathbf{g}^{(2)}(\mathbf{x}_i,\mathbf{x}_{j_1},\mathbf{x}_{j_2})}{\partial\mathbf{x}_{j_1}}\bigg|_{\overline{\mathbf{x}}} \delta\mathbf{x}_{j_1} + \left. \frac{\partial\mathbf{g}^{(2)}(\mathbf{x}_i,\mathbf{x}_{j_1},\mathbf{x}_{j_2})}{\partial\mathbf{x}_{j_2}}\bigg|_{\overline{\mathbf{x}}} \delta\mathbf{x}_{j_2} \right] \\
&+ \cdots + \sigma_M \sum_{j_1,\dots,j_M} a_{ij_1\dots j_M}^{(M)} \left[\frac{\partial\mathbf{g}^{(M)}(\mathbf{x}_i,\mathbf{x}_{j_1},\dots,\mathbf{x}_{j_M})}{\partial\mathbf{x}_i}\bigg|_{\overline{\mathbf{x}}} \delta\mathbf{x}_i \right. \\
&\qquad\qquad + \frac{\partial\mathbf{g}^{(M)}(\mathbf{x}_i,\mathbf{x}_{j_1},\dots,\mathbf{x}_{j_M})}{\partial\mathbf{x}_{j_1}}\bigg|_{\overline{\mathbf{x}}} \delta\mathbf{x}_{j_1} \\
&\qquad\qquad + \cdots + \left. \frac{\partial\mathbf{g}^{(M)}(\mathbf{x}_i,\mathbf{x}_{j_1},\dots,\mathbf{x}_{j_M})}{\partial\mathbf{x}_{j_M}}\bigg|_{\overline{\mathbf{x}}} \delta\mathbf{x}_{j_M} \right],
\end{aligned} \tag{1.17}
$$

where $J\mathbf{f}(\overline{\mathbf{x}}) \in \mathbb{R}^{d\times d}$ is the Jacobian matrix of the function $\mathbf{f}$ evaluated in $\overline{\mathbf{x}}$, while the notation $\cdot|_{\overline{\mathbf{x}}}$ indicates that all the arguments in the partial derivatives are evaluated in $\overline{\mathbf{x}}$. Observe also that the derivatives do not depend on the indexes of the summations.

Next, we can rewrite the linearized system using the property of non-invasiveness of the coupling functions. Indeed, as their value is constant when all their arguments are equal, it follows that their total derivative evaluated on $(\overline{\mathbf{x}},\dots,\overline{\mathbf{x}})$ vanishes, namely

$$
\begin{aligned}
&\frac{\partial\mathbf{g}^{(1)}(\mathbf{x}_i,\mathbf{x}_{j_1})}{\partial\mathbf{x}_i}\bigg|_{\overline{\mathbf{x}}} + \frac{\partial\mathbf{g}^{(1)}(\mathbf{x}_i,\mathbf{x}_{j_1})}{\partial\mathbf{x}_{j_1}}\bigg|_{\overline{\mathbf{x}}} = 0, \\
&\frac{\partial\mathbf{g}^{(2)}(\mathbf{x}_i,\mathbf{x}_{j_1},\mathbf{x}_{j_2})}{\partial\mathbf{x}_i}\bigg|_{\overline{\mathbf{x}}} + \frac{\partial\mathbf{g}^{(2)}(\mathbf{x}_i,\mathbf{x}_{j_1},\mathbf{x}_{j_2})}{\partial\mathbf{x}_{j_1}}\bigg|_{\overline{\mathbf{x}}} + \frac{\partial\mathbf{g}^{(2)}(\mathbf{x}_i,\mathbf{x}_{j_1},\mathbf{x}_{j_2})}{\partial\mathbf{x}_{j_2}}\bigg|_{\overline{\mathbf{x}}} = 0, \\
&\qquad\qquad\qquad\qquad\qquad\vdots \\
&\frac{\partial\mathbf{g}^{(M)}(\mathbf{x}_i,\mathbf{x}_{j_1},\dots,\mathbf{x}_{j_M})}{\partial\mathbf{x}_i}\bigg|_{\overline{\mathbf{x}}} + \frac{\partial\mathbf{g}^{(M)}(\mathbf{x}_i,\mathbf{x}_{j_1},\dots,\mathbf{x}_{j_M})}{\partial\mathbf{x}_{j_1}}\bigg|_{\overline{\mathbf{x}}} \\
&\qquad\qquad + \cdots + \frac{\partial\mathbf{g}^{(M)}(\mathbf{x}_i,\mathbf{x}_{j_1},\dots,\mathbf{x}_{j_M})}{\partial\mathbf{x}_{j_M}}\bigg|_{\overline{\mathbf{x}}} = 0.
\end{aligned} \tag{1.18}
$$

This property allows to write Eqs. (1.17) as

$$\delta \dot{\mathbf{x}}_i = J\mathbf{f}(\bar{\mathbf{x}})\delta \mathbf{x}_i - \sigma_1 \sum_{j_1} L_{ij_1}^{(1)} J_1 \mathbf{g}^{(1)}(\bar{\mathbf{x}})\delta \mathbf{x}_{j_1}$$

$$- \sigma_2 \sum_{j_1,j_2} \tau_{ij_1j_2}^{(2)} \left[J_1 \mathbf{g}^{(2)}(\bar{\mathbf{x}})\delta \mathbf{x}_{j_1} + J_2 \mathbf{g}^{(2)}(\bar{\mathbf{x}})\delta \mathbf{x}_{j_2} \right] \qquad (1.19)$$

$$- \cdots - \sigma_M \sum_{j_1,\ldots,j_M} \tau_{ij_1\ldots j_M}^{(M)} \left[J_1 \mathbf{g}^{(M)}(\bar{\mathbf{x}})\delta \mathbf{x}_{j_1} + \cdots + J_M \mathbf{g}^{(M)}(\bar{\mathbf{x}})\delta \mathbf{x}_{j_M} \right],$$

where $\mathbf{L}^{(1)}$ is the standard Laplacian matrix, and where we introduced the tensors $\mathbf{T}^{(m)}$, whose elements are given by $\tau_{ij_1\ldots j_m}^{(m)} = m!k(i)^{(m)}\delta_{ij_1\ldots j_m} - a_{ij_1\ldots j_m}^{(m)}$, being $k(i)^{(m)}$ is the generalized m-degree of node i, and $\delta_{ij_1\ldots j_m}$ the generalized multi-indexes Kronecker delta. Observe that in the case of directed higher-order interactions $k(i)^{(m)}$ is the generalized in-d-degree of node i. Note that we have also introduced a more compact notation for the partial derivatives of the coupling functions, namely

$$J_1 \mathbf{g}^{(1)}(\bar{\mathbf{x}}) = \left. \frac{\partial \mathbf{g}^{(1)}(\mathbf{x}_i, \mathbf{x}_{j_1})}{\partial \mathbf{x}_{j_1}} \right|_{\bar{\mathbf{x}}},$$

$$J_1 \mathbf{g}^{(2)}(\bar{\mathbf{x}}) = \left. \frac{\partial \mathbf{g}^{(2)}(\mathbf{x}_i, \mathbf{x}_{j_1}, \mathbf{x}_{j_2})}{\partial \mathbf{x}_{j_1}} \right|_{\bar{\mathbf{x}}}, \quad J_2 \mathbf{g}^{(2)}(\bar{\mathbf{x}}) = \left. \frac{\partial \mathbf{g}^{(2)}(\mathbf{x}_i, \mathbf{x}_{j_1}, \mathbf{x}_{j_2})}{\partial \mathbf{x}_{j_2}} \right|_{\bar{\mathbf{x}}}, \qquad (1.20)$$

$$\vdots$$

$$J_1 \mathbf{g}^{(M)}(\bar{\mathbf{x}}) = \left. \frac{\partial \mathbf{g}^{(M)}(\mathbf{x}_i, \mathbf{x}_{j_1}, \ldots, \mathbf{x}_{j_M})}{\partial \mathbf{x}_{j_1}} \right|_{\bar{\mathbf{x}}}, \ \ldots, \ J_M \mathbf{g}^{(M)}(\bar{\mathbf{x}}) \left. \frac{\partial \mathbf{g}^{(M)}(\mathbf{x}_i, \mathbf{x}_{j_1}, \ldots, \mathbf{x}_{j_M})}{\partial \mathbf{x}_{j_M}} \right|_{\bar{\mathbf{x}}}.$$

Eqs. (1.19) can be further simplified by using the symmetry properties of the adjacency tensors $\mathbf{A}^{(m)}$. Let us consider the summation relative to the $(m+1)$-body interactions, which we can write as

$$\sum_{j_1,\ldots,j_m} \tau_{ij_1\ldots j_m}^{(m)} \left[J_1 \mathbf{g}^{(m)}(\bar{\mathbf{x}})\delta \mathbf{x}_{j_1} + \cdots + J_m \mathbf{g}^{(m)}(\bar{\mathbf{x}})\delta \mathbf{x}_{j_m} \right] =$$

$$\sum_{j_1} J_1 \mathbf{g}^{(m)}(\bar{\mathbf{x}})\delta \mathbf{x}_{j_1} \sum_{j_2,\ldots,j_m} \tau_{ij_1\ldots j_m}^{(m)} + \cdots + \sum_{j_m} J_m \mathbf{g}^{(m)}(\bar{\mathbf{x}})\delta \mathbf{x}_{j_m} \sum_{j_1,\ldots,j_{m-1}} \tau_{ij_1\ldots j_m}^{(m)}. \qquad (1.21)$$

In the case of undirected higher-order structures, the adjacency tensors $\mathbf{A}^{(m)}$ are symmetric with respect to all their indexes, namely $a_{ij_1\ldots j_m}^{(m)} = a_{\pi(ij_1\ldots j_m)}^{(m)}$, with π a generic permutation of the indexes $\{i, j_1, \ldots, j_m\}$. This holds obviously true for the generalized multi-indexes Kronecker delta as

well. Therefore, the tensors $\mathbf{T}^{(m)}$ has the same symmetry property as the adjacency tensors $\mathbf{A}^{(m)}$. This allows to permute the indexes so to always sum $\mathbf{T}^{(m)}$ over its last $(m-1)$ indexes, thus yielding

$$\sum_{j_2,\ldots,j_m} \tau_{ij\ldots j_m}^{(m)} = \cdots = \sum_{j_1,\ldots,j_{m-1}} \tau_{ij_1\ldots j}^{(m)} = L_{ij}^{(m)}, \tag{1.22}$$

where we have denoted as j the index over which the tensor is not summed, and where $L_{ij}^{(m)}$ is the entry (i,j) of the generalized Laplacian matrix $\mathbf{L}^{(m)}$, defined in Eq. (1.6). Hence, we can write the term relative to the $(m+1)$-body interactions as

$$\sum_j J_1 \mathbf{g}^{(m)}(\overline{\mathbf{x}})\delta\mathbf{x}_j \sum_{j_2,\ldots,j_m} \tau_{ij\ldots j_m}^{(m)} + \cdots + \sum_j J_m \mathbf{g}^{(m)}(\overline{\mathbf{x}})\delta\mathbf{x}_j \sum_{j_1,\ldots,j_{m-1}} \tau_{ij_1\ldots j}^{(m)} =$$
$$\sum_j L_{ij}^{(m)} \left[J_1 \mathbf{g}^{(m)}(\overline{\mathbf{x}}) + \cdots + J_m \mathbf{g}^{(m)}(\overline{\mathbf{x}}) \right] \delta\mathbf{x}_j. \tag{1.23}$$

Note that this holds true also for 1-directed higher-order structures. In general, for directed structures the adjacency tensors $\mathbf{A}^{(m)}$ are not symmetric with respect to all their indexes. However, property (1.7) of 1-directionality still allows the derivation of generalized Laplacian matrices, as $\mathbf{T}^{(m)}$ is nevertheless symmetric under a permutation of its last m indexes, i.e., $\tau_{ij_1\ldots j_m}^{(m)} = \tau_{i\pi(j_1\ldots j_m)}^{(m)}$.

Finally, we can rewrite Eqs. (1.19) as

$$\delta\dot{\mathbf{x}}_i = \mathbf{JF}\delta\mathbf{x}_i - \sigma_1 \sum_j L_{ij}^{(1)} \mathbf{JG}^{(1)} \delta\mathbf{x}_j - \sigma_2 \sum_j L_{ij}^{(2)} \mathbf{JG}^{(2)} \delta\mathbf{x}_j$$
$$- \cdots - \sigma_M \sum_j L_{ij}^{(M)} \mathbf{JG}^{(M)} \delta\mathbf{x}_j, \tag{1.24}$$

where we have used the notation

$$\mathbf{JF} = J\mathbf{f}(\overline{\mathbf{x}}), \quad \mathbf{JG}^{(m)} = J_1 \mathbf{g}^{(m)}(\overline{\mathbf{x}}) + \cdots + J_m \mathbf{g}^{(m)}(\overline{\mathbf{x}}). \tag{1.25}$$

By introducing the stack vector $\delta\mathbf{x} = \left[\delta\mathbf{x}_1^T,\ldots,\delta\mathbf{x}_N^T\right]^T$, Eqs. (1.24) can be rewritten in block form, namely

$$\delta\dot{\mathbf{x}} = \left[\mathbb{I}_N \otimes \mathbf{JF} - \sigma_1 \mathbf{L}^{(1)} \otimes \mathbf{JG}^{(1)} - \sigma_2 \mathbf{L}^{(2)} \otimes \mathbf{JG}^{(2)} - \cdots - \sigma_M \mathbf{L}^{(M)} \otimes \mathbf{JG}^{(M)} \right] \delta\mathbf{x}, \tag{1.26}$$

where $\mathbb{I}_N$ is the identity matrix of size N, and $\otimes$ denotes the Kronecker product. Eq. (1.26) can be rewritten in a more explicit form, namely

$$
\frac{d}{dt}\begin{bmatrix} \delta\mathbf{x}_1 \\ \delta\mathbf{x}_2 \\ \vdots \\ \delta\mathbf{x}_N \end{bmatrix} = \left\{ \begin{bmatrix} \mathbf{JF} & 0 & \dots & 0 \\ 0 & \mathbf{JF} & \dots & 0 \\ \vdots & \vdots & \ddots & \vdots \\ 0 & 0 & \dots & \mathbf{JF} \end{bmatrix} - \right.
$$

$$
-\sigma_1 \begin{bmatrix} L_{11}^{(1)}\mathbf{JG}^{(1)} & L_{12}^{(1)}\mathbf{JG}^{(1)} & \dots & L_{1N}^{(1)}\mathbf{JG}^{(1)} \\ L_{21}^{(1)}\mathbf{JG}^{(1)} & L_{22}^{(1)}\mathbf{JG}^{(1)} & \dots & L_{2N}^{(1)}\mathbf{JG}^{(1)} \\ \vdots & \vdots & \ddots & \vdots \\ L_{N1}^{(1)}\mathbf{JG}^{(1)} & L_{N2}^{(1)}\mathbf{JG}^{(1)} & \dots & L_{NN}^{(1)}\mathbf{JG}^{(1)} \end{bmatrix} -
$$

$$
-\sigma_2 \begin{bmatrix} L_{11}^{(2)}\mathbf{JG}^{(2)} & L_{12}^{(2)}\mathbf{JG}^{(2)} & \dots & L_{1N}^{(2)}\mathbf{JG}^{(2)} \\ L_{21}^{(2)}\mathbf{JG}^{(2)} & L_{22}^{(2)}\mathbf{JG}^{(2)} & \dots & L_{2N}^{(2)}\mathbf{JG}^{(2)} \\ \vdots & \vdots & \ddots & \vdots \\ L_{N1}^{(2)}\mathbf{JG}^{(2)} & L_{N2}^{(2)}\mathbf{JG}^{(2)} & \dots & L_{NN}^{(2)}\mathbf{JG}^{(2)} \end{bmatrix} - \quad (1.27)
$$

$$
\vdots
$$

$$
\left. -\sigma_M \begin{bmatrix} L_{11}^{(M)}\mathbf{JG}^{(M)} & L_{12}^{(M)}\mathbf{JG}^{(M)} & \dots & L_{1N}^{(M)}\mathbf{JG}^{(M)} \\ L_{21}^{(M)}\mathbf{JG}^{(M)} & L_{22}^{(M)}\mathbf{JG}^{(M)} & \dots & L_{2N}^{(M)}\mathbf{JG}^{(M)} \\ \vdots & \vdots & \ddots & \vdots \\ L_{N1}^{(M)}\mathbf{JG}^{(M)} & L_{N2}^{(M)}\mathbf{JG}^{(M)} & \dots & L_{NN}^{(M)}\mathbf{JG}^{(M)} \end{bmatrix} \right\} \begin{bmatrix} \delta\mathbf{x}_1 \\ \delta\mathbf{x}_2 \\ \vdots \\ \delta\mathbf{x}_N \end{bmatrix}
$$

System (1.26) is composed by N coupled equations. In analogy with the network case, the next step would be to find a proper transformation of variables that allows to decouple the system. In particular, this means to find an eigenvector basis on which to project Eqs. (1.26). However, this is not possible in general, as the generalized Laplacian matrices do not always commute, and so the sets of eigenvectors are different from one another. Nevertheless, given the properties of the Laplacian matrices one is still able to separate the mode corresponding to the linearized dynamics of the isolated system from the others. In the context of synchronization, this means that it is possible to decouple the motion along the synchronous state and that transverse to it, while in that of Turing pattern formation, it means that one can decouple the space-independent part of the system from the spatial one. In facts, assuming at least one Laplacian matrix to be diagonalizable, since they are zero-row sum, they

all share, as the smallest eigenvalue, $\lambda_1^{(m)} = 0$, whose associated eigen-vector $[1, 1, \ldots, 1]^T / \sqrt{N}$ is parallel to the vector field defining the isolated system. All other eigenvectors, though different from one Laplacian to another, are associated to the transverse modes. Now, as a perturbation $\delta\mathbf{x}$ can be written as a linear combination of any of such eigenvector sets, we can arbitrarily choose any of them as the reference basis of the transverse space, and map all other eigenvector sets to such a basis. Let us then consider, as reference basis, the one constituted by the eigenvectors of the standard Laplacian $\mathbf{L}^{(1)}$, that we denote as $\{\mathbf{v_1}, \mathbf{v_2}, \ldots, \mathbf{v_N}\}$. By defining the new variables $\eta = (\mathbf{V}^{-1} \otimes \mathbb{I}_d)\delta\mathbf{x}$, where $\mathbf{V} = [\mathbf{v_1}, \ldots, \mathbf{v_N}]$, we can rewrite Eq. (1.26) as

$$\dot{\eta} = \left[\mathbb{I}_N \otimes \mathbf{JF} - \sigma_1 \mathbf{\Lambda}^{(1)} \otimes \mathbf{JG}^{(1)} - \sigma_2 \widetilde{\mathbf{L}}^{(2)} \otimes \mathbf{JG}^{(2)} - \cdots - \sigma_M \widetilde{\mathbf{L}}^{(M)} \otimes \mathbf{JG}^{(M)} \right] \eta_i, \quad (1.28)$$

where $\mathbf{V}^{-1}\mathbf{L}^{(1)}\mathbf{V} = \mathbf{\Lambda}^{(1)} = \mathrm{diag}(\lambda_1^{(1)}, \lambda_2^{(1)}, \ldots, \lambda_N^{(1)})$, being $0 = \lambda_1^{(1)} \leq \lambda_2^{(1)} \leq \cdots \leq \lambda_N^{(1)}$ the eigenvalues of $\mathbf{L}^{(1)}$, and where $\widetilde{\mathbf{L}}^{(m)} = \mathbf{V}^{-1}\mathbf{L}^{(m)}\mathbf{V}$ is the transformed generalized Laplacian of order m. As the generalized Laplacian matrices are zero-row sum, we can write Eq. (1.28) as

$$\dot{\eta}_1 = \mathbf{JF}\eta_1,$$
$$\dot{\eta}_i = \left(\mathbf{JF} - \sigma_1 \lambda_i^{(1)} \mathbf{JG}^{(1)} \right) \eta_i - \sigma_2 \sum_{j=2}^{N} \widetilde{\mathbf{L}}_{ij}^{(2)} \mathbf{JG}^{(2)} \eta_j - \cdots - \sigma_M \sum_{j=2}^{N} \widetilde{\mathbf{L}}_{ij}^{(M)} \mathbf{JG}^{(M)} \eta_j. \quad (1.29)$$

with $i \in \{2, \ldots, N\}$. Observe that the equations governing the system dynamics are now split in two parts. The first equation, which is decoupled from the others, is the linearized dynamics of the isolated system. The remaining $N - 1$ coupled equations describes instead the dynamics along the directions transverse to the vector field governing the dynamics of the isolated system. Hence, though it is not possible in general to decouple completely the system of equations, we are still able to study the stability of state $\bar{\mathbf{x}}$ numerically. Indeed, from the equation governing the dynamics of the isolated system we can evaluate $\bar{\mathbf{x}}$, from which we can estimate the Jacobian matrices $\mathbf{JF}$ and $\mathbf{JG}^{(m)}$, with $m \in \{1, \ldots, M\}$. We can then simulate the system of $N - 1$ coupled linear equations, and calculate the maximum Lyapunov exponent Λ_{max} associated to the transverse modes from the norm $\sqrt{\sum_{i=2}^{N} ||\eta_i||^2}$. Hence, being Λ_{max} negative is a necessary condition for the stability of $\bar{\mathbf{x}}$.

Hence, analogously to the case of networks, also for higher-order structures we are able to perform a separation of the mode parallel to the vector field defining the isolated system and of those transerve to it, which allows us to analyze the stability of state $\bar{\mathbf{x}}$. However, the greater complexity of higher-order structures does not enable in general to further decouple the system of equations and to write a single parametric Master Stability Equation. It is worth mentioning that the inability of decoupling the transverse modes does not characterize higher-order structures only, but it represents an issue for the analysis of dynamical systems in temporal networks [31, 139], hypernetworks [140], and multilayer networks [32, 141], among others. Nonetheless, as it always possible to separate the tangent and the transverse motions, the analysis still reduces to the (numerical) computation of a single quantity determining the stability of $\bar{\mathbf{x}}$. However, there are few special cases where either the topology of the higher-order structure or the functional form of the couplings allow to fully decouple the equations governing the transverse modes, so to derive a parametric variational equation whose solution, i.e., the Master Stability Function, determines the stability of the system.

1.3.1 Commutative generalized Laplacian matrices

Since the Laplacian matrices encoding the different orders of interactions do not commute in general, it is not possible to entirely decouple system (1.26). As we will soon discuss, there are, however, examples of topologies for which the Laplacian matrices commute. A set of commuting (diagonalizable) matrices share the same set of eigenvectors, meaning that we can simultaneously diagonalize each generalized Laplacian matrix, namely

$$\mathbf{\Lambda}^{(m)} = \mathbf{V}^{-1}\mathbf{L}^{(m)}\mathbf{V}, \ \forall m \in \{1, \dots, M\}, \tag{1.30}$$

where $\mathbf{\Lambda}^{(m)} = \text{diag}(\lambda_1^{(m)}, \lambda_2^{(m)}, \dots, \lambda_N^{(m)})$. Note that, in the case of undirected higher-order topologies, every eigenvalue $\lambda_i^{(m)}$ is real, while for directed structures the eigenvalues are in general complex. Holding Eq. (1.30),

we can rewrite Eq. (1.29) as

$$
\begin{aligned}
\dot{\eta}_1 &= \mathbf{JF}\eta_1, \\
\dot{\eta}_i &= \left(\mathbf{JF} - \sigma_1 \lambda_i^{(1)} \mathbf{JG}^{(1)} - \sigma_2 \lambda_i^{(2)} \mathbf{JG}^{(2)} - \cdots - \sigma_M \lambda_i^{(M)} \mathbf{JG}^{(M)} \right) \eta_i.
\end{aligned}
\tag{1.31}
$$

We observe that the equations relative to the transverse modes all have the same form. Hence, we can subsume them in a single parametric variational equation, which is

$$
\begin{aligned}
\dot{\zeta} = \big[\mathbf{JF} &- (\alpha^{(1)} + i\beta^{(1)})\mathbf{JG}^{(1)} - \\
&- (\alpha^{(2)} + i\beta^{(2)})\mathbf{JG}^{(2)} - \\
&- \cdots - (\alpha^{(M)} + i\beta^{(M)})\mathbf{JG}^{(M)} \big] \zeta,
\end{aligned}
\tag{1.32}
$$

where $\alpha^{(m)} + i\beta^{(m)}$, $\forall m \in \{1, \ldots, M\}$ are complex-valued parameters, as in general the eigenvalues of the Laplacian matrices can be complex. From Eq. (1.32) we can calculate the Lyapunov exponent. Compared to the network case, where the maximum Lyapunov exponent is a function of a single complex parameter, i.e., $\Lambda_{\max} = \Lambda_{\max}(\alpha + i\beta)$, for higher-order structures of order M, the MSF is a function of M complex parameters, namely $\Lambda_{\max} = \Lambda_{\max}(\alpha^{(1)} + i\beta^{(1)}, \ldots, \alpha^{(M)} + i\beta^{(M)})$. Hence, if $\Lambda_{\max} < 0$ in each point $[\sigma_1 \lambda_i^{(1)}, \ldots, \sigma_M \lambda_i^{(M)}]$ in the $2M$-dimensional complex space, state $\bar{\mathbf{x}}$ is stable. In the contest of synchronization, this is a necessary condition for the onset of synchronization itself. On the other hand, if $\Lambda_{\max} > 0$ for some point $[\sigma_1 \lambda_i^{(1)}, \ldots, \sigma_M \lambda_i^{(M)}]$, then $\bar{\mathbf{x}}$ is unstable. In the context of Turing theory, this is a necessary and sufficient condition for the formation of patterns.

We here illustrate some examples where the generalized Laplacian matrices commute. Let us first consider the case of an undirected higher-order structure with N nodes where only two and three-body interactions are present, i.e., $M = 2$. If all the two-body interactions are active, i.e., $A_{ij}^{(1)} = 1$, $\forall i \neq j$, then no matter the structure of the three-body interactions the generalized Laplacian matrices $\mathbf{L}^{(1)}$ and $\mathbf{L}^{(2)}$ will commute. In facts, it is simple to prove that the Laplacian matrix of the complete graph, i.e., $\mathbf{L}^{(1)}$, commutes with any other Laplacian matrix $\mathbf{L}^{(m)}$. Indeed,

the elements of the standard Laplacian matrix in the all-to-all coupling configuration are given by

$$L_{ij}^{(1)} = \begin{cases} N-1 & \text{for } i = j, \\ -1 & \text{for } i \neq j. \end{cases} \tag{1.33}$$

Therefore, the element (i, j) of the product matrix $\mathbf{L}^{(1)}\mathbf{L}^{(m)}$ is given by

$$(\mathbf{L}^{(1)}\mathbf{L}^{(m)})_{ij} = \sum_k L_{ik}^{(1)} L_{kj}^{(m)} = (N-1)L_{ij}^{(m)} - \sum_{k \neq i} L_{kj}^{(m)} = NL_{ij}^{(m)} - \sum_k L_{kj}^{(m)} = NL_{ij}^{(m)}, \tag{1.34}$$

where we have used the property of zero-column sum of the Laplacian matrix of an undirected graph. Similarly, given that $\mathbf{L}^{(m)}$ is zero-row sum, we can show that the element (i, j) of $\mathbf{L}^{(m)}\mathbf{L}^{(1)}$ is equal to $NL_{ij}^{(m)}$, thus proving that $\mathbf{L}^{(1)}$ commutes with any other Laplacian matrix. Therefore, noting that in the all-to-all configuration the nonzero eigenvalues of the Laplacian matrix are $\lambda_2^{(1)} = \cdots = \lambda_N^{(1)} = N$, we can rewrite Eq. (1.32) in this case as

$$\dot{\zeta} = \left[\mathbf{JF} - \sigma_1 N \mathbf{JG}^{(1)} - \alpha^{(2)} \mathbf{JG}^{(2)} \right] \zeta, \tag{1.35}$$

where $\beta^{(2)} = 0$, as we are considering undirected three-body interactions. Hence, when all the two-body interactions are active, we find that the dependence of the MSF on the pairwise coupling is limited to the coupling strength σ_1 and the number of nodes N, i.e., $\Lambda_{\max} = \Lambda_{\max}(\sigma_1, N, \alpha^{(2)})$. Therefore, having fixed N and the strength of the two-body interactions, we can study the effect of the three-body interactions on the system stability through the parameter $\alpha^{(2)} = \sigma_2 \lambda_i^{(2)}$.

The property of the complete graph Laplacian matrix to commute with any other symmetric Laplacian matrix allows us to analyze some special cases with $M > 2$. Let us for instance consider the case $M = 3$, where the two-body interactions are in the all-to-all configuration. As above discussed, the matrices $\mathbf{L}^{(2)}$ and $\mathbf{L}^{(3)}$ do not commute in general. However, if we consider the case where all the possible three-body interactions are active, we find that $\mathbf{L}^{(2)}$ recovers the Laplacian matrix of the complete graph, thus allowing to decouple the equations for the dynamics of the transverse modes. In facts, the off-diagonal terms $L_{ij}^{(2)}$, with $i \neq j$ consist

in the number of three-body interactions of which the couple of nodes (i, j) are part of (see Eq. (1.6)) that in the three-body all-to-all configuration is simply $N - 2$, i.e., all the nodes in the network different from i and j. On the other hand, the diagonal terms $L_{ii}^{(2)}$ are proportional to the number of three-body interactions in which node i participates, which is given by

$$L_{ii}^{(2)} = \binom{N-1}{2} = \frac{(N-1)(N-2)}{2}.$$

(1.36)

Hence, when both the two-body and the three-body are in the all-to-all configuration we have

$$\mathbf{L}^{(2)} = (N-2)\mathbf{L}^{(1)},$$

(1.37)

from which it follows that, no matter the patterns of the four-body interactions, it is always possible to write a single parametric equation to study the stability of the system. Following this reasoning, we can show that we can write a single MSE for a M-dimensional higher-order structure every time all but one of the orders of interactions are in the all-to-all configuration. In facts, when all the $(m+1)$-body interactions are active, the corresponding generalized Laplacian $\mathbf{L}^{(m)}$ can be written as a function of the complete graph Laplacian matrix. In facts, we can calculate the number of $(m+1)$-body interactions in which node i partecipates and the number of $(m+1)$-body interactions of which nodes i and j are part of, namely

$$k_i^{(m)} = \binom{N-1}{m} = \frac{(N-1)(N-2)\dots(N-m)}{m!},$$

(1.38)

and

$$k_{ij}^{(m)} = \binom{N-2}{m-1} = \frac{(N-2)(N-3)\dots(N-m)}{(m-1)!},$$

(1.39)

from which, we can write the generalized Laplacian matrix for the $(m+1)$-body interactions as

$$\mathbf{L}^{(m)} = (N-2)(N-3)\dots(N-m)\mathbf{L}^{(1)}.$$

(1.40)

In particular, when all orders of interactions are in the all-to-all configuration, Eq. (1.32) can be rewritten as

$$\dot{\zeta} = \left[\mathbf{JF} - \sigma_1 N \mathbf{JG}^{(1)} - \sigma_2 N(N-2)\mathbf{JG}^{(2)} - \right.$$
$$\left. - \dots - \sigma_M N(N-2)\dots(N-M)\mathbf{JG}^{(M)} \right] \zeta.$$
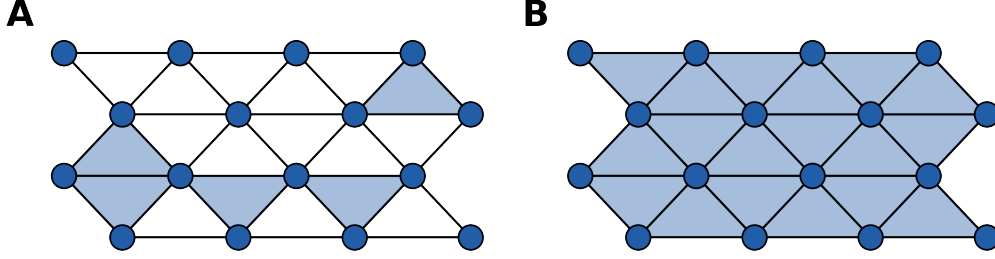
(1.41)

A

B

Figure 1.4: Comparison between a triangular lattice with a few three-body interactions active (panel A) and a 2-lattice, where all three-body interactions are present.

Once again, we have derived a single parametric equation, with the MSF that only depends on the coupling strengths $\sigma_1, \sigma_2, \ldots, \sigma_M$ and the number of nodes N, i.e. $\Lambda_{max} = \Lambda_{max}(\sigma_1, \sigma_2, \ldots, \sigma_M, N)$.

Another interesting example where the generalized Laplacian matrices commute is that of some regular topologies. This is the case, for instance, of a triangular lattice with periodic boundary conditions, where we assume the nodes forming a triangle also to interact via a three-body coupling. For this reason we will call it triangular 2-lattice. In this structure, each node interacts with its six neighbors through six two-body interactions and as many three-body interactions. From definition (1.6), we can show that for a triangular lattice with N nodes the Laplacian matrix $\mathbf{L}^{(2)}$ is a multiple of $\mathbf{L}^{(1)}$, namely

$$\mathbf{L}^{(2)} = 2\mathbf{L}^{(1)}, \tag{1.42}$$

where

$$L_{ij}^{(1)} = \begin{cases} 6 & \text{for } i = j, \\ -A_{ij}^{(1)} & \text{for } i \neq j. \end{cases} \tag{1.43}$$

Hence, for the triangular lattice case we can write the equations for the transverse modes as

$$\dot{\eta}_i = \left[\mathbf{JF} - \lambda_i^{(1)} \left(\sigma_1 \mathbf{JG}^{(1)} + 2\sigma_2 \mathbf{JG}^{(2)} \right) \right] \eta_i, \tag{1.44}$$

so that the MSF will be a function of the coupling strengths and of the eigenvalues of $\mathbf{L}^{(1)}$.

Though they enable an analytical treatment of the stability problem, the cases presented so far largely restrict the range of possible topologies one can consider. In particular, structures where the Laplacian matrices commute are unlikely to occur in practical situations [140]. Yet, they allow to have a certain flexibility in the choice of the coupling functions at different orders, as no further requirements are needed to obtain the Master Stability Equation. In the next section, we will consider the opposite case, imposing certain conditions on the coupling functions, while leaving more flexibility in the structure of interactions.

1.3.2 Natural coupling

When the Laplacian matrices for the different orders of interactions do not commute, it is still possible to decouple the equations for the transverse modes by imposing a few yet quite general conditions on the functional form of the couplings. The first step is to consider coupling functions $\mathbf{g}^{(m)}$ that are diffusive-like (see Eq. (1.14)). Under this choice of the couplings, one can follow the derivation presented above, again obtaining a block-form equation for the linearized system having the same form of Eqs. (1.26), namely

$$\delta \dot{\mathbf{x}} = \left[\mathbb{I}_N \otimes \mathbf{JF} - \sigma_1 \mathbf{L}^{(1)} \otimes \mathbf{JH}^{(1)} - \sigma_2 \mathbf{L}^{(2)} \otimes \mathbf{JH}^{(2)} - \cdots - \sigma_M \mathbf{L}^{(M)} \otimes \mathbf{JH}^{(M)} \right] \delta \mathbf{x}, \quad (1.45)$$

where we have introduced the notation, similar to the one in Eqs. (1.20) and (1.25)

$$\mathbf{JH}^{(m)} = \sum_{\ell=1}^{m} \left. \frac{\partial \mathbf{h}^{(m)}(\mathbf{x}_{j_1}, \dots, \mathbf{x}_{j_m})}{\partial \mathbf{x}_{j_\ell}} \right|_{\bar{\mathbf{x}}}. \quad (1.46)$$

In addition, we assume the coupling functions to respect the hypothesis of *natural coupling*, namely

$$\mathbf{h}^{(M)}(\mathbf{y}, \mathbf{y}, \dots, \mathbf{y}) = \cdots = \mathbf{h}^{(2)}(\mathbf{y}, \mathbf{y}) = \mathbf{h}^{(1)}(\mathbf{y}). \quad (1.47)$$

Basically, the natural coupling hypothesis consists in assuming that the influence that a unit experiences when interacting with a group of m
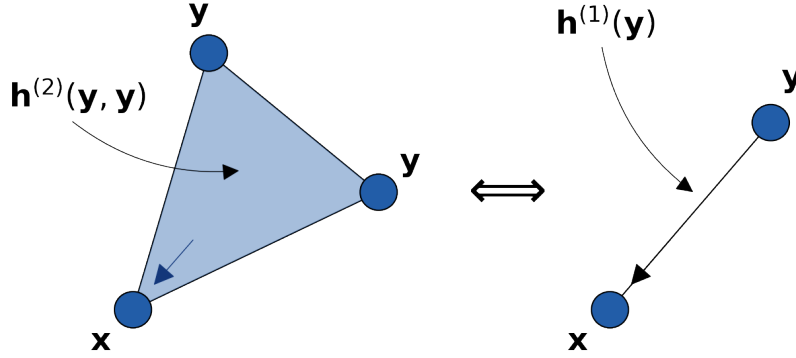
Figure 1.5: A graphical representation of the natural coupling hypothesis for three-body interactions. The influence that a node in a given state **x** receives from a couple of nodes in the same state **y** is equivalent to that the node would experience when interacting with a single node in state **y**.

units, all in the same state **y**, is equivalent to the one it would undergo when interacting with a single unit in state **y**. In other words, the influenced unit does not distinguish between different orders of interactions when affected by units in the same state. A graphical representation of the natural coupling hypothesis is displayed in Fig. 1.5. It is worth remarking that in the context of Turing pattern formation, the natural coupling hypothesis reads

$$
\begin{aligned}
D_u^{(M)} h_u^{(M)}(u, u, \ldots, u) &= \cdots = D_u^{(2)} h_u^{(2)}(u, u) = D_u^{(1)} h_u^{(1)}(u), \\
D_v^{(M)} h_v^{(M)}(v, v, \ldots, v) &= \cdots = D_v^{(2)} h_v^{(2)}(v, v) = D_v^{(1)} h_v^{(1)}(v).
\end{aligned}
\tag{1.48}
$$

Hence, if we consider the case $h_u^{(M)}(u, u, \ldots, u) = \cdots = h_u^{(2)}(u, u) = h_u^{(1)}(u)$ and $h_v^{(M)}(v, v, \ldots, v) = \cdots = h_v^{(2)}(v, v) = h_v^{(1)}(v)$, condition (1.48) implies that the diffusion coefficients at the various order of interaction

have to be equal, namely

$$
\begin{aligned}
D_u^{(M)} &= \cdots = D_u^{(2)} = D_u^{(1)}, \\
D_v^{(M)} &= \cdots = D_v^{(2)} = D_v^{(1)}.
\end{aligned}
\tag{1.49}
$$

The mathematical consequence of the natural coupling hypothesis is that the derivatives of the coupling functions $\mathbf{h}^{(m)}$ evaluated in state $\bar{\mathbf{x}}$ satisfy the relation

$$
\mathbf{JH}^{(M)} = \cdots = \mathbf{JH}^{(2)} = \mathbf{JH}^{(1)}.
\tag{1.50}
$$

Crucially, Eq. (1.50) allows us to greatly simplify Eq. (1.45), which we can write as

$$
\delta\dot{\mathbf{x}} = \left[\mathbb{I}_N \otimes \mathbf{JF} - \sigma_1 \mathcal{L} \otimes \mathbf{JH}^{(1)}\right] \delta\mathbf{x},
\tag{1.51}
$$

where we have introduced the *effective Laplacian matrix* $\mathcal{L}$, defined as

$$
\mathcal{L} = \mathbf{L}^{(1)} + r_2 \mathbf{L}^{(2)} + \cdots + r_M \mathbf{L}^{(M)}, \text{ with } r_i = \frac{\sigma_i}{\sigma_1}.
\tag{1.52}
$$

Note that, since all generalized Laplacian matrices are zero-row sum, it follows straightforwardly that the matrix $\mathcal{L}$ is zero-row sum as well. Hence, $\mathcal{L}$ represents the Laplacian matrix of an effective projected graph that encodes all the different orders of interactions. In facts, once fixed the ratios r_i, the equations governing the dynamics of the perturbations are formally equivalent to those of a system with weighted pairwise interactions among the units, coupling coefficient equal to σ_1, and a Laplacian matrix given by $\mathcal{L}$. In particular, from $\mathcal{L}$ we can evaluate the weighted adjacency matrix of the projected graph as $\mathcal{A} = \mathcal{D} - \mathcal{L}$, where $\mathcal{D}$ is a diagonal matrix whose elements are equal to the main diagonal of $\mathcal{L}$. However, it is crucial to remark that such an analogy between the two cases holds only in the linear regime, while no such an equivalence can be found in the nonlinear regime. As a consequence, while the linear stability in the two cases is equivalent, as determined by Eqs. 1.51, nothing can be said about the global stability analysis. An in-depth discussion about this aspect will be carried out in the Perspective section.

As an equivalent formulation, we can rewrite Eq. (1.51) as

$$
\delta\dot{\mathbf{x}} = \left[\mathbb{I}_N \otimes \mathbf{JF} - \widetilde{\mathcal{L}} \otimes \mathbf{JH}^{(1)}\right] \delta\mathbf{x},
\tag{1.53}
$$

with $\widetilde{\mathcal{L}}$ given by

$$\widetilde{\mathcal{L}} = \sigma_1 \mathbf{L}^{(1)} + \sigma_2 \mathbf{L}^{(2)} + \cdots + \sigma_M \mathbf{L}^{(M)}, \tag{1.54}$$

Both formulations are equivalent, so we will conclude the discussion on the linear stability analysis only referring to Eq. (1.51). Nonetheless, Eq. (1.53) will prove to be useful in the numerical analysis.

Assuming the effective Laplacian matrix $\mathcal{L}$ to be diagonalizable, we can finally project Eq. (1.45) onto its eigenvectors, thus fully decoupling the system in N linear equations. In particular, by defining the new variable $\eta = (\mathbf{V}^{-1} \otimes \mathbb{I}_d)\delta\mathbf{x}$, where $\mathbf{V}$ is the matrix whose columns are the eigenvectors of $\mathcal{L}$, we obtain

$$\dot{\eta}_i = \left[\mathbf{JF} - \sigma_1 \lambda_i \mathbf{JH}^{(1)} \right] \eta_i, \tag{1.55}$$

where $i \in \{1, \ldots, N\}$, and where $\lambda_1, \lambda_2, \ldots, \lambda_N$ are the eigenvalues of $\mathcal{L}$. Once again, the equation for $i = 1$ describes the linearized motion of the isolated system, while the other equations govern the motion of the transverse modes. As the equations for the transverse modes have the same form, we can finally write a single Master Stability Equation

$$\dot{\zeta} = \left[\mathbf{JF} - (\alpha + i\beta)\mathbf{JH}^{(1)} \right] \zeta. \tag{1.56}$$

The case of higher-order structure with coupling functions respecting the natural coupling hypothesis is substantially equivalent to that of networks. In fact, analogously to the network case, the maximum Lyapunov exponent is here a function of a single complex parameter, i.e., $\Lambda_{\max} = \Lambda_{\max}(\alpha + i\beta)$. Hence, $\Lambda_{\max} < 0$ where $\alpha + i\beta$ is any non-zero eigenvalue of $\mathcal{L}$ is a necessary condition for stability of state $\overline{\mathbf{x}}$.

It is here worth stressing that assuming that the effective Laplacian matrix $\mathcal{L}$ is diagonalizable, which can turn out to be quite a strong assumption in the case of directed higher-order interactions, is not essential to the linear stability analysis. In fact, to study the stability of the system dynamics one can extend the approach introduced in [142] for networks to higher-order structures. In particular, this mathematical framework, based on the Jordan block decomposition rather then on diagonalization, yields the derivation of the same condition on stability for non-

diagonalizable Laplacian matrices. Hence, the crucial aspect of the stability analysis is the identification of a matrix whose eigenvalues ultimately determine the robustness of the dynamics to perturbations.

As we have seen, when the natural coupling hypothesis holds, we are able to study the problem of the stability analytically, as it is possible to derive a single MSE with which the dynamics of the transverse modes can be studied. By giving up some flexibility on the choice of the interaction functions, the natural coupling allows us to study any higher-order structure, thus enabling to analyze more practical situations in which the connectivity has no restriction.

Chapter 2

Synchronization in symmetric high-order structures

In this chapter, we study the synchronization of coupled chaotic oscillators in presence of both pairwise and higher-order interactions that are reciprocal. We provide a series of numerical results that confirm the validity of the linear stability analysis described in the previous chapter. First, we start from the most general case where the Laplacian matrices associated to the different orders of interactions do not commute and where the coupling functions do not satisfy the natural coupling hypothesis. Focusing on the prototypical case of the Rössler oscillator [143], we analyze the contribution of the higher-order interactions on the stability of the synchronous state in several of higher-order motifs. In the same setting, we consider an example of neuron dynamics, analyzing a system of Hindmarsh-Rose oscillators [144], interacting through non-diffusive higher-order coupling functions. Next, we concentrate on those scenarios where it is possible to obtain a single Master Stability Equation for the study of synchronization. We first study a case where the Laplacian matrices for the different orders of interaction commute. Then, we concentrate on the natural coupling hypothesis, analyzing an example of synchronization in a generic higher-order topology. In particular, we will consider systems of coupled Rössler oscillators and of interacting Lorenz systems [145]. Finally, we analyze the differences in the synchronization behavior of undirected hypergraphs and simplicial complexes.

51

2.1 General case

In this section, we consider the most general setting where the Laplacian matrices encoding pairwise and higher-order interactions do not commute and where the natural coupling hypothesis does not hold. As a first example, we study the synchronization of a system of Rössler oscillators, whose dynamics is described by the equations

$$
\begin{aligned}
\dot{x} &= -y - z, \\
\dot{y} &= x + ay, \\
\dot{z} &= b + z(x - c).
\end{aligned}
\tag{2.1}
$$

Note that, using the notation introduced in the previous chapter, we have $\mathbf{x} = [x, y, z]^T \in \mathbb{R}^3$, and $\mathbf{f}(\mathbf{x}) = [-y - z, x + ay, b + z(x - c)]^T$. Here and in what follows, the parameters are fixed so to have a chaotic dynamics. In particular, we select $a = b = 0.2$, and $c = 9$ [26]. To show how the stability of the synchronous state is affected by the topology and the coupling functions, we concentrate on a few simple higher-order motifs, and we limit the choice of the coupling functions to a few examples. Moreover, for sake of clarity we limit our study to the case where only two-body and three-body interactions are active, though the more general case of a higher-order structure of order M can be analyzed in a similar way. In spite of these limitations, our analysis will allow us to highlight the variety of synchronization behaviors that can emerge from a system of units coupled through higher-order interactions.

We analyze five different settings, defined by different higher-order structures and coupling functions, which we label settings I to V. The motifs considered for the stability analysis are shown in Fig. 2.1. Let us remark that the three motifs are examples of simplicial complexes, so given a 2-simplex, i.e., a full triangle, all the possible 1-simplices, i.e., the links, exist. Observe that all the motifs here studied are formed by two 2-simplices connected to each other by sharing a couple of nodes (panel A), a single node (panel B), or none, being connected through a link in the latter case (panel C). In settings I, IV, and V, we consider the first motif, in setting II, we study the second, while in setting III, the third. Though in the following analysis we will focus on simplicial complexes, we remark
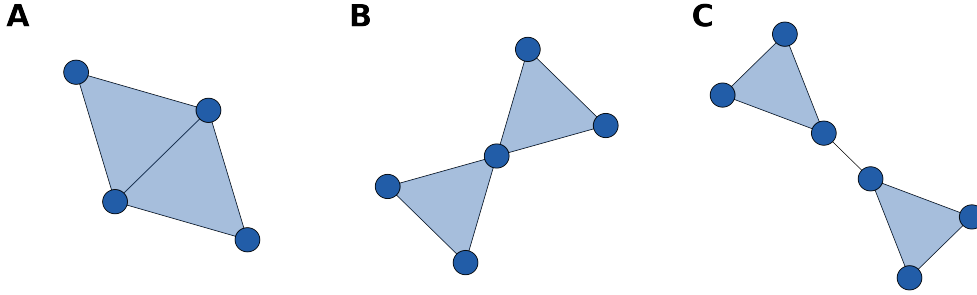
Figure 2.1: Motifs considered for the stability analysis. All motifs are formed by two 2-simplices connected to each other by sharing a couple of nodes (panel A), a single node (panel B), or none, being connected through a link in the latter case (panel C).

that the mathematical framework here developed is general enough to be applicable to hypergraphs.

As regards the interaction functions, we consider the classical diffusive coupling for the two-body interactions, while we take cubic diffusive-like functions for the three-body interactions. We remark that, in order to deal with an authentic multi-body dynamics, we need to consider, at least for the three-body interactions, nonlinear coupling functions, as discussed in Chapter 1. In more detail, for the two-body interactions we consider either $\mathbf{g}^{(1)}(\mathbf{x}_i, \mathbf{x}_j) = [x_j - x_i, 0, 0]^T$ in settings I to IV or $\mathbf{g}^{(1)}(\mathbf{x}_i, \mathbf{x}_j) = [0, y_j - y_i, 0]^T$ in setting V, while for the three-body interactions we take either $\mathbf{g}^{(2)}(\mathbf{x}_i, \mathbf{x}_j, \mathbf{x}_k) = [x_j^2 x_k - x_i^3, 0, 0]^T$ in settings I to III, and V or $\mathbf{g}^{(2)}(\mathbf{x}_i, \mathbf{x}_j, \mathbf{x}_k) = [0, y_j^2 y_k - y_i^3, 0]^T$ in setting IV. Tab. 2.1 summarizes the choices of the topology and of the coupling functions in the five settings considered. Note that, settings I to III deal with the same interaction functions bur with different higher-order motifs, while settings I, IV, and V, are characterized by the same topology and different couplings. This will allow us to analyze separately the role of the structure, and that of the form of interaction on synchronization.

As an illustrative example, let us here write in an explicit form the equations governing the dynamics of the system of Rössler oscillators arranged in setting (1), namely $N = 4$ oscillators disposed as in motif

Setting	Structure	$\mathbf{g}^{(1)}(\mathbf{x}_i, \mathbf{x}_j)$	$\mathbf{g}^{(2)}(\mathbf{x}_i, \mathbf{x}_j, \mathbf{x}_k)$
I	Motif A	$[x_j - x_i, 0, 0]^T$	$[x_j^2 x_k - x_i^3, 0, 0]^T$
II	Motif B	$[x_j - x_i, 0, 0]^T$	$[x_j^2 x_k - x_i^3, 0, 0]^T$
III	Motif C	$[x_j - x_i, 0, 0]^T$	$[x_j^2 x_k - x_i^3, 0, 0]^T$
IV	Motif A	$[x_j - x_i, 0, 0]^T$	$[0, y_j^2 y_k - y_i^3, 0]^T$
V	Motif A	$[0, y_j - y_i, 0]^T$	$[x_j^2 x_k - x_i^3, 0, 0]^T$

Table 2.1: Structural and functional characteristics of the settings considered in the numerical analysis of synchronization. The letters associated to the motifs correspond to the panel labels in Fig. 2.1.

A, interacting through the coupling functions $\mathbf{g}^{(1)}(\mathbf{x}_i, \mathbf{x}_j) = [x_j - x_i, 0, 0]^T$ and $\mathbf{g}^{(2)}(\mathbf{x}_i, \mathbf{x}_j, \mathbf{x}_k) = [x_j^2 x_k - x_i^3, 0, 0]^T$. The equations are

$$\dot{x}_i = -y_i - z_i + \sigma_1 \sum_{j=1}^{N} a_{ij}^{(1)}(x_j - x_i) + \sigma_2 \sum_{j,k=1}^{N} a_{ijk}^{(2)}(x_j^2 x_k - x_i^3),$$

$$\dot{y}_i = x_i + a y_i,$$
$$\dot{z}_i = b + z_i(x_i - c).$$

(2.2)

For each configuration considered, we integrate the corresponding set of dynamical equations for different values of the coupling strengths σ_1 and σ_2, and study whether the system of coupled oscillators synchronizes or not. To characterize the system behavior, we monitor the average synchronization error E, defined as

$$E = \left\langle \left(\frac{1}{N(N-1)} \sum_{i,j=1}^{N} \| \mathbf{x}_j - \mathbf{x}_i \|^2 \right)^{\frac{1}{2}} \right\rangle_T,$$

(2.3)

where T is a sufficiently large time interval over which the synchronization error is averaged, after having discarded a transient. For the present analysis, we integrate the system equations using an Euler algorithm, with integration step fixed to $\delta t = 10^{-4}$, for a time interval of length $2T$,
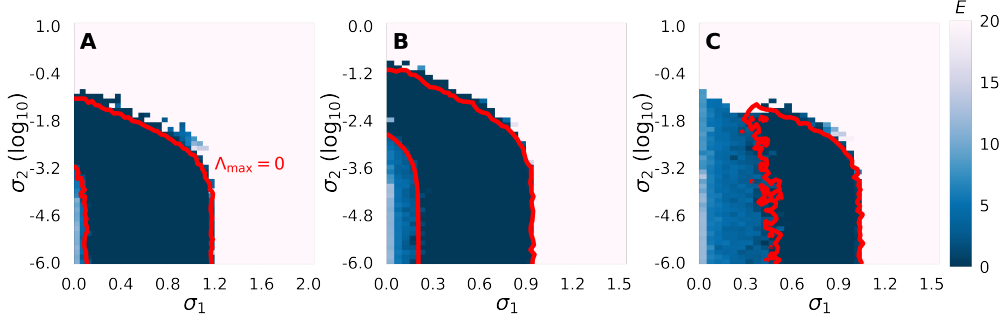
Figure 2.2: Contour plots of the average synchronization error E (Eq. (2.3)) in the plane (σ_1, σ_2) for the higher-order motifs in Fig. 2.1. Panels A to C display the results for settings I to III, respectively. The red continuous lines correspond to the theoretical prediction of the boundary of the stability regions, namely the points in the plane where $\Lambda_{max} = 0$.

where $T = 500$. We then compare the results obtained with the theoretical predictions. In particular, we evaluate the maximum Lyapunov exponent of the transverse modes, and we verify whether the area in the plane (σ_1, σ_2) for which $\Lambda_{max} < 0$ matches that where the average synchronization error goes to zero. To calculate Λ_{max} we use the Sprott's algorithm [146] (pp. 116-117). This consists in evaluating the temporal evolution of the average logarithmic separation of two trajectories starting from slightly different initial conditions, moving back one close to the other once they get too far apart. Such a procedure of letting evolve and readjusting the trajectories is repeated C times, and the Lyapunov exponent is evaluated as an average over these cycles. Here we use again an Euler algorithm to integrate the linearized system, setting the integration step to $\delta t = 10^{-3}$, while for the Sprott's algorithm we perform $I = 10^5$ iterations per cycle, and $C = 5$ number of cycles.

First, we study how the pattern of interactions affects synchronization having fixed the coupling functions. The results obtained for the analysis of settings I to III are reported in Fig. 2.2, in panels A to C, respectively. We observe that in all cases, the numerical simulations are in accordance with the theoretical predictions. In fact, the area of the (σ_1, σ_2) plane where the average synchronization error goes to zero is in good agree-
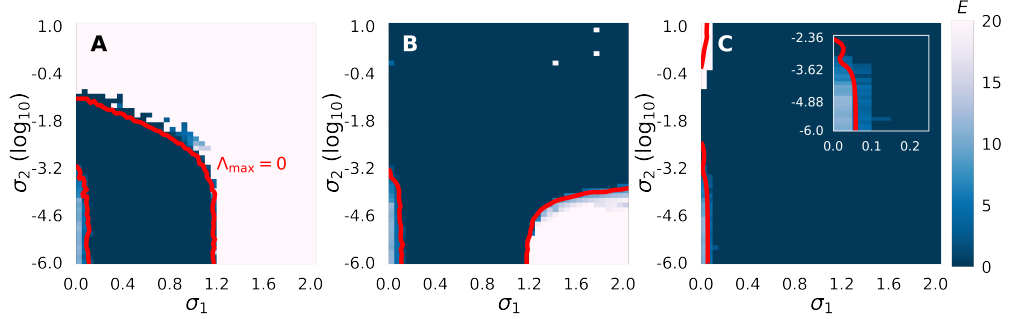
Figure 2.3: Contour plots of the average synchronization error E (Eq. (2.3)) in the plane (σ_1, σ_2) for different coupling functions. Panels A to C correspond to settings I, IV, and V, respectively. We consider a set of $N = 5$ systems arranged according to motif A of Fig. 2.1, with coupling functions reported in Tab. 2.1. The red continuous lines correspond to the theoretical prediction of the boundary of the stability regions, namely the points in the plane where $\Lambda_{max} = 0$. The inset in panel C represents a zoom of the area close to the origin.

ment with the area where the maximum Lyapunov exponent is negative, the boundary of which, defined by $\Lambda_{max} = 0$, is shown in the figure as a continuous red line. Moreover, we note that for all motifs the stability region is bounded. Therefore, according to the MSF classification usually adopted for the analysis of complex networks, this scenario represents the higher-order analogous of the so-called type III MSF, i.e., the MSF is negative in a closed interval of values [26, 49]. Finally, we notice that for motifs A and B synchronization may be achieved using either two-body or three-body interactions only, while for motif C the system does not synchronize for small values of σ_1, i.e., for weak two-body interactions. This is due to the structure of the higher-order motif. In fact, as the two 2-simplices do not have any node in common and they are connected by a single link, the corresponding two-body interaction becomes essential for the synchronization of the system, i.e., when $\sigma_1 \to 0$ the simplicial complex is substantially disconnected.

We now analyze the role of the coupling functions in the synchronization behavior of the system given a fixed higher-order structure (motif A).

The results obtained for the analysis of settings I, IV and V are reported in Fig. 2.3, in panels A to C, respectively. As for the previous study, the numerical simulations are in good agreement with the theoretical predictions, corroborating once again the validity of our analysis. Differently from the previous case, however, we observe that changing the coupling functions has dramatic effects on the shape of the stability region. Indeed, when Rössler oscillators are coupled on the x variable, both for the two-body and the three-body interactions, the stability region is bounded (panel A). However, when either the two-body or the three-body coupling is made on the y variable, the area of the (σ_1, σ_2) plane for which synchronization is achieved becomes, at least in the range of parameters considered, unbounded (panels B and C), a scenario that is the higher-order analogous of the type II MSF.

2.1.1 An application to neuron dynamics

Here we discuss a possible application of our mathematical framework, namely the study of synchronization of neuronal activities. In the context of neuron dynamics, the study of synchronization is of great relevance. In fact, on the one hand synchronized oscillations of neurons allow rapid formation of neural ensembles, which may underlie cognitive flexibility [147]. On the other hand, anomalous synchronization of neural oscillations is known to be associated to epileptic seizures [148, 149, 150]. Recent evidences in neuroscience have highlighted the existence of higher-order interactions in neuronal activity at both microscopic and macroscopic levels, though their importance in respect to pairwise interactions remains unclear for both the anatomical and the functional brain networks [82, 151, 152]. In particular, modeling neuron dynamics in presence of higher-order interactions is still an open problem. To show the potential of our mathematical framework in the study of neuronal activity, in this section we discuss an example of synchronization in an ensemble of neurons in presence of higher-order interactions.

In details, we study a system of coupled Hindmarsh-Rose (HR) oscillators, interacting through both two-body and three-body couplings. We

consider the system to be governed by the equations

$$\dot{x}_i = y_i - ax_i^3 + bx_i^2 - z_i + I + \sigma_1 \sum_{j=1}^{N} a_{ij}^{(1)} \tanh\left(\frac{x_j - x_i}{0.5}\right) +$$

$$+ \sigma_2 \sum_{j,k=1}^{N} a_{ijk}^{(2)} \tanh\left(\frac{x_j + x_k - 2x_i}{0.5}\right), \quad (2.4)$$

$$\dot{y}_i = c - dx_i^2 - y_i,$$
$$\dot{z}_i = -rz_i + rs(x_i - x_R),$$

where using again the notation introduced in the previous chapter, we have $\mathbf{x} = [x, y, z]^T \in \mathbb{R}^3$, and $\mathbf{f}(\mathbf{x}) = [y - ax^3 + bx^2 - z + I, c - dx^2 - y, -rz + rs(x - x_R)]^T$. The eight parameters of the model are here fixed to $a = c = 1$, $b = 3$, $d = 5$, $r = 0.006$, $s = 4$, $x_R = -8/5$, and $I = 16/5$ [49, 153]. Let us remark that we have chosen the interaction functions not to be diffusive-like, i.e., they can not be written as in Eq. (1.14). On the one hand, the coupling on the membrane potential, i.e., the x variable, through hyperbolic tangents accounts for possible saturation phenomena in the diffusion. On the other hand, this choice gives us the opportunity to prove the validity of our theoretical framework in the case of couplings that are not diffusive-like. We remark that this generalizes the standard MSF approach, where only diffusive-like functions are considered.

As for the previous section, we integrate Eqs. (2.4) for different sets of σ_1 and σ_2, monitoring the synchronization of the system using the average synchronization error (2.3). To integrate the system equations we use an Euler algorithm, with integration step $\delta t = 10^{-4}$, for a time interval of length $2T$, with $T = 500$. Again, the results obtained are compared with the theoretical predictions, by verifying if the area in the plane (σ_1, σ_2) for which $\Lambda_{\max} < 0$ predicts the sets of coupling strength values for which E goes to zero. $\Lambda_{\max}$ is once again calculated using the Sprott's algorithm, using an Euler algorithm to integrate the linearized system, setting the integration step to $\delta t = 10^{-3}$, and performing $I = 10^5$ iterations per cycle, and $C = 5$ number of cycles.

We study the synchronization behavior of system (2.4) by coupling the HR oscillators according to the motifs displayed in Fig. 2.1. The results obtained for the three settings are shown in Fig. 2.4, in panels A
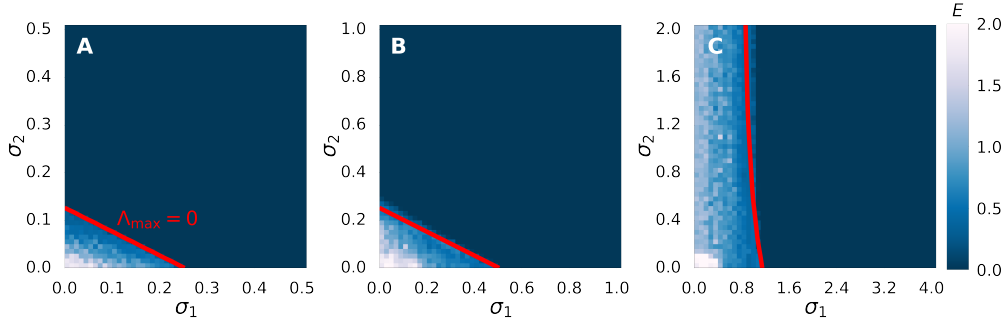
Figure 2.4: Contour plots of the average synchronization error E (Eq. (2.3)) in a system of coupled HR oscillators, in the plane (σ_1, σ_2), for the higher-order motifs displayed in Fig. 2.1. The red continuous lines correspond to the theoretical prediction of the boundary of the stability regions, namely the points in the plane where $\Lambda_{max} = 0$.

to C, respectively. Once again, we see that our theoretical framework is able to predict the sets (σ_1, σ_2) for which the synchronous state is stable. In particular, we observe that synchronization in neuronal activity is achieved in an unbounded region of the coupling coefficients considered (type II MSF). Additionally, we remark that three-body interactions play a positive role in synchronization, as they lower the value of the pairwise coupling strength necessary to achieve it. Our results point out that higher-order interactions may enhance the synchronization of coupled neurons, paving the way for further studies on the topic [154].

2.2 Structures with commuting Laplacian matrices

We now analyze those cases where it is possible to fully decouple the equations governing the perturbations transverse to the synchronous state, and so to derive a Master Stability Function for synchronization of systems with higher-order interactions. To begin with, in this section we numerically investigate the scenario where the Laplacian matrices associated to the different orders of interactions commute. In the next section
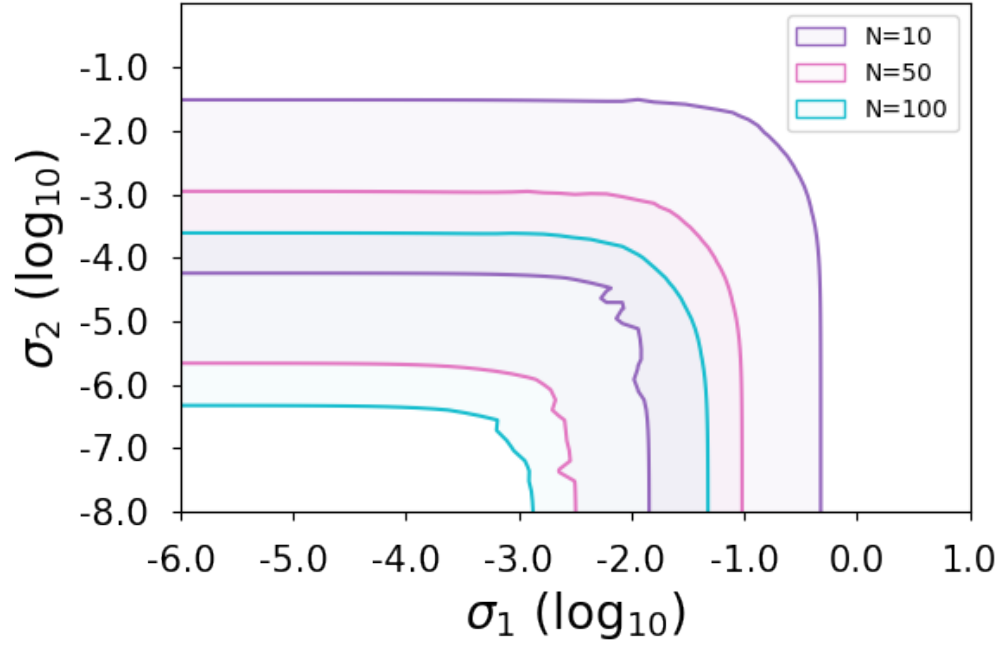
Figure 2.5: Stability regions of the synchronous manifold in the all-to-all configuration for different values of N. The shaded areas correspond to the values of the coupling coefficients σ_1 and σ_2 where the maximum Lyapunov exponent associated to the transverse modes is negative.

we will instead consider the case of natural coupling.

We consider the case where both the pairwise and the higher-order couplings are in the all-to-all configuration. We account for a system of Rössler oscillators, coupled via diffusive-like interaction functions, with $\mathbf{h}^{(1)}(\mathbf{x}_j) = [x_j, 0, 0]^T$ and $\mathbf{h}^{(2)}(\mathbf{x}_j, \mathbf{x}_k) = [x_j^2 x_k, 0, 0]^T$, for the two-body and three-body couplings, respectively. Note that these functions do not satisfy the natural coupling hypothesis. In this setting, the equation govern-

ing can be simply rewritten as

$$\dot{x}_i = -y_i - z_i + \sigma_1 \sum_{j=1,j\neq i}^{N} (x_j - x_i) + \sigma_2 \sum_{j,k=1,j\neq k\neq i}^{N} (x_j^2 x_k - x_i^3),$$

$$\dot{y}_i = x_i + ay_i,$$

$$\dot{z}_i = b + z_i(x_i - c).$$

(2.5)

As discussed in Chapter 1, in this setting the MSF only depends on the coupling strengths σ_1,σ_2, and on the number of nodes N (see Eg. (1.41)). Therefore, to analyze the synchronization behavior of the system, we evaluate the MSF in the plane (σ_1, σ_2) for three different values of N, namely $N = 10$, $N = 50$, and $N = 100$. For the calculation of the MSF we use the Wolf's algorithm [155]. This consists in evaluating a single trajectory of the nonlinear system, taking a reference point along it, finding its nearest neighbor, and measuring the temporal evolution of the distance between the two, until this exceeds a certain threshold value. Such a procedure is repeated multiple times, each time re-choosing the nearest neighbor of the reference point. The maximum Lyapunov exponent is computed as the temporal average of the logarithmic separation between the two points. For the present analysis, we use an Euler algorithm with integration step size $\delta t = 10^{-5}$, with simulation length equal to $L = 2500$, averaging over a time window of length $T = 0.9L$.

The results of our analysis are shown in Fig. 2.5, where the colored areas represent the values of the coupling coefficients for which $\Lambda_{\max} < 0$. We find a type III MSF, with the stability region that moves toward the origin as the number of nodes is increased. In other words, the bigger the network, hence the larger the number of two-body and three-body interactions, the lower the threshold values of σ_1 and σ_2 for which synchronization emerges. Such a result clearly highlihgts the role of the system size on synchronization. In fact, the number of nodes, as well as the average degree, can bias graph measures. Therefore, a direct comparisons between (empirical) networks with different number of nodes or different density may yield spurious results, thus making crucial to deal with these and other possible sources of biases [156, 157]. A systematic analysis of how the size of the network and the average generalized degrees affect synchronization in presence of higher-order interactions will be carried

out in future studies.

2.3   Natural coupling functions

To conclude the analysis of synchronization in undirected higher-order structures, here we study the case of natural coupling. As discussed in the previous chapter, the natural coupling hypothesis allows us to derive a MSF that is function of a single parameter $\alpha = \sigma_1 \lambda(\mathcal{L})$, where σ_1 is the strength of the pairwise coupling, while $\lambda(\mathcal{L})$ is the set of eigenvalues of an effective Laplacian matrix encoding all orders of interactions (see definition (1.52)). We remark that, under the natural coupling hypothesis, the Master Stability Function for synchronization in higher-order structures is formally analogous to that obtained for complex networks.

To begin with, we calculate the MSF for the Rössler oscillator and for the Lorenz system with different choices of the coupling functions, all satisfying the natural coupling hypothesis. The dynamics of the former is described by Eq. (2.1), while the Lorenz system is represented by

$$
\begin{aligned}
\dot{x} &= \sigma(y - x), \\
\dot{y} &= x(\rho - z) - y, \\
\dot{z} &= xy - \beta z,
\end{aligned}
\tag{2.6}
$$

where we fix the parameters so that the dynamics is chaotic, namely $\sigma = 10$, $\rho = 28$, and $\beta = 8/3$ [145]. For both models, we calculate the MSF for nine coupling configurations. In particular, we account for two-body and three-body interactions, coupling either the same oscillator components, e.g., the x-component of an oscillator influences the x-component of another, or different components, e.g., the y-component of an oscillator influences the x-component of another. Hereby, we use the notation $v \to w$, with $v, w \in \{x, y, z\}$ to denote the coupling scheme where the w-component of an oscillator is influenced by the v-component of the others. Tab. 2.2 summarizes the form of the coupling functions $\mathbf{h}^{(1)} = \mathbf{h}^{(1)}(\mathbf{x}_j)$ and $\mathbf{h}^{(2)} = \mathbf{h}^{(2)}(\mathbf{x}_j, \mathbf{x}_k)$ in the nine configurations considered. For the calculation of the MSF we use again the Wolf's algorithm, exploiting an Euler algorithm with integration step size $\delta t = 10^{-5}$, with

Influencing component

		x	y	z
Influenced component	x	$\mathbf{h}^{(1)} = [x_j^3, 0, 0]^T$ $\mathbf{h}^{(2)} = [x_j^2 x_k, 0, 0]^T$	$\mathbf{h}^{(1)} = [y_j^3, 0, 0]^T$ $\mathbf{h}^{(2)} = [y_j^2 y_k, 0, 0]^T$	$\mathbf{h}^{(1)} = [z_j^3, 0, 0]^T$ $\mathbf{h}^{(2)} = [z_j^2 z_k, 0, 0]^T$
	y	$\mathbf{h}^{(1)} = [0, x_j^3, 0]^T$ $\mathbf{h}^{(2)} = [0, x_j^2 x_k, 0]^T$	$\mathbf{h}^{(1)} = [0, y_j^3, 0]^T$ $\mathbf{h}^{(2)} = [0, y_j^2 y_k, 0]^T$	$\mathbf{h}^{(1)} = [0, z_j^3, 0]^T$ $\mathbf{h}^{(2)} = [0, z_j^2 z_k, 0]^T$
	z	$\mathbf{h}^{(1)} = [0, 0, x_j^3]^T$ $\mathbf{h}^{(2)} = [0, 0, x_j^2 x_k]^T$	$\mathbf{h}^{(1)} = [0, 0, y_j^3]^T$ $\mathbf{h}^{(2)} = [0, 0, y_j^2 y_k]^T$	$\mathbf{h}^{(1)} = [0, 0, z_j^3]^T$ $\mathbf{h}^{(2)} = [0, 0, z_j^2 z_k]^T$

Table 2.2: Coupling configurations considered for the calculation of the MSF for the Rössler oscillator and for the Lorenz system, in the case of natural coupling.

simulation length equal to $L = 2500$, averaging over a time window of length $T = 0.9L$.

The MSFs for the different coupling configurations are shown in Fig. 2.6 for the Rössler oscillator, and in Fig. 2.7 for the Lorenz system. Note that the arrangement of the panels in both figures follows the one of Tab. 2.2, so that the coupling functions considered for the calculation of the MSF are the ones reported in the corresponding table entry, e.g., panel A shows the results obtained for $\mathbf{h}^{(1)}(\mathbf{x}_j) = [x_j^3, 0, 0]^T$ and $\mathbf{h}^{(2)}(\mathbf{x}_j, \mathbf{x}_k) = [x_j^2 x_k, 0, 0]^T$. For both systems considered, we observe different types of MSF. In particular, for the Rössler oscillator we find that configuration $x \to x$ yields a type III MSF (panel A), while configuration $y \to y$ a type II MSF (panel E). Interestingly, the same behavior was observed also for coupling functions not respecting the natural coupling hypothesis (see Fig. 2.3 for a comparison). The remaining coupling schemes lead to type I MSFs. As regards the Lorenz system, we again observe a variety of synchronization behaviors. In particular, configurations $x \to x$, $x \to y$,and $y \to y$ yield a type II MSF (panels A, D and E, respectively), while configuration $y \to x$ yields a type III MSF. Additionally, we observe that for configuration $z \to z$ the MSF assumes negative values in two different in-
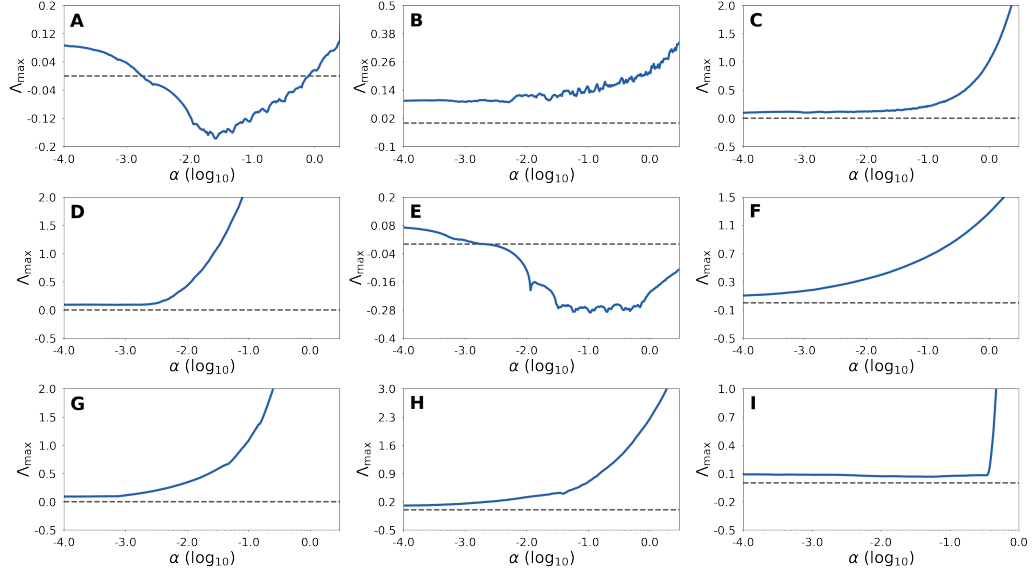
Figure 2.6: MSFs for the Rössler oscillator using different interaction functions satisfying the natural coupling hypothesis.

tervals of α, the first of which is bounded, while the second is unbounded (panel I). All remaining coupling schemes yield type I MSFs.

Next, we prove the validity of our theoretical analysis on a real-world complex structure. In particular, we study the synchronization of a system of Rössler oscillators coupled through a higher-order extension of the paradigmatic Zachary's karate club network. The original structure consists of $N = 34$ nodes connected by 78 links, forming a total of 45 triangles, here meant as a triple of fully connected nodes. Starting from this network, we can generate a simplicial complex by "filling" a fraction p_H of triangles, which means to assume that a fraction of the node triples interacting through two-body couplings also interact with three-body couplings.

We account for diffusive-like interaction functions, with $\mathbf{h}^{(1)}(\mathbf{x}_j) = [x_j^3, 0, 0]^T$ and $\mathbf{h}^{(2)}(\mathbf{x}_j, \mathbf{x}_k) = [x_j^2 x_k, 0, 0]^T$, that satisfy the natural coupling hypothesis. Under these assumptions, the dynamics of each node i is
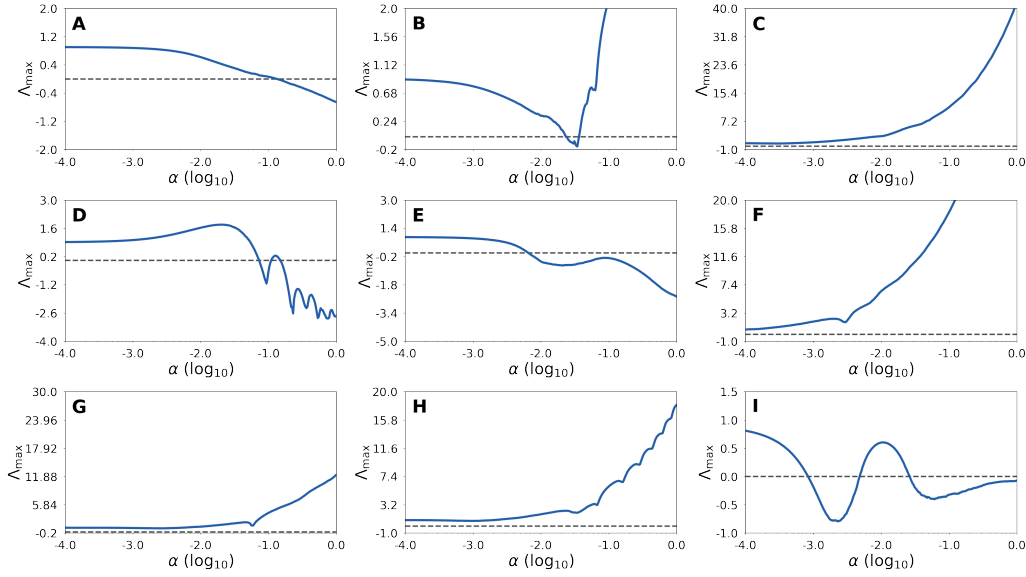
Figure 2.7: MSFs for the Lorenz system using different interaction functions satisfying the natural coupling hypothesis.

governed by the equations

$$
\dot{x}_i = -y_i - z_i + \sigma_1 \sum_{j=1}^{N} a_{ij}^{(1)} (x_j^3 - x_i^3) + \sigma_2 \sum_{j,k=1}^{N} a_{ijk}^{(2)} (x_j^2 x_k - x_i^3),
$$
$$
\dot{y}_i = x_i + a y_i,
$$
$$
\dot{z}_i = b + z_i (x_i - c).
$$

(2.7)

We integrate Eqs. (2.7) for different values of the coupling coefficients σ_1 and σ_2, monitoring the state of the system using the average synchronization error E. To integrate the system equations we use an Euler algorithm, with integration step $\delta t = 10^{-4}$, for a time interval of length $2T$, with $T = 500$. We then compare the results obtained with the theoretical predictions, checking whether the synchronization behavior is predicted by the MSF. For the calculation of the MSF we again use the Wolf's algorithm, using an Euler algorithm with integration step size $\delta t = 10^{-5}$, with an integration length equal to $L = 2500$, averaging over a time window of length $T = 0.9L$.
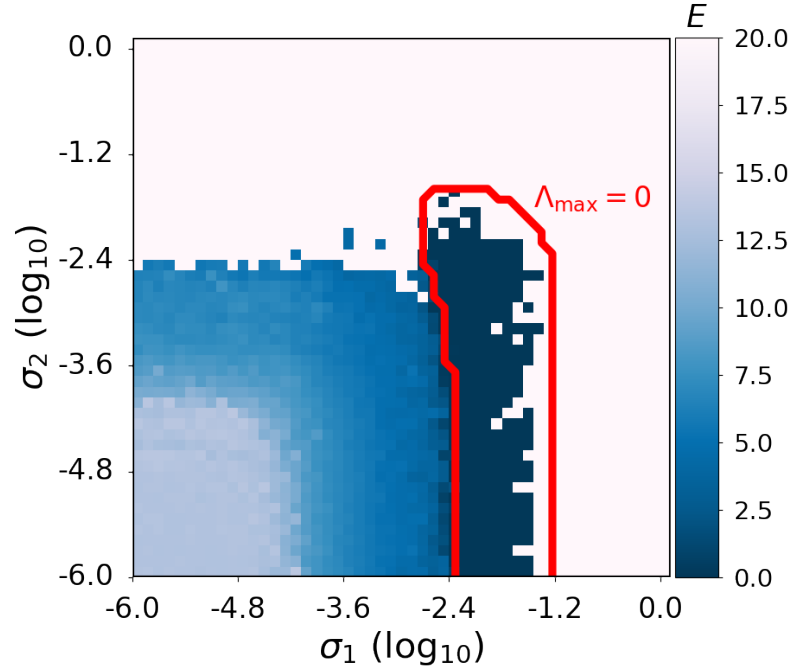
Figure 2.8: Contour plot of the average synchronization error E (Eq. (2.3)) in a system of Rössler oscillators as a function of the coupling coefficients σ_1 and σ_2. The oscillators are coupled through a simplicial complex obtained from the Zachary's karate club network where all triangles are considered as being 2-simplices. The red continuous line corresponds to the boundary of the stability region as predicted by the MSF, i.e., $\Lambda_{max} = 0$.

To begin with, we consider the case where all triangles are filled, i.e., $p_H = 1$. The results of our analysis are shown in Fig. 2.8. In general, the MSF is able to predict the values of σ_1 and σ_2 for which the synchronous state is stable. In particular, we observe that pairwise interactions play a crucial role in the onset of synchronization, as this is not achievable when only three-body interactions are active. Similarly to what we have seen in the general case (see panel C of Fig. 2.2), this is due to the structure of the simplicial complex. In fact, if we remove the links, namely we set $\sigma_1 = 0$, the simplicial complex becomes disconnected, and so synchronization is prevented. This result shows the capability of our framework of predict-

ing the synchronization behavior of a system of coupled oscillators even in real-world higher-order structures.

Finally, we use the theoretical framework we have developed to briefly discuss whether higher-order interactions promote or impede synchronization. In the case of natural coupling, the stability of the synchronous state can be analyzed in two steps. First, we derive a MSF, which is independent on the specific higher-order topology considered, as this only depends on the local dynamics on the node and on the coupling functions. Second, the MSF is evaluated at the points $\sigma_1 \lambda_i$, where λ_i is any nontrivial eigenvalue of the effective Laplacian matrix $\mathcal{L}$. Therefore, in the case of natural coupling, we can study the synchronizability of a given higher-order structures by analyzing the spectrum of its associated matrix $\mathcal{L}$, which encodes all the different orders of interaction. In particular, we can calculate two quantities to assess the synchronizability of the topology, namely λ_2 and λ_2/λ_N [26, 28]. The former quantity provides the scaling of synchronization for type II MSF. In this case $\Lambda_{\max}(\alpha) < 0$ for α larger than a threshold value $\alpha_c = \sigma_1^{\text{critical}} \lambda_2$, therefore the larger λ_2 is, the more synchronizable the topology is, as the critical value of the coupling strength for which the threshold α_c is achieved is smaller. The ratio λ_2/λ_N is instead a proxy of synchronizability for type III MSF. In this latter case, one has $\Lambda_{\max}(\alpha) < 0$ in an interval $[\alpha_1, \alpha_2]$, so synchronization is achieved only if all $\sigma_1 \lambda_i$ are within such an interval. This holds true if $\sigma_1 \lambda_2 > \alpha_1$ and $\sigma_1 \lambda_N < \alpha_2$, which yields the condition

$$\frac{\lambda_2}{\lambda_N} > \frac{\alpha_1}{\alpha_2}. \tag{2.8}$$

Hence, also in this case the larger the value λ_2/λ_N, the easier it is to synchronize the system.

To study the synchronizability of higher-order structures, here we consider the example of the Zachary's karate club network, now constructing different simplicial complexes by increasing p_H, and we analyze how the quantities λ_2 and λ_2/λ_N vary as a function of p_H. Additionally, the effective Laplacian matrix $\mathcal{L}$ is a function of $r_2 = \sigma_2/\sigma_1$, we study such a dependence for different values of the ratio between the coupling coefficients. The results obtained are shown in Fig. 2.9. We observe two opposite behaviors. On the one hand, we find that λ_2 increases as a function
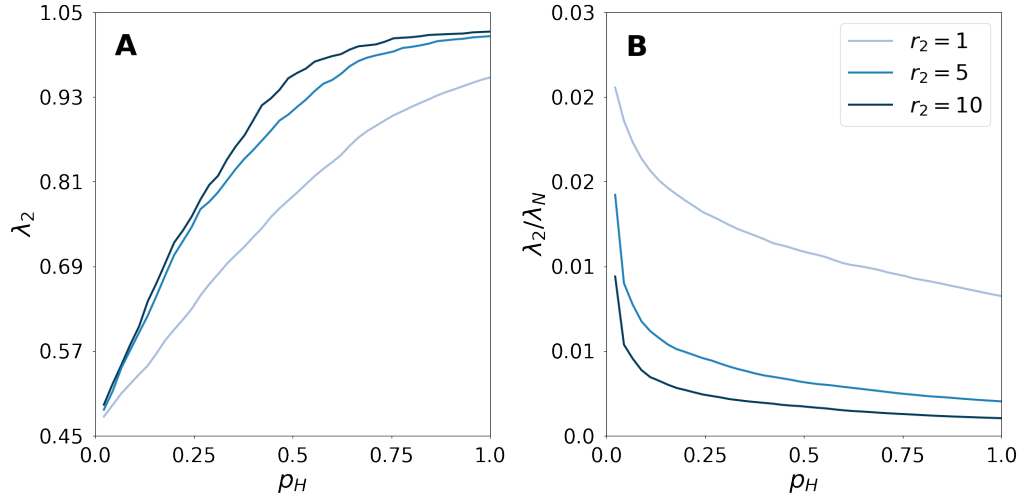
Figure 2.9: Synchronizability of the higher-order Zachary's karate club network as a function of the fraction of active 2-simplices. Panel A represent the dependence of λ_2 on p_H, while panel B that of the ratio λ_2/λ_N. The three curves represent the results obtained for the three different values of the ratio $r_2 = \sigma_2/\sigma_1$.

of p_H, meaning that higher-order interactions promote synchronization when the MSF is of type II. On the other hand, we note that an increase in the fraction of 2-simplices reduces the value of λ_2/λ_N, thus negatively affecting the synchronizability of the higher-order structure for type III MSF. Consistently, we observe that increasing the value of r_2, which is directly related to the strength of the higher-order interactions, leads to larger values of λ_2 and smaller values of λ_2/λ_N, further confirming the positive impact of three-body interactions on sychronizability in type II MSF, and the negative effect on type III MSF.

These results paves the way also for the study of synchronization of nonidentical oscillators. In such a case, the theory of MSF cannot be applied, as it is not possible to define an invariant manifold. However, it possible to show numerically that the ratio λ_2/λ_N still provides a good proxy of the propensity for synchronization of a network of nonidentical units [29]. Hence, investigating whether this result also applies to higher-order networks represents an interesting research question, which will be
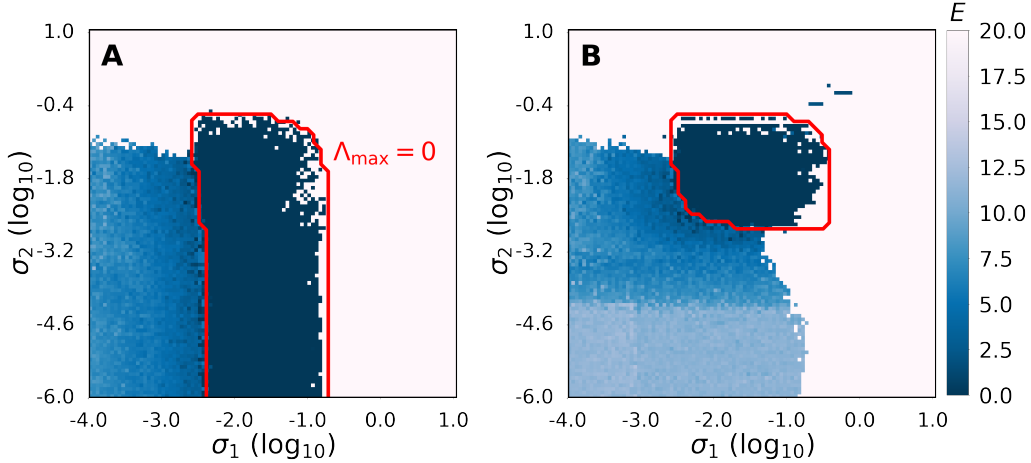
Figure 2.10: Comparison between the synchronization behaviors on a simplicial complex (panel A) and on a hypergraph (panel B). The contour plots show the average synchronization error E (Eq. (2.3)). The red continuous line corresponds to the boundary of the stability region as predicted by the MSF, i.e., $\Lambda_{\max} = 0$.

addressed in future studies.

2.3.1 A comparison between hypergraphs and simplicial complexes

So far, all the numerical examples we have discussed have been carried out on simplicial complexes. However, the mathematical framework here developed is general enough to be applicable to both simplicial complexes and hypergraphs. Yet, despite the formal similarities of the equations for synchronization in the two higher-order structures, different dynamical behaviors can be obtained for the two. Hence, we conclude this chapter by presenting some numerical analysis aiming to compare the synchronization behaviors in hypergraphs and simplicial complexes.

We consider a system of N Rössler oscillators, coupled through diffusive-like interaction functions, with $\mathbf{h}^{(1)}(\mathbf{x}_j) = [x_j^3, 0, 0]^T$ and $\mathbf{h}^{(2)}(\mathbf{x}_j, \mathbf{x}_k) =$

$[x_j^2 x_k, 0, 0]^T$, which satisfy the natural coupling hypothesis. The dynamics of the system in this configuration is governed by Eqs. (2.7). As concerns the topology of the coupling, we account for an example of simplicial complex and one of hypergraph. For the former, we take the motif displayed in panel C of Fig. 2.2. For the latter we consider the same motif where we remove the links adjacent to the 2-simplices, meaning that the triples of nodes interact only with three-body couplings. For the two structures, we integrate Eqs. (2.7) for different values of the coupling strengths σ_1 and σ_2, and we monitor the system synchronization with the average synchronization error E. To integrate the system equations, we use an Euler algorithm, with integration step fixed to $\delta t = 10^{-4}$, for a time interval of length $2T$, where $T = 500$. Then, we compare the results obtained with the theoretical predictions of the MSF, that we calculate using the Wolf's algorithm (integration step size $\delta t = 10^{-5}$, integration length $L = 2500$, averaging time window length $T = 0.9L$).

The results of the analysis are shown in Fig. 2.10. Beside the good agreement between the theoretical predictions and the numerical simulations, which confirms the applicability of our approach to hypergraphs, we observe a different synchronization behavior between the two higher-order structures. Indeed, comparing the two panels, we note that, while the simplicial complex can achieve synchronization even for small values of σ_2 (panel A), this is not the case for the hypergraph, which requires an higher value of the coupling coefficient to synchronize (panel B). Hence, given the structure of the hypergraph, both two-body and three-body interactions are needed for the onset of synchronization, the presence of pairwise interactions among the nodes involved in three-body interactions in the simplicial complex guarantees the stability of the synchronous state even for small values of σ_2.

In conclusion, the results presented in this chapter confirm the validity of the theoretical derivation of the necessary conditions for which the synchronous state is stable in undirected higher-order topologies. We have numerically investigated the role of the structure of the higher-order interactions and of the form of the coupling functions on the dynamics of the system of coupled oscillators, finding synchronization behaviors similar to those observed in complex networks. Additionally, we have explored the interplay between different orders of interaction and their

role on the system synchronizability in the special cases of commuting Laplacian matrices and of natural coupling functions. Finally, we have illustrated the differences in the synchronization behavior between simplicial complex and in hypergraphs. In the next chapter, we will extend the analysis of synchronization in higher-order structures by considering directionality in the higher-order interactions.

Synchronization in directed high-order structures

Having studied the emergence of synchronization in system of coupled chaotic oscillators with reciprocal pairwise and higher-order interactions, in this chapter we focus on the more general scenario where the coupling among the units can be nonreciprocal. In particular, here we present a few numerical analyses, all carried out using systems of Rössler oscillator interacting through natural coupling functions, showing how the presence of privileged directions in higher-order interactions can dramatically change the synchronization behavior of the system. We investigate how tuning the directionality in higher-order interactions can induce either the desynchronization of a system of synchronized units or the stabilization of an otherwise unstable synchronized state. We then compare and discuss the different ways in which the tuning of directionality can be performed. Lastly, we accompany these studies with a few results showing how directionality affects the eigenvalue distribution of randomly generated hypergraphs.

3.1 The effect of directionality on synchronization

We begin our analysis by considering a system of N coupled Rössler oscillators, the dynamics of which is governed by Eq. (2.1). Again, we set the system parameters to that its dynamics is chaotic, namely we fix $a = b = 0.2$, and $c = 9$. For the sake of clarity, we only consider two-body and three-body interactions. We couple the oscillators on the x-component, using diffusive-like functions, with $\mathbf{h}^{(1)}(\mathbf{x}_j) = [x_j^3, 0, 0]^T$ and $\mathbf{h}^{(2)}(\mathbf{x}_j, \mathbf{x}_k) = [x_j^2 x_k, 0, 0]^T$. Note that these satisfy the natural coupling hypothesis. Under these assumptions, we can write the equations governing the dynamics of each node i, which are

$$
\begin{aligned}
\dot{x}_i &= -y_i - z_i + \sigma_1 \sum_{j=1}^{N} a_{ij}^{(1)}(x_j^3 - x_i^3) + \sigma_2 \sum_{j,k=1}^{N} a_{ijk}^{(2)}(x_j^2 x_k - x_i^3), \\
\dot{y}_i &= x_i + a y_i, \\
\dot{z}_i &= b + z_i(x_i - c).
\end{aligned}
\tag{3.1}
$$

To study how directionality affects the synchronization of the system, we account for a weighted directed hypergraph. In particular, we consider a higher-order structure of which we can tune how directed are its hyperedges as a function of a single "symmetry parameter" p. We will take into consideration a hypergraph that has reciprocal two-body interactions and nonreciprocal three-body interactions, respectively, so to assess the role of directionality in higher-order interactions only. To construct such a structure, we start from an undirected ring network of N nodes, where N is even. By labeling the nodes in a consecutive order, each node i will be connected to nodes $i - 1$ and $i + 1$, namely we set $A_{i,i-1}^{(1)} = A_{i-1,i}^{(1)} = 1$ and $A_{i,i+1}^{(1)} = A_{i+1,i}^{(1)} = 1$. Then, we add a set of weighted 2-hyperedges among adjacent triple of nodes. In particular, we add $N/2$ 2-hyperedges connecting nodes $(1, 2, 3)$, $(3, 4, 5)$, ..., $(N - 1, N, 1)$. As discussed in Chapter 1, an undirected 2-hyperedge can be decomposed in three 1-directed hyperedges. Hence, for each triple of nodes $(i, i + 1, i + 2)$ where we have added an hyperedge, we set a different weight for the three directions of the interactions so to create a
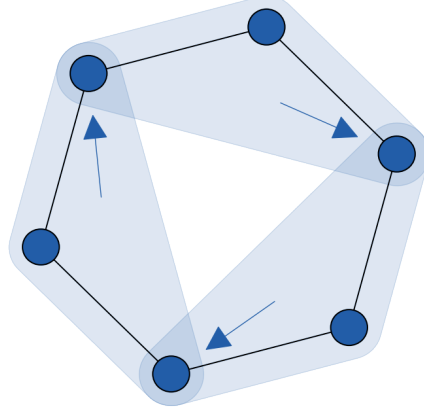
Figure 3.1: Graphical representation of the weighted hypergraph used for the numerical analyses of directionality in higher-order networks, with $N = 6$ nodes. The arrow indicates the node to which the 1-directed hyperedge points when $p = 0$.

privileged direction in the ring of nodes. In particular, we assign weight 1 to the hyperedge directed from nodes i and $i+1$ to node $i+2$, while we assign weight p, with $p \in [0, 1]$ to the hyperedge directed from nodes $i+1$ and $i+2$ to node i and to that directed from nodes i and $i+2$ to node $i+1$. Formally, this means to set $A^{(2)}_{i+2,i,i+1} = A^{(2)}_{i+2,i+1,i} = 1$, $A^{(2)}_{i,i+1,i+2} = A^{(2)}_{i,i+2,i+1} = p$, and $A^{(2)}_{i+1,i,i+2} = A^{(2)}_{i+1,i+2,i} = p$. In this way, we can tune with continuity how directed the hyperedges are. In fact, when $p = 0$, only one of the three directions of the hyperdge is active, which means that the higher-order interactions are completely nonreciprocal, as only one node is influenced by the presence of the other two and not vice-versa. As p increases, so does the weight of the other two directions. When $p = 1$, we recover an undirected structure, which represent the case of reciprocal three-body interactions, as each node in the triple is affected by the other two in the same way. A graphical representation of the hypergraph with $N = 6$ nodes is displayed in Fig. 3.1.

As an example, we now write the adjacency tensors and the Laplacian matrices that characterize the hypergraph in the case $N = 6$. We start

from the adjacency matrix $\mathbf{A}^{(1)}$, encoding the pattern of the two-body interactions. This is given by

$$\mathbf{A}^{(1)} = \begin{pmatrix} 0 & 1 & 0 & 0 & 0 & 1 \\ 1 & 0 & 1 & 0 & 0 & 0 \\ 0 & 1 & 0 & 1 & 0 & 0 \\ 0 & 0 & 1 & 0 & 1 & 0 \\ 0 & 0 & 0 & 1 & 0 & 1 \\ 1 & 0 & 0 & 0 & 1 & 0 \end{pmatrix}. \tag{3.2}$$

Let us remark that, as we are considering two-body interactions that are reciprocal, $\mathbf{A}^{(1)}$ is symmetric. From the adjacency matrix, we can evaluate the Laplacian matrix relative to the pairwise interactions, namely

$$\mathbf{L}^{(1)} = \begin{pmatrix} 2 & -1 & 0 & 0 & 0 & -1 \\ -1 & 2 & -1 & 0 & 0 & 0 \\ 0 & -1 & 2 & -1 & 0 & 0 \\ 0 & 0 & -1 & 2 & -1 & 0 \\ 0 & 0 & 0 & -1 & 2 & -1 \\ -1 & 0 & 0 & 0 & -1 & 2 \end{pmatrix}, \tag{3.3}$$

which is symmetric as well. As regards the three-body interactions, these are encoded by the adjacency tensor $\mathbf{A}^{(2)}(p)$, which is a function of the symmetry parameter p. This reads

$$\mathbf{A}^{(2)}(p) = (\{A_{1jk}^{(2)}(p)\}, \dots, \{A_{6jk}^{(2)}(p)\}) =$$

$$\left(\begin{pmatrix} 0 & 0 & 0 & 0 & 0 & 0 \\ 0 & 0 & p & 0 & 0 & 0 \\ 0 & p & 0 & 0 & 0 & 0 \\ 0 & 0 & 0 & 0 & 0 & 0 \\ 0 & 0 & 0 & 0 & 0 & 1 \\ 0 & 0 & 0 & 0 & 1 & 0 \end{pmatrix}, \begin{pmatrix} 0 & 0 & p & 0 & 0 & 0 \\ 0 & 0 & 0 & 0 & 0 & 0 \\ p & 0 & 0 & 0 & 0 & 0 \\ 0 & 0 & 0 & 0 & 0 & 0 \\ 0 & 0 & 0 & 0 & 0 & 0 \\ 0 & 0 & 0 & 0 & 0 & 0 \end{pmatrix}, \begin{pmatrix} 0 & 1 & 0 & 0 & 0 & 0 \\ 1 & 0 & 0 & 0 & 0 & 0 \\ 0 & 0 & 0 & 0 & 0 & 0 \\ 0 & 0 & 0 & 0 & p & 0 \\ 0 & 0 & 0 & p & 0 & 0 \\ 0 & 0 & 0 & 0 & 0 & 0 \end{pmatrix}, \right.$$

$$\left. \begin{pmatrix} 0 & 0 & 0 & 0 & 0 & 0 \\ 0 & 0 & 0 & 0 & 0 & 0 \\ 0 & 0 & 0 & 0 & p & 0 \\ 0 & 0 & 0 & 0 & 0 & 0 \\ 0 & 0 & p & 0 & 0 & 0 \\ 0 & 0 & 0 & 0 & 0 & 0 \end{pmatrix}, \begin{pmatrix} 0 & 0 & 0 & 0 & 0 & p \\ 0 & 0 & 0 & 0 & 0 & 0 \\ 0 & 0 & 0 & 1 & 0 & 0 \\ 0 & 0 & 1 & 0 & 0 & 0 \\ 0 & 0 & 0 & 0 & 0 & 0 \\ p & 0 & 0 & 0 & 0 & 0 \end{pmatrix}, \begin{pmatrix} 0 & 0 & 0 & 0 & p & 0 \\ 0 & 0 & 0 & 0 & 0 & 0 \\ 0 & 0 & 0 & 0 & 0 & 0 \\ 0 & 0 & 0 & 0 & 0 & 0 \\ p & 0 & 0 & 0 & 0 & 0 \\ 0 & 0 & 0 & 0 & 0 & 0 \end{pmatrix} \right), \tag{3.4}$$

where $\{A_{1jk}^{(2)}(p)\}, \dots, \{A_{6jk}^{(2)}(p)\}$ are the matrices from fixing the first index of the tensor. We observe that, since we are considering nonreciprocal

three-body interactions, the adjacency tensor $\mathbf{A}^{(2)}(p)$ is in general not symmetric to a generic permutation of its indexes, e.g., $A_{123}(p) \neq A_{312}(p)$ for $p \neq 1$. However, when $p = 1$, namely when all interactions among the nodes have the same strength, the tensor becomes symmetric, meaning that $A_{ijk}^{(2)}(p = 1) = 1 \Rightarrow A_{\pi(ijk)}^{(2)}(p = 1) = 1$, with π a generic permutation of indexes. Also, let us remark that the matrices resulting from fixing the first index of the tensor are symmetric for any value of p. Given $\mathbf{A}^{(2)}(p)$, we can calculate the Laplacian matrix for the three-body interactions (see Eq. (1.6)). This is given by

$$\mathbf{L}^{(2)}(p) = \begin{pmatrix} 2(1+p) & -p & -p & 0 & -1 & -1 \\ -p & 2p & -p & 0 & 0 & 0 \\ -1 & -1 & 2(1+p) & -p & -p & 0 \\ 0 & 0 & -p & 2p & -p & 0 \\ -p & 0 & -1 & -1 & 2(1+p) & -p \\ -p & 0 & 0 & 0 & -p & 2p \end{pmatrix}. \tag{3.5}$$

Consistently, since the adjacency tensor $\mathbf{A}^{(2)}(p)$ is not symmetric, $\mathbf{L}^{(2)}(p)$ is not symmetric as well. Yet, when $p = 1$, we retrieve as expected a symmetric Laplacian matrix.

Let us here point out a that the way in which we tune the hypergraph from directed to undirected does not conserve the total strength of the interactions. To explain this, let us consider the case of three nodes i, j, and k interacting through nonreciprocal interactions. We assume the three possible 1-directed hyperedges among the nodes to have different weight, in particular we take $A_{i,j,k}^{(2)} = A_{i,k,j}^{(2)} = 1$, $A_{j,k,i}^{(2)} = A_{j,i,k}^{(2)} = p$, and $A_{k,i,j}^{(2)} = A_{k,j,i}^{(2)} = p$. Hence, the strength of the hyperedge resulting from the composition of three 1-directed hyperedges increases as a function of p. When $p = 0$ only one direction is active, i.e., from j and k to i, so the total strength of the interaction among the nodes, which remains nonreciprocal, is 1. The total strength increases as we increase p, until we reach $p = 1$, where all directions has the same strength, so the total strength of the reciprocal interaction is three times the strength of the nonreciprocal interactions. A graphical representation of the symmetrization is shown in Fig. 3.2. Such a symmetrization method is motivated by the fact that, in real-world systems, a change in the strength of an interaction
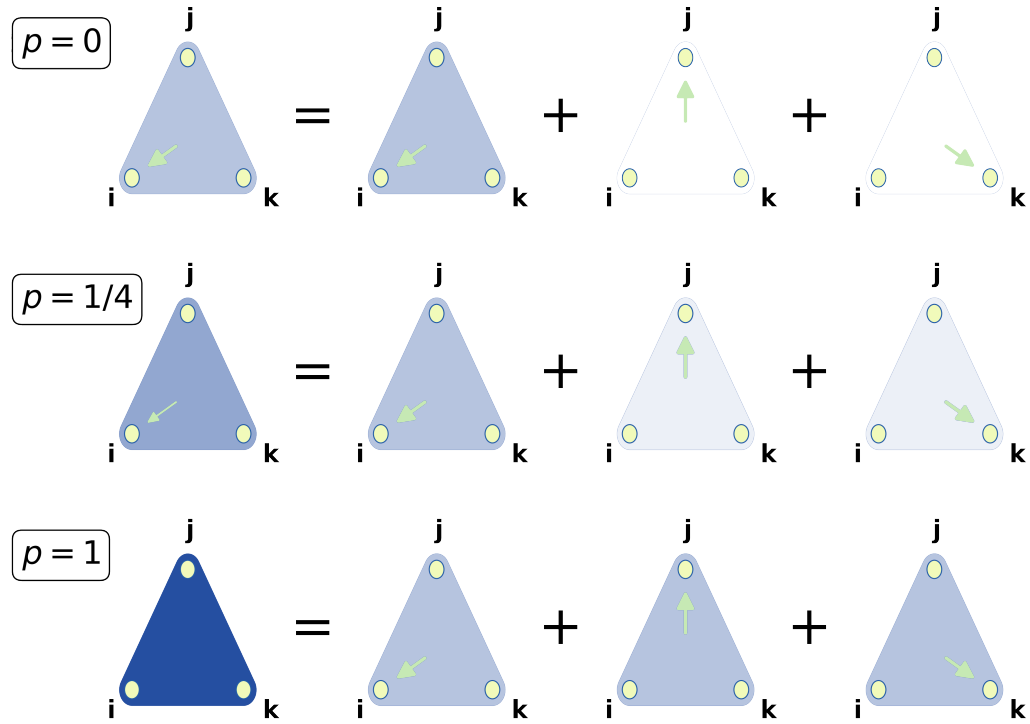
Figure 3.2: Graphical representation of the symmetrization of a 1-directed 2-hyperedge, as a function of the symmetry parameter p. Starting from a single 1-directed hyperedge ($p = 0$), the strength of the other directions is varied until all directions of interaction have the same weight ($p = 1$). Note that the strength of the total interaction, which transits from nonreciprocal to reciprocal, increases as a function of p.

does not necessarily imply a variation in the reciprocal interactions that keeps constant the total interaction strength. However, a change in the strength of the composed hyperedge utterly impacts the synchronization behavior of the system. For this reason, in the next section we will study an alternative symmetrization that conserves the total coupling strength of the interaction.

Our analysis begins with calculating the MSF associated to system (3.1), which means to linearize the equations governing the system dynamics, and to evaluate the maximum Lyapunov exponent corresponding to the
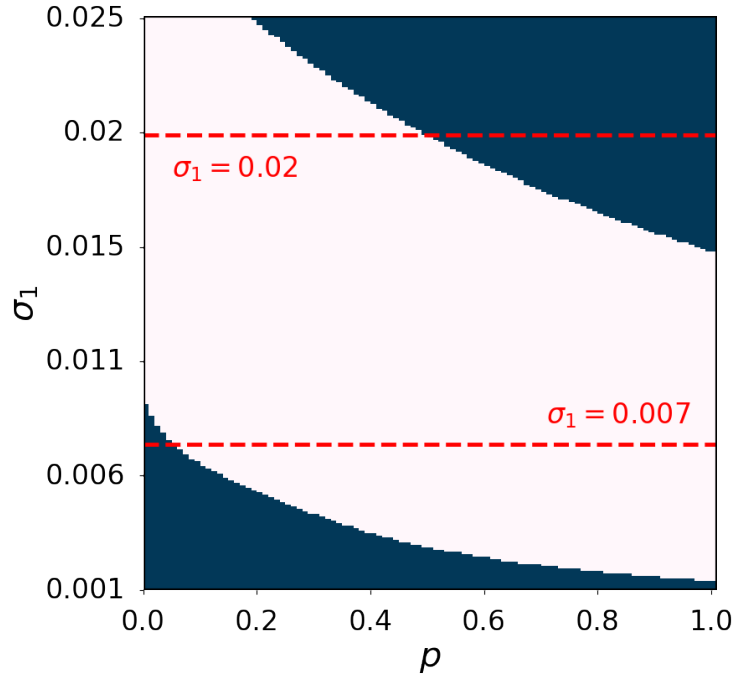
Figure 3.3: Synchronization diagram in the plane (p, σ_1) for system (3.1). The white area indicates the region of stability, while the blue one the region where the synchronous state is unstable. The horizontal dashed red lines evidence two generic values of σ_1 for which the system transits from a synchronized to an unsynchronized state as we increase p ($\sigma_1 = 0.02$), and the other way around ($\sigma_1 = 0.007$).

motion transverse to the synchronization manifold. As previously discussed, the property of stability in the case of coupling functions respecting the natural coupling hypothesis will depend on the eigenvalues of an effective Laplacian matrix $\mathcal{L}$ encoding the contribution of the different orders of interaction. Compared to the case of undirected higher-order structures, however, as $\mathcal{L}$ is not symmetric, its spectrum will be in general complex. Hence, the MSF will be a function of a complex parameter, i.e., $\Lambda_{\max}(\alpha + i\beta)$. For synchronization to be achieved, a necessary condition is that $\Lambda_{\max}(\alpha + i\beta) < 0$, where $\alpha + i\beta$ is any non-zero eigenvalue of $\mathcal{L}$ times the coupling coefficient σ_1. Conversely, if there is at least an eigenvalue of $\mathcal{L}$ such that $\Lambda_{\max} > 0$, then the synchronous state is unstable. To

calculate the MSF we exploit again the Wolf's algorithm, using an Euler algorithm with integration step size $\delta t = 10^{-5}$, with simulation length equal to $L = 2500$, averaging over a time window of length $T = 0.9L$.

To illustrate the effect of directionality on synchronization, we consider a directed weighted hypergraph of $N = 20$ nodes, built with the algorithm described above. We calculate the eigenvalues of the associated effective Laplacian matrix $\mathcal{L}$ as a function of the symmetry parameter p. To study the interplay between directionality and strength of the interactions, we also vary the coupling strength σ_1, having fixed the ratio $r_2 = \sigma_2/\sigma_1 = 10$. We remark that the eigenvalues of $\mathcal{L}$ depends on the structure of interactions, encoded by the Laplacian matrices $\mathbf{L}^{(1)}$ and $\mathbf{L}^{(2)}(p)$, and on the ratio r_2. Hence, since the latter is fixed, the spectrum of $\mathcal{L}$ only depends on the symmetry parameter p. In this way, we obtain a synchronization diagram in the plane (p, σ_1), which is shown in Fig. 3.3. The white area represents the values (p, σ_1) for which the system synchronizes, namely the sets for which $\Lambda_{\max} < 0$ for every eigenvalue of $\mathcal{L}$. On the contrary, the blue area shows the region of instability, i.e., $\Lambda_{\max} > 0$ for at least one eigenvalue of $\mathcal{L}$. We find different behaviors of the system as a function of the coupling strength σ_1. First, we see that for very small values of σ_1, the system does not synchronize for any value of the symmetry parameter p, meaning that the coupling is too weak to win the divergence of the perturbations around the synchronous state. Conversely, we also note an interval of values of σ_1 for which the system remains synchronized no matter the value of p. Finally, we observe that there are two other regions where a variation in the value of the symmetry parameter leads to a transition in the system either from synchronized to unsynchronized or the other way around. An example of these two behaviors is hallmarked in the figure by the two horizontal dashed red lines. On the one hand, for $\sigma_1 = 0.02$, we see that the synchronous state is stable for small values of p, namely when the hyperedges are strongly directed, while it loses stability for larger values of p, i.e., when the hypergraph is more symmetric. On the other hand, for $\sigma_1 = 0.007$ we observe the opposite behavior, with synchronization that is achieved by increasing p, while a strongly directed hypergraph prevents the synchronization of the chaotic oscillators.

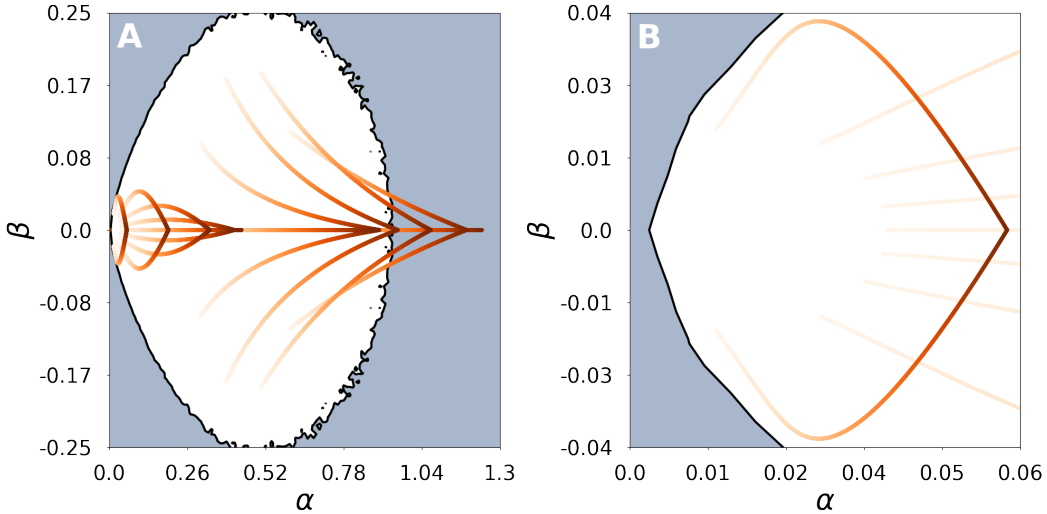The system of coupled oscillators is synchronized when all points

Figure 3.4: Desynchronization induced by symmetrization. In the background, the white area represents the stability region of the synchronous state, identified by a negative MSF, the black line its boundary, while the light blue area the region where the synchronization manifold is unstable, namely the area of the complex plane for which the MSF is positive. The colored lines display the locus of the eigenvalues of $\widetilde{\mathcal{L}}$ as a function of p, for a weighted hypergraph with $N = 20$ nodes, pairwise coupling coefficients fixed to $\sigma_1 = 0.02$, and $\sigma_2 = 10\sigma_1$. The color coding is such that the case $p = 0$ is represented in light red, while the case $p = 1$ in dark red. Panel B shows a zoom of the area close to the origin.

$\sigma_1 \lambda(\mathcal{L})$ are inside the region of the complex plane (α, β) for which $\Lambda_{\max}$ is negative, while it not synchronized when one or more points are outside the same region. Hence, the transition of the system from a synchronized to a desynchronized state as a function of p occurs when at least one of the eigenvalues of $\widetilde{\mathcal{L}} = \sigma_1 \mathcal{L}$, which depends on p, leaves the region of stability. On the other way around, the transition from desynchronization to a synchronization is achieved when all the eigenvalues of $\widetilde{\mathcal{L}}$ enter the stability region. To show this, we consider the locus of the eigenvalues of $\widetilde{\mathcal{L}}$ as a function of p, accounting for two values of σ_1 highlighted in Fig. 3.3, corresponding to the two possible transitions that can be induced by directionality. Figs. 3.4 and 3.5 show the transition from synchroniza-
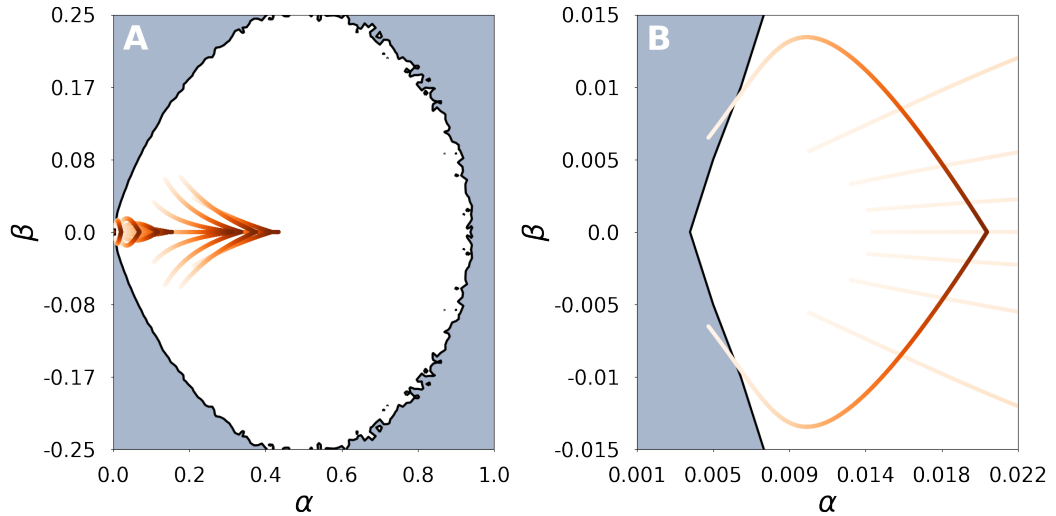
Figure 3.5: Desynchronization induced by directionality. In the background, the white area represents the stability region of the synchronous state, identified by a negative MSF, the black line its boundary, while the light blue area the region where the synchronization manifold is unstable, namely the area of the complex plane for which the MSF is positive. The colored lines display the locus of the eigenvalues of $\widetilde{\mathcal{L}}$ as a function of p, for a weighted hypergraph with $N = 20$ nodes, pairwise coupling coefficients fixed to $\sigma_1 = 0.007$, and $\sigma_2 = 10\sigma_1$. The color coding is such that the case $p = 0$ is represented in light red, while the case $p = 1$ in dark red. Panel B shows a zoom of the area close to the origin.

tion to desynchronization as a function of p, and the other way around, respectively. In both figures, the light blue area in the background represents the region where the MSF is positive, hence the area where the synchronous state is unstable, while the white area portrays the region of stability. The boundary value $\Lambda_{\max}(\alpha + i\beta) = 0$ is instead shown as a continuous black line between the two regions. We observe that the region of the complex plane (α, β) for which $\Lambda_{\max} < 0$ is bounded, both along the real axis and the imaginary one. This shape of the stability region, which is the complex-value equivalent of a type III MSF [48, 26], implies that either a large value of α or a large value of β can induce the system instability. The colored lines show the locus of the eigenvalues of

$\widetilde{\mathcal{L}}$ as a function of p, so that the case $p = 0$ is represented in light red, while the case $p = 1$ in dark red. Note also that in both figures panel B represents a zoom of the area close to the origin. In Fig. 3.4, which refers to the case where the coupling coefficient is fixed to $\sigma_1 = 0.02$, we note that for large enough p the eigenvalues cross the boundary and leave the stability region, thus inducing the desynchronization of the system. Conversely, in Fig. 3.5, displaying the case $\sigma_1 = 0.07$, we observe that the eigenvalues of $\widetilde{\mathcal{L}}$ enter the stability region for large values of p, meaning that more reciprocal higher-order interactions favors the synchronization of the system of oscillators.

As clear from these results, directionality can change the dynamical behavior of a system of coupled chaotic oscillators, either inducing the synchronization of the system or its desynchronization. However, as we have seen in the case of undirected higher-order structures, a different choice of the coupling functions leads to a different synchronization behavior. Hence, to conclude this section, we consider as a further example the case of a system of Rössler oscillators coupled on the y-component. In particular, we account again for diffusive-like functions, with $\mathbf{h}^{(1)}(\mathbf{x}_j) = [0, y_j^3, 0]^T$ and $\mathbf{h}^{(2)}(\mathbf{x}_j, \mathbf{x}_k) = [0, y_j^2 y_k, 0]^T$, which satisfy the natural coupling hypothesis. The equations governing the dynamics of the system are

$$\dot{x}_i = -y_i - z_i,$$

$$\dot{y}_i = x_i + ay_i + \sigma_1 \sum_{j=1}^{N} a_{ij}^{(1)}(y_j^3 - y_i^3) + \sigma_2 \sum_{j,k=1}^{N} a_{ijk}^{(2)}(y_j^2 y_k - y_i^3), \qquad (3.6)$$

$$\dot{z}_i = b + z_i(x_i - c).$$

As we have done for the previous example, we first calculate the MSF associated to system (3.6). To do so, we account again for the Wolf's algorithm, using an Euler algorithm with integration step size $\delta t = 10^{-5}$, with simulation length equal to $L = 2500$, averaging over a time window of length $T = 0.9L$. We study the effect of directionality on the synchronization behavior of a system of $N = 20$ oscillators whose structure of interactions is given by the directed weighted hypergraph described above. In particular, we calculate the eigenvalues of the effective Laplacian matrix $\widetilde{\mathcal{L}}$, and study how they vary as a function of the symmetry
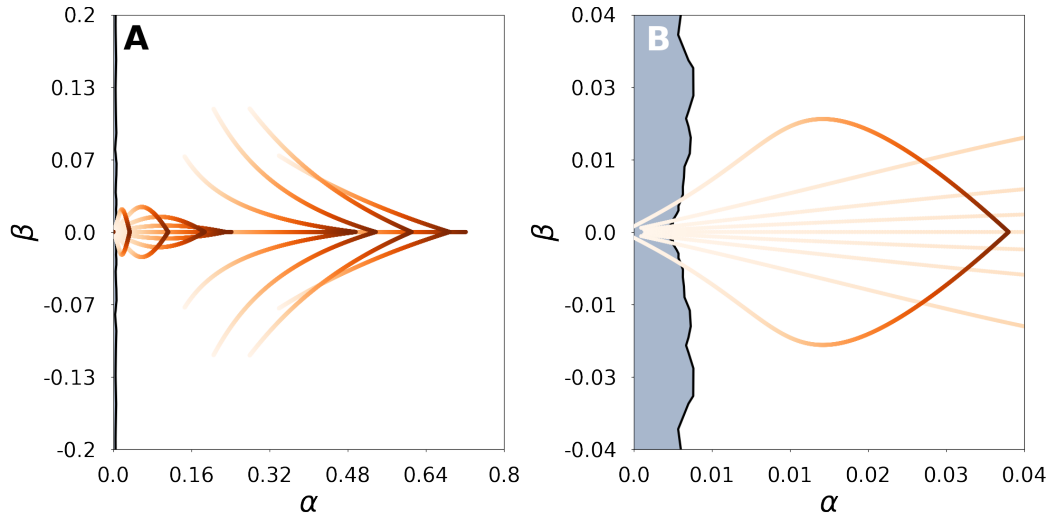
Figure 3.6: Desynchronization induced by directionality for a system of Rössler oscillators coupled on the y component. In the background, the white area represents the stability region of the synchronous state, identified by a negative MSF, the black line its boundary, while the light blue area the region where the synchronization manifold is unstable, namely the area of the complex plane for which the MSF is positive. The colored lines display the locus of the eigenvalues of $\widetilde{\mathcal{L}}$ as a function of p, for a weighted hypergraph with $N = 20$ nodes, pairwise coupling coefficients fixed to $\sigma_1 = 0.001$ and $\sigma_2 = 0.12$. The color coding is such that the case $p = 0$ is represented in light red, while the case $p = 1$ in dark red. Panel B shows a zoom of the area close to the origin.

parameter p. We do so for two sets of the coupling coefficient σ_1, σ_2, namely $\sigma_1 = 0.001$ and $\sigma_2 = 0.12$, and $\sigma_1 = 0.01$ and $\sigma_2 = 0.16$. The locus of the eigenvalues in these two case studies is shown in Figs. 3.6 and 3.6 respectively. Once again, in both figures the light blue area in the background indicates the region where the synchronous state is unstable, while the white area portrays the region of stability, with the boundary between the two represented as a continuous black line. Similarly, the colored lines show the locus of the eigenvalues of $\widetilde{\mathcal{L}}$ as a function of p, so that the case $p = 0$ is represented in light red, while the case $p = 1$ in dark red. Again, in both figures panel B represents a zoom of the area
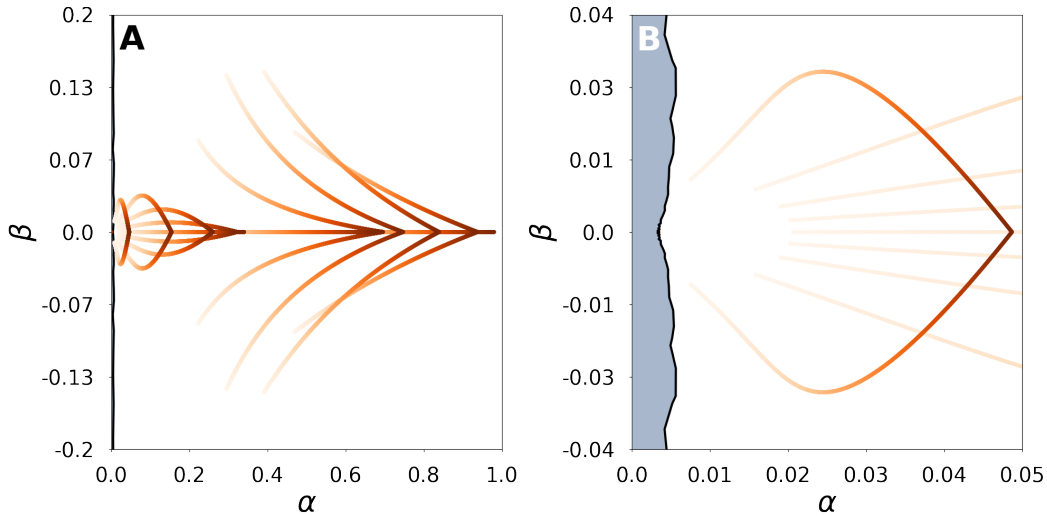
Figure 3.7: The shape of the MSF for a system of Rössler oscillators coupled on the y component does not permit the loss of synchronization by making the higher-order interactions symmetric. In the background, the white area represents the stability region of the synchronous state, identified by a negative MSF, the black line its boundary, while the light blue area the region where the synchronization manifold is unstable, namely the area of the complex plane for which the MSF is positive. The colored lines display the locus of the eigenvalues of $\widetilde{\mathcal{L}}$ as a function of p, for a weighted hypergraph with $N = 20$ nodes, pairwise coupling coefficients fixed to $\sigma_1 = 0.01$, and $\sigma_2 = 0.16$. The color coding is such that the case $p = 0$ is represented in light red, while the case $p = 1$ in dark red. Panel B shows a zoom of the area close to the origin.

close to the origin. Compared to the case where the Rössler oscillators are coupled on the x component, we observe that the region of stability is unbounded, both along the real axis and the imaginary one, being that the complex-value equivalent of a type II MSF. The shape of the MSF in this configuration ultimately determines the synchronization behavior of the system in relation to its degree of symmetry, so that it is possible to desynchronize the system by enhancing the directionality of the higher-order structure but it is not possible to do so by making the interactions among triples of nodes more symmetric. In Fig. 3.6, we observe that the

eigenvalues of $\widetilde{\mathcal{L}}$, some of which are in the region where $\Lambda_{max} > 0$, enter the stability region for large enough values of p. Hence, in this scenario it is the presence of privileged directions in the higher-order interactions to induce the desynchronization of the system. However, in Fig. 3.7, we note that if we set the coupling coefficient in such a way that the synchronous state that is stable for $p = 0$, we are not able to make the synchronization manifold unstable by varying the value of p. In facts, given the shape of the MSF, the eigenvalues of $\widetilde{\mathcal{L}}$ remain in the area of the complex plane for which $\Lambda_{max} < 0$, meaning that it is not possible to desynchronize the system by making the higher-order interactions more reciprocal.

3.2 A symmetrization preserving the total coupling strength

In the previous section, we have shown how directionality in higher-order interactions can induce either the synchronization of a system of coupled chaotic oscillators or its desynchronization. To do so, we have accounted for a method to control the degree of symmetry in the higher-order structure, which allowed us to study the impact of directionality on the synchronization behavior. However, as we have remarked, the way in which we have tuned the directionality in higher-order structures did not conserve the total strength of the interactions. This may represent a confounding factor, as the change in the stability of the synchronous state may be due to a modification in the coupling strength itself, and not to directionality. Consequently, to determine whether the variations in the synchronization behavior of the system are actually due to directionality, here we analyze a new symmetrization method that conserves the total coupling strength of the higher-order interactions.

Starting from a configuration where only one direction in the hyperedge has a nonzero weight, the previous symmetrization method consisted in gradually increasing the weight of the remaining directions until all of them had the same weight. To keep the total coupling strength constant, in this new symmetrization method we increase the strength of the others directions, while properly decreasing the strength of the first direction considered, until they have all the same strength. Let us again con-
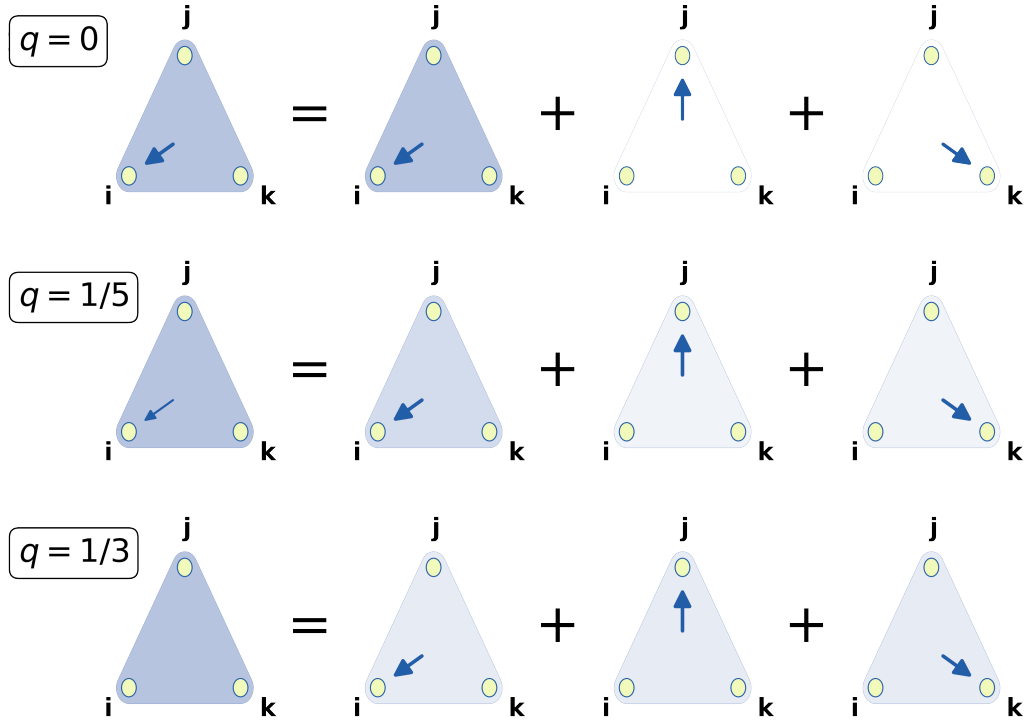
Figure 3.8: Graphical representation of the alternative symmetrization of a 1-directed 2-hyperedge, as a function of the symmetry parameter q. Starting from a single 1-directed hyperedge ($q = 0$), the strength of the other directions is varied until all directions of interaction have the same weight ($q = 1/3$). Note that the strength of the total interaction, which transits from nonreciprocal to reciprocal, is constant.

sider the case of three nodes i, j, and k interacting through nonreciprocal interactions. We assume the three possible 1-directed hyperedges among the nodes be characterized by the symmetry parameter $q \in [0, 1/3]$, so that $A_{i,j,k}^{(2)} = A_{i,k,j}^{(2)} = 1 - 2q$, $A_{j,k,i}^{(2)} = A_{j,i,k}^{(2)} = q$, and $A_{k,i,j}^{(2)} = A_{k,j,i}^{(2)} = q$. In this case, when $q = 0$ only one direction is active, namely the one from j and k to i, while we have that all directions have the same weight for $q = 1/3$. As for the first symmetrization method, this second procedure allows us to tune the directionality of the hyperedges, ranging from

a case where only one privileged direction in the interaction is present, to the case where the interactions are reciprocal. However, compared to the method described in the previous section, using this alternative symmetrization the total coupling strength of the three-body interaction does not change as we vary the symmetry parameter q. A graphical representation of symmetrization method is shown in Fig. 3.8.

We again consider the weighted directed hypergraph described in the previous section, where this time we tune the directionality of the higher-order structure using the alternative symmetrization method. Starting from an undirected ring network of N nodes, where N is even, where we label the nodes in a consecutive order, we add a set of weighted 2-hyperedges among connecting nodes $(1, 2, 3)$, $(3, 4, 5)$, ..., $(N - 1, N, 1)$, setting $A^{(2)}_{i+2,i,i+1} = A^{(2)}_{i+2,i+1,i} = 1 - 2q$, $A^{(2)}_{i,i+1,i+2} = A^{(2)}_{i,i+2,i+1} = q$, and $A^{(2)}_{i+1,i,i+2} = A^{(2)}_{i+1,i+2,i} = q$. As an example, let us here write the adjacency tensors and the Laplacian matrices characterizing the hypergraph in the case $N = 6$. As for the first symmetrization method, the adjacency matrix $\mathbf{A}^{(1)}$ and its associated Laplacian matrix $\mathbf{L}^{(1)}$, which encode the two-body interactions, are given by Eqs. (3.2) and (3.3) respectively. As concerns the adjacency tensor $\mathbf{A}^{(2)}(q)$, encoding the structure of the three-body

interactions, we have

$$A^{(2)}(q) = (\{A^{(2)}_{1jk}(q)\}, \ldots, \{A^{(2)}_{6jk}(q)\}) =$$

$$
\left(
\begin{pmatrix}
0 & 0 & 0 & 0 & 0 & 0 \\
0 & 0 & q & 0 & 0 & 0 \\
0 & q & 0 & 0 & 0 & 0 \\
0 & 0 & 0 & 0 & 0 & 0 \\
0 & 0 & 0 & 0 & 0 & 1-2q \\
0 & 0 & 0 & 0 & 1-2q & 0
\end{pmatrix},
\begin{pmatrix}
0 & 0 & q & 0 & 0 & 0 \\
0 & 0 & 0 & 0 & 0 & 0 \\
q & 0 & 0 & 0 & 0 & 0 \\
0 & 0 & 0 & 0 & 0 & 0 \\
0 & 0 & 0 & 0 & 0 & 0 \\
0 & 0 & 0 & 0 & 0 & 0
\end{pmatrix},
\right.
$$

$$
\begin{pmatrix}
0 & 1-2q & 0 & 0 & 0 & 0 \\
1-2q & 0 & 0 & 0 & 0 & 0 \\
0 & 0 & 0 & 0 & 0 & 0 \\
0 & 0 & 0 & 0 & q & 0 \\
0 & 0 & 0 & q & 0 & 0 \\
0 & 0 & 0 & 0 & 0 & 0
\end{pmatrix},
\begin{pmatrix}
0 & 0 & 0 & 0 & 0 & 0 \\
0 & 0 & 0 & 0 & 0 & 0 \\
0 & 0 & 0 & 0 & q & 0 \\
0 & 0 & 0 & 0 & 0 & 0 \\
0 & 0 & q & 0 & 0 & 0 \\
0 & 0 & 0 & 0 & 0 & 0
\end{pmatrix},
$$

$$
\begin{pmatrix}
0 & 0 & 0 & 0 & 0 & q \\
0 & 0 & 0 & 0 & 0 & 0 \\
0 & 0 & 0 & 1-2q & 0 & 0 \\
0 & 0 & 1-2q & 0 & 0 & 0 \\
0 & 0 & 0 & 0 & 0 & 0 \\
q & 0 & 0 & 0 & 0 & 0
\end{pmatrix},
\left.
\begin{pmatrix}
0 & 0 & 0 & 0 & q & 0 \\
0 & 0 & 0 & 0 & 0 & 0 \\
0 & 0 & 0 & 0 & 0 & 0 \\
0 & 0 & 0 & 0 & 0 & 0 \\
q & 0 & 0 & 0 & 0 & 0 \\
0 & 0 & 0 & 0 & 0 & 0
\end{pmatrix}
\right)
\tag{3.7}
$$

where $\{A^{(2)}_{1jk}(q)\}, \ldots, \{A^{(2)}_{6jk}(q)\}$ are the matrices obtained by fixing the first index of the tensor. As expected, the adjacency tensor $\mathbf{A}^{(2)}(q)$ is in general not symmetric to a generic permutation of its indexes, e.g., $A_{123}(q) \neq A_{312}(q)$ for $q \neq 1/3$, while we recover a symmetric tensor for $q = 1/3$, i.e., $A^{(2)}_{ijk}(1/3) = 1 \Rightarrow A^{(2)}_{\pi(ijk)}(1/3) = 1$, with π a generic permutation of indexes. We remark that the matrices resulting from fixing the first index of the tensor are instead symmetric for any value of q. We can then calculate the Laplacian matrix for the three-body interactions (see Eq. (1.6)), which is given by

$$L^{(2)}(q) =$$

$$
\begin{pmatrix}
2(1-q) & -q & -q & 0 & -(1-2q) & -(1-2q) \\
-q & 2q & -q & 0 & 0 & 0 \\
-(1-2q) & -(1-2q) & 2(1-q) & -q & -q & 0 \\
0 & 0 & -q & 2q & -q & 0 \\
-q & 0 & -(1-2q) & -(1-2q) & 2(1-q) & -q \\
-q & 0 & 0 & 0 & -q & 2q
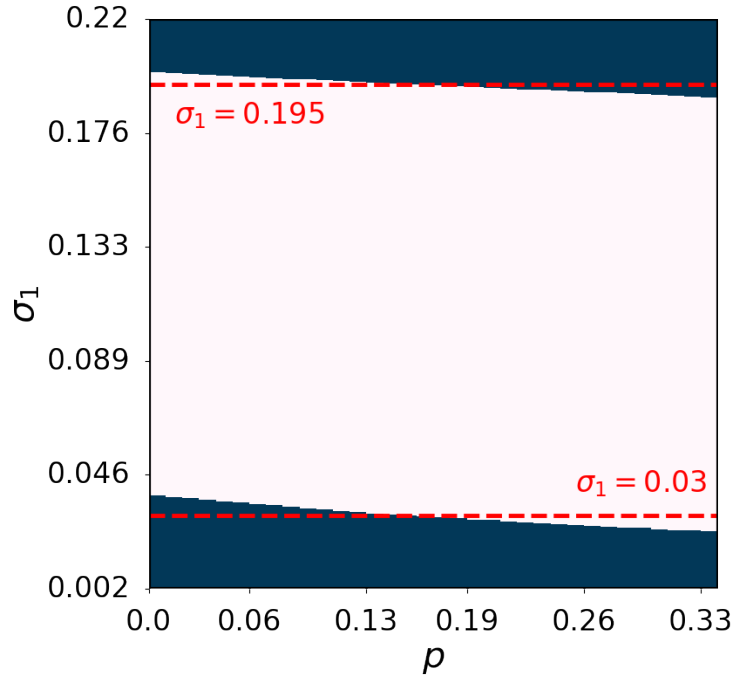\end{pmatrix}.
\tag{3.8}
$$

Figure 3.9: Synchronization diagram in the plane (q, σ_1) for system (3.1). The white area indicates the region of stability, while the blue one the region where the synchronous state is unstable. The horizontal dashed red lines evidence two particular values of σ_1 for which the system transits from a synchronized to an unsynchronized state as we increase q ($\sigma_1 = 0.195$), and the other way around ($\sigma_1 = 0.03$).

As the adjacency tensor $\mathbf{A}^{(2)}(q)$ is not symmetric in general, $\mathbf{L}^{(2)}(q)$ is not symmetric as well. When $q = 1/3$, however, we the Laplacian matrix becomes symmetric, as expected.

We again analyze the system of Rössler oscillators coupled on the x component whose dynamics is described in Eq. (3.1), where this time the terms $a_{ijk}^{(2)}$ are the elements of the adjacency tensor $\mathbf{A}^{(2)}(q)$ whose expression is given in Eq. (3.7). As it is independent on the particular topology considered, we use the MSF that we have calculated in the previous section for the first symmetrization method. To assess the impact of directionality on synchronization, we consider again a directed weighted hypergraph of $N = 20$ nodes, and we evaluate the eigenvalues of its as-

sociated effective Laplacian matrix $\mathcal{L}$ as a function of the new symmetry parameter q. Moreover, we also vary the coupling strength σ_1, fixing the ratio $r_2 = \sigma_2/\sigma_1 = 0.7$. In this way, we construct a synchronization diagram in the plane (q, σ_1), which we report in Fig. 3.9. As for the first symmetrization method, we find four different behaviors as a function of the coupling strength σ_1. First, we see that either for very small and very large values of σ_1, the system does not synchronize for any value of q. This means that there is an interval of values of σ_1 for which the coupling is too weak to dump out the perturbations transverse to the synchronization manifold, and an interval of values for which the coupling is rather too strong to allow the synchronization of the system. Then, we note an interval of values of σ_1 for which the system is synchronized no matter the degree of symmetry of the higher-order structure. Lastly, we observe two regions where a variation in the value of q leads to a transition in the state of the system either from synchronized to unsynchronized or the other way around. The presence of these two regions confirms that directionality can change the synchronization behavior of the system by itself, as the possible confounding factors have been here overcome. The horizontal dashed red lines in the figure highlight an example of the two possible transitions. First, for $\sigma_1 = 0.195$, we see that the synchronization manifold is stable for small values of q, so when the hypergraph is more directed, while stability is lost for larger values of q, so for a more symmetric hypergraph. On the other hand, for $\sigma_1 = 0.03$ the opposite behavior is observed, with the system synchronization that is achieved for larger values of q, while the presence of a strong directionality in the higher-order structure induces the loss of synchronization.

For these two values of σ_1, we study the locus of the eigenvalues of $\widetilde{\mathcal{L}}$ as a function of q. They are reported in Figs. 3.10 and 3.11, which refer to the cases $\sigma_1 = 0.195$ and $\sigma_1 = 0.03$, respectively. In both figures, the light blue area displays the region where the synchronous state is unstable, determined by a positive value of the MSF $\Lambda_{\max}$, the white area the region of stability, namely where the MSF is negative, while the continuous black line the boundary between the two, i.e., $\Lambda_{\max} = 0$. The colored lines show the locus of the eigenvalues of $\widetilde{\mathcal{L}}$ as a function of q, so that the case $q = 0$ is displayed in light red, while the case $q = 1/3$ is in dark red. Panel B of both figures shows a zoom of the area
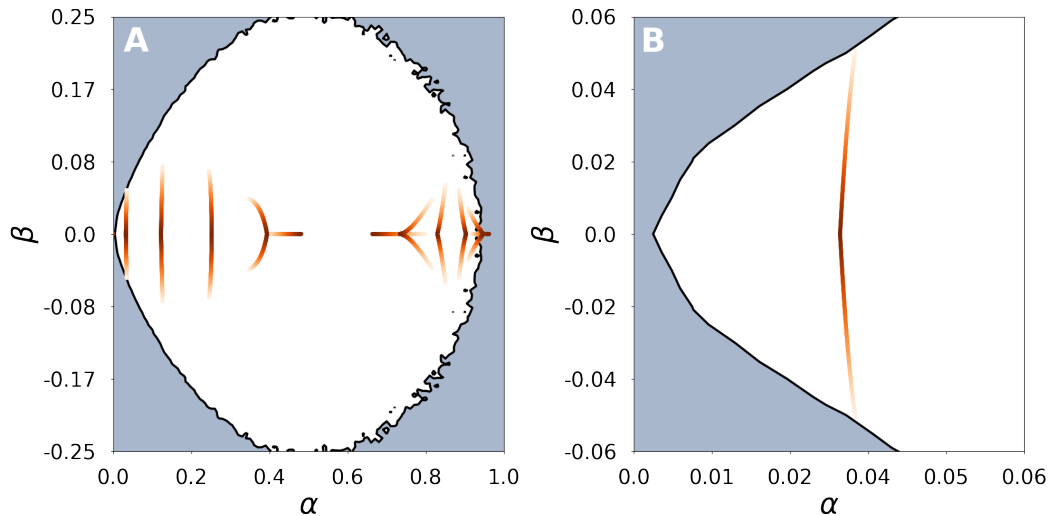
Figure 3.10: Desynchronization induced by an alternative symmetriza-tion. In the background, the white area represents the stability region of the synchronous state, identified by a negative MSF, the black line its boundary, while the light blue area the region where the synchronization manifold is unstable, namely the area of the complex plane for which the MSF is positive. The colored lines display the locus of the eigenvalues of $\widetilde{\mathcal{L}}$ as a function of q, for a weighted hypergraph with $N = 20$ nodes, pairwise coupling coefficients fixed to $\sigma_1 = 0.195$, and $\sigma_2 = 0.7\sigma_1$. The color coding is such that the case $q = 0$ is represented in light red, while the case $q = 1/3$ in dark red. Panel B shows a zoom of the area close to the origin.

close to the origin. In Fig. 3.10, we can observe that an higher degree of symmetry in the hypergraph yields the desynchronization of the system of oscillators. In fact, we note how the eigenvalues of $\widetilde{\mathcal{L}}$ leave the stability region of the synchronous state for large enough q, which induces the desynchronization of the system. Conversely, in Fig. 3.5 displays the case where it is the directionality to destabilize the synchronization manifold. Indeed, we see that the eigenvalues leave the stability region for smaller values of q, which means that a more directed higher-order structure hampers the system synchronization.

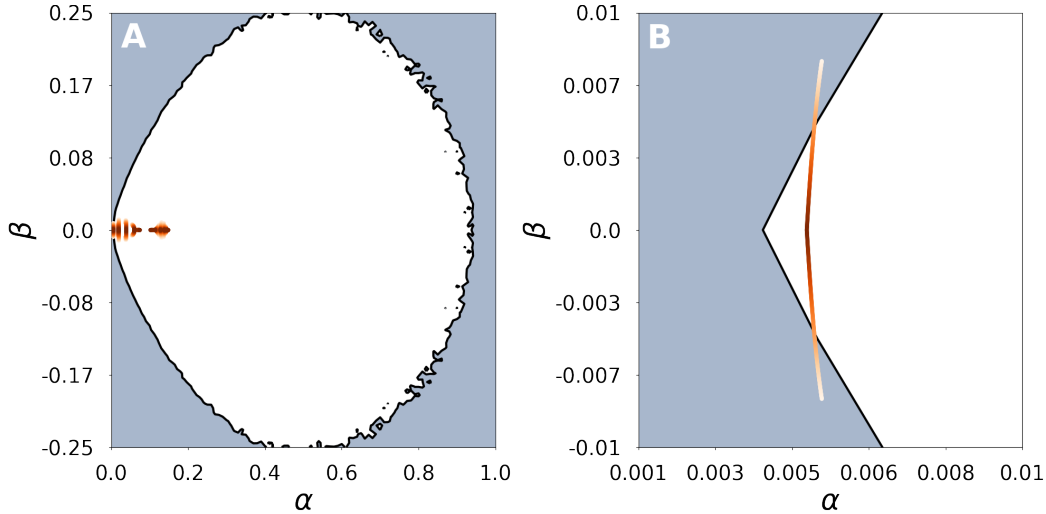As we have done for the first method of symmetrization, here we con-

Figure 3.11: Desynchronization induced by directionality, with the alternative symmetrization method. In the background, the white area represents the stability region of the synchronous state, identified by a negative MSF, the black line its boundary, while the light blue area the region where the synchronization manifold is unstable, namely the area of the complex plane for which the MSF is positive. The colored lines display the locus of the eigenvalues of $\widetilde{\mathcal{L}}$ as a function of q, for a weighted hypergraph with $N = 20$ nodes, pairwise coupling coefficients fixed to $\sigma_1 = 0.03$, and $\sigma_2 = 0.7\sigma_1$. The color coding is such that the case $q = 0$ is represented in light red, while the case $q = 1/3$ in dark red. Panel B shows a zoom of the area close to the origin.

clude the section analyzing the case of a system of Rössler oscillators coupled on the y-component. The dynamics of the systems is described in Eq. (3.6), where again $a_{ijk}^{(2)}$ is the element (i, j, k) of the adjacency tensor $\mathbf{A}^{(2)}(q)$ (see Eq. (3.7)). The first step would be to evaluate the MSF associated to system (3.6), but since this does not depend on the structure of the interactions, we can use the one calculated in the previous section. We analyze the effect of directionality in the $y - y$ coupling configuration in a system of $N = 20$ oscillators, with the structure of interactions given by the usual directed weighted hypergraph. We calculate the eigenvalues of
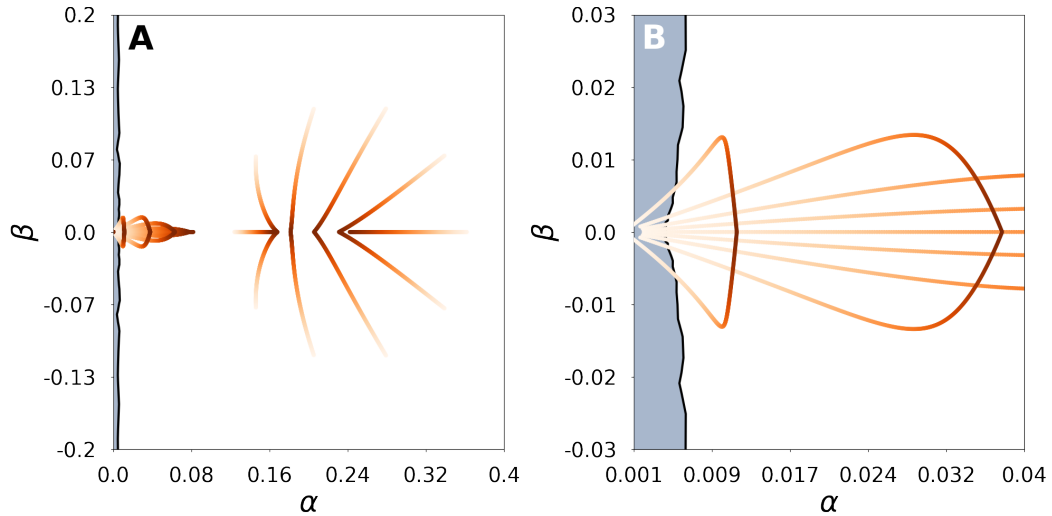
Figure 3.12: Desynchronization induced by directionality for a system of Rössler oscillators coupled on the y component, with the alternative symmetrization. In the background, the white area represents the stability region of the synchronous state, identified by a negative MSF, the black line its boundary, while the light blue area the region where the synchronization manifold is unstable, namely the area of the complex plane for which the MSF is positive. The colored lines display the locus of the eigenvalues of $\widetilde{\mathcal{L}}$ as a function of q, for a weighted hypergraph with $N = 20$ nodes, pairwise coupling coefficients fixed to $\sigma_1 = 0.001$ and $\sigma_2 = 0.12$. The color coding is such that the case $q = 0$ is represented in light red, while the case $q = 1/3$ in dark red. Panel B shows a zoom of the area close to the origin.

the effective Laplacian matrix $\widetilde{\mathcal{L}}$, studying how they vary as a function of the symmetry parameter q. To better appreciate the differences between the two symmetrization methods, we account for the same two sets of coupling coefficient σ_1 and σ_2, namely $\sigma_1 = 0.001$ and $\sigma_2 = 0.12$, and $\sigma_1 = 0.01$ and $\sigma_2 = 0.16$. The locus of the eigenvalues of in the two cases is shown in Figs. 3.12 and 3.12, respectively. The colored lines display the locus of the eigenvalues of $\widetilde{\mathcal{L}}$ as a function of q, so that the case $q = 0$ is shown in light red, while the case $q = 1/3$ in dark red. Panel B of both figures portrays a zoom of the area close to the origin. Coherently
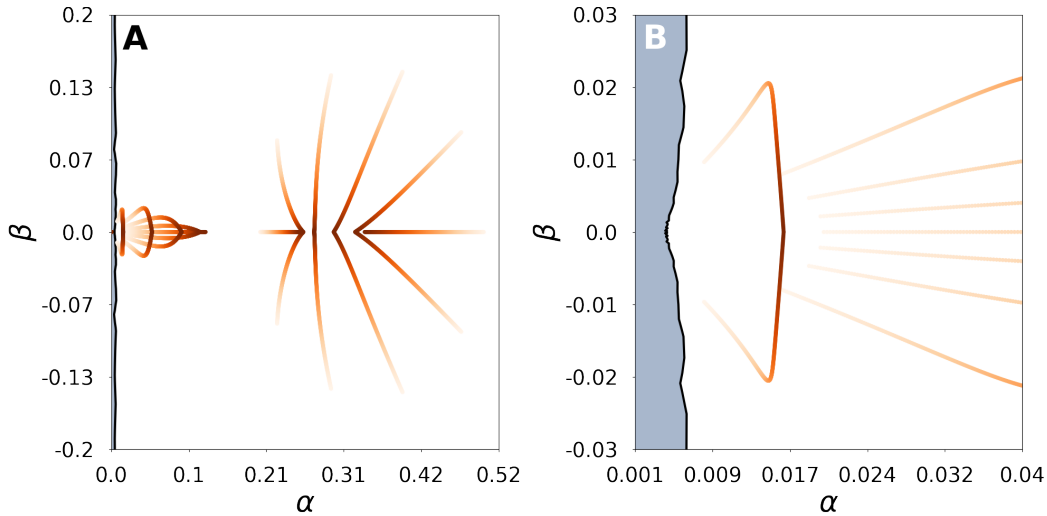
Figure 3.13: The shape of the MSF for a system of Rössler oscillators coupled on the y component does not permit the loss of synchronization by making the higher-order interactions symmetric, even with the alternative symmetrization. In the background, the white area represents the stability region of the synchronous state, identified by a negative MSF, the black line its boundary, while the light blue area the region where the synchronization manifold is unstable, namely the area of the complex plane for which the MSF is positive. The colored lines display the locus of the eigenvalues of $\widetilde{\mathcal{L}}$ as a function of q, for a weighted hypergraph with $N = 20$ nodes, pairwise coupling coefficients fixed to $\sigma_1 = 0.01$, and $\sigma_2 = 0.16$. The color coding is such that the case $q = 0$ is represented in light red, while the case $q = 1/3$ in dark red. Panel B shows a zoom of the area close to the origin.

with what we have observed for the first symmetrization method, we observe that the shape of the MSF permits to desynchronize the system by increasing the directionality of the higher-order structure, but it does not allow to do so the other way around. In particular, in Fig. 3.12, we see that a more directed hypergraph induces the loss of synchronization in the system. We note indeed that some of the eigenvalues of $\widetilde{\mathcal{L}}$ leave the stability region for small values of q. On the other hand, Fig. 3.13 show that, given the shape of the MSF, it is not possible to desynchronize the

system by making the hypergraph structure more symmetric, even with the alternative symmetrization described in this section. In fact, starting from a setting for which the synchronous state that is stable for $q = 0$, we observe that the eigenvalues of $\widetilde{\mathcal{L}}$ remain in the stability region for any value of the symmetry parameter q.

3.3 Synchronization in random hypergraphs

All the case studies presented so far have been carried out on a specific directed weighted hypergraph, that allowed us to tune the directionality of the higher-order structure so to study its impact on the synchronization of chaotic oscillators. The dynamical behavior of a system of coupled units depends on three main features, namely the dynamics of the isolated system, the functional form of the couplings, and the structure of the interactions. Once we set the first two, i.e., once we calculate the MSF, the determinant of the emergence of synchronization is the structure of the pairwise and higher-order interactions. As we have seen, this reflects in the position of the eigenvalues of the effective Laplacian matrix $\widetilde{\mathcal{L}}$ with respect to the stability region, as defined by the MSF. Hence, understanding the role of directionality on synchronization in other structures requires a characterization of the spectrum of the associated Laplacian matrix. To conclude this chapter, we introduce and analyze two generative models of random hypergraphs, which allows us to briefly discuss how different higher-order topologies affect the stability of the synchronization manifold.

We account for models that are a higher-order generalization of two well-studied random network generative models. First, we take a higher-order topology inspired by the Newman-Watts (NW) model [158]. To construct the hypergraph, we start from an undirected nonlocal ring of N nodes, each connected to its m nearest neighbors. Then, for each couple of nodes in the network, we add with probability ϕ a 1-directed 2-hyperedge pointing to a third node, chosen at random. Second, we consider a hypergraph generalization of the Erdős-Rényi (ER) model [159]. This generative model is defined by two parameters. The first, as in the classical ER model, is the probability ρ_1 of connecting two nodes via an undi-

rected link, while the second is the probability ρ_2 of adding a 1-directed 2-hyperedge among three nodes, pointing to a randomly chosen node of the triple.

As the hypergraphs are randomly generated, the eigenvalues of the associated Laplacian matrices $\widetilde{\mathcal{L}}$ are stochastic variables. Hence, to study the stability of the synchronization manifold in relation to the structure of the random hypergraphs, one needs to characterize the distribution of the eigenvalues in the complex plane. In particular, the spectrum of the Laplacian matrices varies as a function of the parameters of the generative models, of the coupling coefficients σ_1 and σ_2, and of the degree of symmetry of the higher-order structure p (without loss of generality, we have here accounted for the symmetrization that does not conserve the total coupling strength of the three-body interactions). As we want to compare how different topologies impact the synchronization behavior of the system, we set the parameters of the generative models so that the average number of links and the average number of 2-hyperedges pointing to each node are the same for the two algorithms. In particular, we take structures of $N = 20$ connected nodes. For the higher-order NW model we fix $m = \langle k^{(1)} \rangle = 4$ and $\phi = 0.5$, which results in an average number of hyperedges $\langle k_{\text{in}}^{(2)} \rangle = 4.75$. Note that this value, which varies as a function of the symmetry parameter p, refers to the case $p = 0$. Consistently, we set the values of ρ_1 and ρ_2 in the generalized ER model so that the average number of links and the average number of hyperedges are the same. By doing so, we compare structures with (on average) the same number of links and of hyperedges, arranged in two different ways. Having fixed the parameters of the generative models, we investigate how the distribution of the eigenvalues of $\widetilde{\mathcal{L}}$ depends on the symmetry parameter p and on the ratio $r_2 = \sigma_2/\sigma_1$, having fixed $\sigma_1 = 0.001$. For the first study, we set the value of the ratio to $r_2 = 30$, and we account for three values of the symmetry parameter, namely $p = 0$, $p = 0.5$, and $p = 1$. For the second, we fix $p = 0.5$, and consider the cases $r_2 = 10$, $r_2 = 30$, and $r_2 = 50$.

The results obtained for these two analyses are shown in Figs. 3.14 and 3.15, respectively. In both figures, panel A shows the eigenvalue distribution for the higher-order Newman-Watts model, while panel B the distribution for the higher-order Erdős-Rényi model, as a function of p and r_2 respectively. Starting from Fig. 3.14, we can observe two
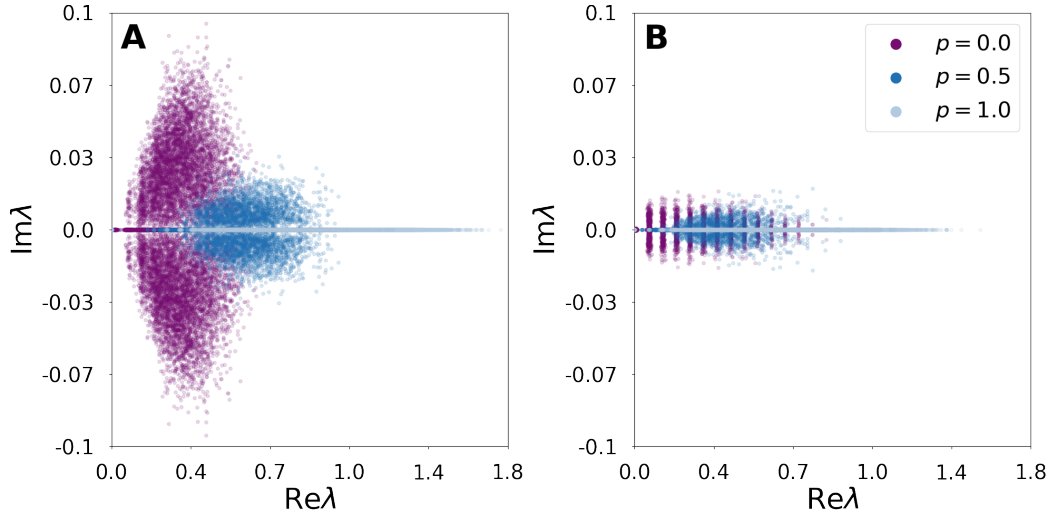
Figure 3.14: Variation of the eigenvalue distribution for the higher-order Newman-Watts model (panel A), and for the higher-order Erdős-Rényi model (panel B) as a function the symmetry parameter p. For both structure, we set $\langle k^{(1)} \rangle = 4$ and $\langle k_{\text{in}}^{(2)}(p = 0) \rangle = 4.75$. We also fix set the coupling coefficient $\sigma_1 = 0.001$, $\sigma_2 = r_2 \sigma_1$, while we fix the symmetry parameter to $p = 0.5$. Note that the distributions obtained for $p = 0.5$ are the same as those displayed in Fig. 3.15, with the label $r_2 = 30$.

aspects. First, for $p = 0$ we note that the eigenvalues distribution has a nonzero imaginary part, which shrinks to the real axis for $p = 1$. Second, we see that the imaginary part in the NW-like model is generally larger compared to that of the ER-like model. Intuitively, this difference shall be due to the fact that the NW model has a more circulant structure compared to the ER model, thus determining a larger imaginary part [70]. As regards, Fig. 3.15, we notice a similar behavior. In this case, the distribution of eigenvalues remains close to the real axis for smaller values of r_2, i.e., for smaller values of σ_2 compared to σ_1, while it spreads over the imaginary axis for larger values of r_2. Consistently to what we have observed for the study of p, the spectra obtained for the higher-order NW model usually have a larger imaginary part compared to that emerging from the higher-order ER model.

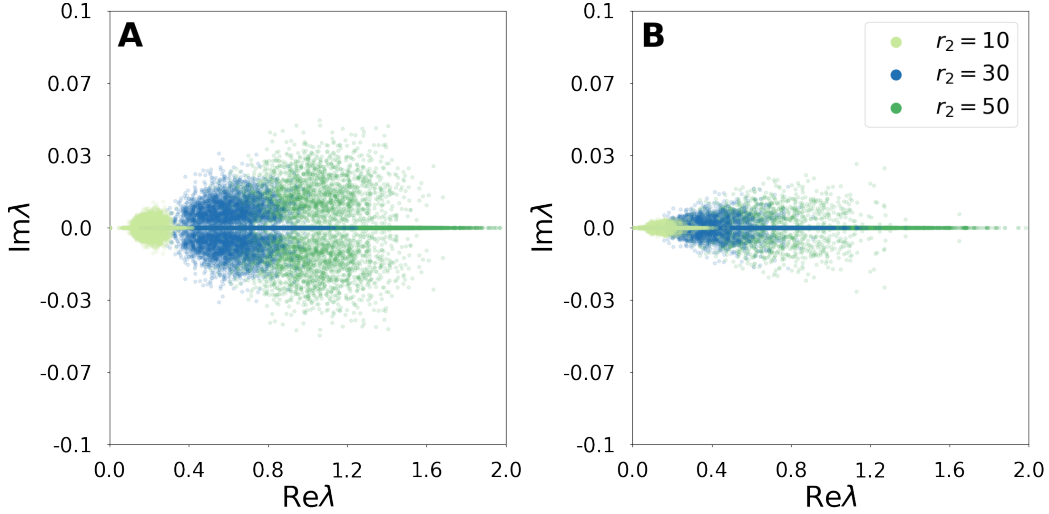To fully characterize the impact of topology on the synchronization

Figure 3.15: Variation of the eigenvalue distribution for the higher-order Newman-Watts model (panel A), and for the higher-order Erdős-Rényi model (panel B) as a function the ratio $r_2 = \sigma_1/\sigma_1$. For both structure, we set $\langle k^{(1)} \rangle = 4$ and $\langle k^{(2)}_{\text{in}}(p=0) \rangle = 4.75$. We also fix set the coupling coefficient $\sigma_1 = 0.001$, $\sigma_2 = r_2\sigma_1$, while we fix the symmetry parameter to $p = 0.5$. Note that the distributions obtained for $r_2 = 30$ are the same as those displayed in Fig. 3.14, with the label $p = 0.5$.

behavior of a system of coupled oscillators, we would need to find the conditions for which the eigenvalues of the effective Laplacian matrix $\widetilde{\mathcal{L}}$ are entirely contained in the stability region as defined by the MSF. Such a problem is not entirely new, as it also appears in the context of directed networks. However, despite a few attempts to study how the relationship between the distribution of the eigenvalues and the shape of the MSF affects the emergence of synchronization [30], the problem remains open. Such a problem is even more articulated for higher-order structures, as the effective Laplacian matrix $\widetilde{\mathcal{L}}$, whose eigenvalues determine the synchronization behavior of the system, encodes the contribution of multiple orders of interactions. Hence, a relevant follow-up of the analyses presented in this section would be to characterize how optimal different higher-order topologies are for synchronization, in terms of the probability that the associated eigenvalues distribution is contained in the stability

region, as defined by the MSF.

The results provided in this chapter conclude the analysis of synchronization in system of chaotic oscillators coupled through pairwise and higher-order interactions. In particular, here we have explored the role of nonreciprocal interactions on the stability of the synchronous state, showing how directionality can completely change the dynamical behavior of the system, either inducing its synchronization or its destabilization. Furthermore, we have given a few results aimed at showing how the eigenvalues distribution of random hypergraphs is affected by directionality and by the relationship between different orders of interactions.

Chapter 4

Turing pattern formation in high-order structures

In this chapter, we study the formation of Turing patterns in systems where both pairwise and higher-order interactions are present. We derive analytically the conditions for which patterns can emerge, showing how the presence of multi-body interactions affects the Turing instability. We begin by studying the case of a system where only pairwise interactions are active, investigating the role of nonlinear diffusion in pattern formation. Such an analysis will be used as a benchmark for studying the role of higher-order interactions. We begin the analysis of many-body interactions by exploring the case of coupling functions respecting natural coupling hypothesis. Then, we study the pattern formation in higher-order topologies whose associated Laplacian matrices commute. In particular, we consider two structures, namely a 2-lattice and a simplicial complex where all possible interactions among the nodes are active. Finally, we relax these constraints and we explore the most general setting of the problem, numerically investigating how higher-order interactions affect the formation of Turing patterns.

4.1 Turing patterns with nonlinear diffusion

As the objective of this chapter is to show how the presence of higher-order interactions affects pattern formation with respect to the classical scenario where only pairwise interactions are considered, we begin by studying this latter in details. From a mathematical point of view, this corresponds to analyze system (1.16) by setting $M = 1$. In particular, we aim at finding the necessary and sufficient conditions for the onset of Turing patterns in a system of units coupled through nonlinear diffusive-like functions. Hence, in the next sections we will investigate how higher-order interactions modify such conditions.

We begin our discussion by briefly illustrating the linear stability analysis presented in Sec. 1.3 for the specific case of Turing pattern formation. By setting $M = 1$, we can rewrite (1.16) as

$$
\begin{aligned}
\dot{u}_i &= f_u(u,v) + \sigma_1 \sum_{j=1}^{N} a_{ij}^{(1)} D_u^{(1)} \left[h_u^{(1)}(u_j) - h_u^{(1)}(u_i) \right], \\
\dot{v}_i &= f_v(u,v) + \sigma_1 \sum_{j=1}^{N} a_{ij}^{(1)} D_v^{(1)} \left[h_v^{(1)}(v_j) - h_v^{(1)}(v_i) \right].
\end{aligned}
\tag{4.1}
$$

We recall that in the analysis of Turing pattern formation one usually consider two species activator-inhibitor systems, so we have $\mathbf{x}_i = [u_i, v_i]^T$. We assume the isolated system to admit an equilibrium point $\mathbf{x}^* = [u^*, v^*]^T$, i.e., $f_u(u^*, v^*) = f_v(u^*, v^*) = 0$, which is also an homogeneous solution of system (4.1). Moreover, we assume the fixed point to be stable, which means to require

$$
\text{tr}\mathbf{JF} < 0 \quad \text{and} \quad \det\mathbf{JF} > 0,
\tag{4.2}
$$

where

$$
\mathbf{JF} = \begin{pmatrix} \frac{\partial f_u(u,v)}{\partial u} & \frac{\partial f_u(u,v)}{\partial v} \\ \frac{\partial f_v(u,v)}{\partial u} & \frac{\partial f_v(u,v)}{\partial v} \end{pmatrix}_{[u^*,v^*]^T}.
\tag{4.3}
$$

We perform a linear stability analysis around the equilibrium point, following the steps reported in Sec. 1.3. In particular, we write the equations governing the dynamics of the perturbations $\delta\mathbf{x}_i = [\delta u_i, \delta v_i]^T$, where

$\delta u_i = u_i - u^*$, and $\delta v_i = v_i - v^*$, which are

$$\delta\dot{\mathbf{x}}_i = \mathbf{JF}\delta\mathbf{x}_i - \sigma_1 \sum_j L_{ij}^{(1)}\mathbf{JH}^{(1)}\delta\mathbf{x}_j, \tag{4.4}$$

where we have used the notation

$$\mathbf{JH}^{(1)} = \begin{pmatrix} D_u^{(1)}\frac{\partial h_u^{(1)}(u)}{\partial u} & 0 \\[2mm] 0 & D_v^{(1)}\frac{\partial h_v^{(1)}(v)}{\partial v} \end{pmatrix}_{[u^*,v^*]^T}. \tag{4.5}$$

By introducing the stack vector $\delta\mathbf{x} = \left[\delta\mathbf{x}_1^T, \ldots, \delta\mathbf{x}_N^T\right]^T$, we can rewrite Eqs. (4.4) in block form, namely

$$\delta\dot{\mathbf{x}} = \left[\mathbb{I}_N \otimes \mathbf{JF} - \sigma_1\mathbf{L}^{(1)} \otimes \mathbf{JH}^{(1)}\right]\delta\mathbf{x}. \tag{4.6}$$

It is worth remarking a characteristic of the Laplacian matrix $\mathbf{L}^{(1)}$. Such a matrix is the discrete analogous of the continuous diffusion operator ∇^2, which is the main reason why it plays a role in the formation of Turing patterns on complex networks. In most of the literature on Turing patterns, this is defined as $L_{ij}^{(1)} = a_{ij}^{(1)} - k^{(1)}(i)\delta_{ij}$, so its eigenvalues are non-positive. However, consistently with the mathematical framework used so far, here we consider the definition of the Laplacian matrix given in Eq. (1.6), which has instead a non-negative spectrum.

Since the Laplacian matrix $\mathbf{L}^{(1)}$ is symmetric, as we are considering undirected networks, we can project Eqs. (4.6) onto the basis formed by the eigenvectors $\{\mathbf{v}_1, \ldots, \mathbf{v}_N\}$ of $\mathbf{L}^{(1)}$, thus separating the system of $2N$ coupled equations in N linear decoupled 2×2 equations, each one depending on a single eigenvalue $\lambda_i^{(1)}$ of $\mathbf{L}^{(1)}$. Formally, we have

$$\dot{\eta}_i = \left[\mathbf{JF} - \sigma_1\lambda_i^{(1)}\mathbf{JH}^{(1)}\right]\eta_i, \tag{4.7}$$

where $\eta_i = [\delta\tilde{u}_i, \delta\tilde{v}_i]^T$, being $\delta\tilde{u}_i$ and $\delta\tilde{v}_i$ the projections of δu_i and δv_i, respectively, on the eigenbasis of $\mathbf{L}^{(1)}$. As explained in Sec. 1.3, the equation corresponding to the eigenvalue $\lambda_1^{(1)} = 0$ is the one governing the dynamics of the space-independent part of the system, i.e., the isolated

system, while the others are those associated to the spatial part. As the equations for the spatial part have the same form, we can consider a single parametric variational equation, namely

$$\dot{\zeta} = \left[\mathbf{JF} - \alpha \mathbf{JH}^{(1)} \right] \zeta, \tag{4.8}$$

where α is a real-valued parameter. The stability of the homogeneous solution, i.e., $\delta \mathbf{x} = \mathbf{0}$, is determined by the eigenvalues of the matrix

$$\mathbf{J}^{\alpha} = \mathbf{JF} - \alpha \mathbf{JH}^{(1)}. \tag{4.9}$$

It is here crucial to remark a feature making the analysis of Turing pattern formation a relevant application of our mathematical framework. The matrix $\mathbf{J}^{\alpha}$ is time-independent, so it is possible to derive the necessary conditions for the stability of the homogeneous solution $\mathbf{x}^*$ analytically. This is in contrast with the case of synchronization, where the MSF, namely the maximum Lyapunov exponent associated to the Master Stability Equation, had to be calculated numerically. In facts, in the present case we can calculate the eigenvalues of $\mathbf{J}^{\alpha}$ by solving the equation

$$\Lambda^2 - 2\mathrm{tr}\mathbf{J}^{\alpha}\Lambda + \mathrm{det}\mathbf{J}^{\alpha} = 0. \tag{4.10}$$

The solution with the largest real part, considered as a function of α takes the name of *dispersion relation*. If there exists a value of α such that $\mathrm{Re}\Lambda_{\alpha} > 0$, then the fixed point $[u^*, v^*]^T$ is unstable, and the formation of Turing patterns is observed. As $\mathrm{tr}\mathbf{J}^{\alpha} < 0$, from Eq. (4.10) we can derive a necessary condition for Λ_{α} to be positive. In facts, assuming $\partial h_u^{(1)}(u)/\partial u|_{u^*} > 0$ and $\partial h_v^{(1)}(v)/\partial v|_{v^*} > 0$, and being $\lambda_i^{(1)} > 0$ and $\mathrm{tr}\mathbf{JF} < 0$, we have $\mathrm{tr}\mathbf{J}^{\alpha} < 0$, so a necessary condition for the formation of Turing pattern is

$$\mathrm{det}\mathbf{J}^{\alpha} < 0. \tag{4.11}$$

Such a condition is also sufficient if there is an eigenvalue $\lambda_i^{(1)}$ such that $\mathrm{det}\mathbf{J}^{\tilde{\alpha}} < 0$, with $\tilde{\alpha} = \sigma_1 \lambda_i^{(1)}$. We remark that the evaluation of $\mathrm{Re}\Lambda_{\alpha}$ as a continuous function of α corresponds to the study of Turing pattern formation on a continuous media, as long as α is interpreted as the square of the wave number k, associated to a spatial Fourier mode [67].

To substantiate the theoretical derivations presented above, let us now focus on a specific example of reaction-diffusion system. As concerns the reactive part, i.e., the dynamics of the isolated system, we consider the well known Brusselator model, which finds application in the study of oscillations in auto-catalytic chemical reactions [160, 161, 162]. In particular, the dynamics of the model is governed by the set of equations

$$\dot{u} = f_u(u, v) = 1 - (b + 1)u + cu^2v,$$
$$\dot{v} = f_v(u, v) = bu - cu^2v,$$

(4.12)

where $b, c > 0$. Such a model has a single equilibrium point $[u^*, v^*]^T = [1, b/c]^T$, and the Jacobian matrix evaluated at it is given by

$$\mathbf{JF} = \begin{pmatrix} b - 1 & c \\ -b & -c \end{pmatrix}.$$

(4.13)

According to condition (4.2), such a fixed point is stable if $\mathrm{tr}\mathbf{JF} = b - c - 1 < 0$, as $\det\mathbf{JF} = c > 0$ is verified by definition. We account for N identical Brusselator systems, coupled via nonlinear diffusion functions. In particular, we consider cubic diffusion-like functions, namely setting

$$h_u^{(1)}(u) = u^3 \quad \text{and} \quad h_v^{(1)}(v) = v^3.$$

(4.14)

Let us stress that Turing pattern formation with nonlinear diffusion has already been studied in the case of a continuous space [135, 136], so the following analysis simply represents its counterpart in networked systems. Hence, the main goal of this section is to set up the study of higher-order interactions. Under these assumptions, system (4.1) can be written as

$$\dot{u}_i = 1 - (b + 1)u_i + cu_i^2v_i + \sigma_1 \sum_{j=1}^{N} a_{ij}^{(1)} D_u^{(1)} \left(u_j^3 - u_i^3 \right),$$

$$\dot{v}_i = bu_i - cu_i^2v_i + \sigma_1 \sum_{j=1}^{N} a_{ij}^{(1)} D_v^{(1)} \left(v_j^3 - v_i^3 \right).$$

(4.15)

To calculate the matrix $\mathbf{J}^\alpha$ associated to the linearization of system

(4.15), one needs to evaluate the matrix $\mathbf{JH}^{(1)}$, which is given by

$$\mathbf{JH}^{(1)} = 3 \begin{pmatrix} D_u^{(1)} & 0 \\ 0 & D_v^{(1)} \left(\frac{b}{c}\right)^2 \end{pmatrix}. \tag{4.16}$$

Given the matrices $\mathbf{JF}$ and $\mathbf{JH}^{(1)}$, we can now derive condition (4.11) for the system (4.15) explicitly, namely

$$\begin{cases} (b-1)b^2 D_v^{(1)} - c^3 D_u^{(1)} > 0, \\ 4b^2 c^3 D_u^{(1)} D_v^{(1)} - \left[(b-1)b^2 D_v^{(1)} - c^3 D_u^{(1)}\right]^2 < 0, \end{cases} \tag{4.17}$$

which guarantees that $\det \mathbf{J}^\alpha < 0$ for some values of α. It is crucial to observe that these conditions do not depend on α itself. This means that, consistently with the MSF approach, they do not depend on the particular topology chosen. Hence, we can first derive a continuous dispersion relation that only depends on the dynamics of the non-spatial system and on the functional form of the couplings, checking *a posteriori* whether $\det \mathbf{J}^\alpha$ is negative for some eigenvalues of the Laplacian matrix $\mathbf{L}^{(1)}$.

From Eq. (4.17) we can derive a condition on the diffusion coefficients, which is

$$b^2 D_v^{(1)} > c^2 D_u^{(1)}. \tag{4.18}$$

This is an extension of the classic condition $D_v^{(1)} > D_u^{(1)}$ to the case of cubic diffusive-like coupling functions. Condition (4.18) derives from imposing $\mathrm{tr}\mathbf{JF} < 0$, which in the case of the Brusselator model is equivalent to the inequality $b - 1 < c$. In facts, from the first condition in Eq. (4.17), we can write

$$(b-1)b^2 D_v^{(1)} > c^3 D_u^{(1)} \Rightarrow (b-1)b^2 D_v^{(1)} > c^3 D_u^{(1)} > (b-1)c^2 D_u^{(1)}, \tag{4.19}$$

where the implication derives from the condition on the trace of $\mathbf{JF}$. Condition (4.18), which has been derived for a general reactive system and for continuous support in [135], implies that patterns can emerge even when the activators, i.e., the u species, diffuse faster than the inhibitors, i.e., the v species, in contrast with what is predicted by the classic Turing instability theory.

In the next two sections we will study whether and how conditions (4.17) are affected by the presence of higher-order interactions. First, we will study the case where the pairwise and the higher-order interaction functions satisfy the natural coupling hypothesis. Then, we will analyze a broader class of interaction functions by restricting the range of possible higher-order structures to a few regular topologies. Finally, we will provide a glimpse of the most general case, where both the structure and the functional form of the couplings have no further limitation.

4.2   The case of natural coupling

As a first study of the role of higher-order interactions on the emergence of Turing patterns, here we examine the case of natural coupling. As we have done for the analysis of synchronization, for simplicity and without loss of generality, we consider only two-body and three-body interactions, i.e., we set $M = 2$. In particular, we account for a system of N Brusselator models, coupled through cubic diffusive-like interaction functions, with no cross-diffusion terms. Therefore, for two-body interactions we take $\mathbf{h}^{(1)}(u_j, v_j) = [D_u^{(1)} h_u^{(1)}(u_j), D_v^{(1)} h_v^{(1)}(v_j)]^T$, with $h_u^{(1)}(u_j) = u_j^3$ and $h_v^{(1)}(v_j) = v_j^3$, while for three-body interactions we consider $\mathbf{h}^{(2)}(u_j, v_j, u_k, v_k) = [D_u^{(2)} h_u^{(2)}(u_j, u_k), D_v^{(2)} h_v^{(2)}(v_j, v_k)]^T$, with $h_u^{(2)}(u_j, u_k) = u_j^2 u_k$ and $h_v^{(2)}(v_j, v_k) = v_j^2 v_k$. Note that the functions $\mathbf{h}^{(1)}$ and $\mathbf{h}^{(2)}$ satisfy the natural coupling hypothesis as long as $D_u^{(1)} = D_u^{(2)}$ and $D_v^{(1)} = D_v^{(2)}$, as explained in Sec. 1.3.2. Under these assumptions, Eqs. (1.16) can be

written as

$$
\begin{aligned}
\dot{u}_i =& 1 - (b+1)u_i + cu_i^2 v_i + \sigma_1 \sum_{j=1}^{N} a_{ij}^{(1)} D_u^{(1)} \left(u_j^3 - u_i^3 \right) + \\
& + \sigma_2 \sum_{j,k=1}^{N} a_{ijk}^{(2)} D_u^{(1)} \left(u_j^2 u_k - u_i^3 \right), \\
\dot{v}_i =& bu_i - cu_i^2 v_i + \sigma_1 \sum_{j=1}^{N} a_{ij}^{(1)} D_v^{(1)} \left(v_j^3 - v_i^3 \right) + \\
& + \sigma_2 \sum_{j,k=1}^{N} a_{ijk}^{(2)} D_v^{(1)} \left(v_j^2 v_k - v_i^3 \right).
\end{aligned}
\tag{4.20}
$$

Similarly to what we have done for the case with pairwise interactions only, we can perform a linear stability analysis of Eqs. (4.20) around the fixed point $[u^*, v^*]^T = [1, b/c]^T$, following the steps detailed in Sec. 1.3.2. In the end, we arrive to the block equation

$$
\delta \dot{\mathbf{x}} = \left[\mathbb{I}_N \otimes \mathbf{JF} - \sigma_1 \mathcal{L} \otimes \mathbf{JH}^{(1)} \right] \delta \mathbf{x},
\tag{4.21}
$$

where $\mathcal{L} = \mathbf{L}^{(1)} + r_2 \mathbf{L}^{(2)}$, being $\mathbf{L}^{(1)}$ and $\mathbf{L}^{(2)}$ the Laplacian matrices encoding the two-body and three-body interactions, respectively, while $r_2 = \sigma_2/\sigma_1$. We recall that, given the natural coupling hypothesis, we have $\mathbf{JH}^{(1)} = \mathbf{JH}^{(2)}$. We observe that such a system of equations is formally equivalent to the one obtained considering pairwise interactions only, i.e., Eqs. (4.6). Hence, when the coupling functions respect the natural coupling hypothesis, the necessary conditions for the formation of Turing patterns in a system of coupled Brusselator models, namely Eq. (4.17), are not altered by the presence of higher-order interactions. Differently from the previous case, however, the stability of the fixed point $[u^*, v^*]^T$ is determined by the nonzero eigenvalues λ_i of $\mathcal{L}$, depending on both the two-body interactions, through the Laplacian matrix $\mathbf{L}^{(1)}$, and the three-body interactions, through $\mathbf{L}^{(2)}$. In particular, if there is an eigenvalue λ_i such that $\det \mathbf{J}^{\tilde{\alpha}} < 0$, with $\tilde{\alpha} = \sigma_1 \lambda_i$, then Turing patterns emerge.

To confirm the theoretical expectations, we consider the following example. We set the parameters of the Brusselator model to $b = 3$, and
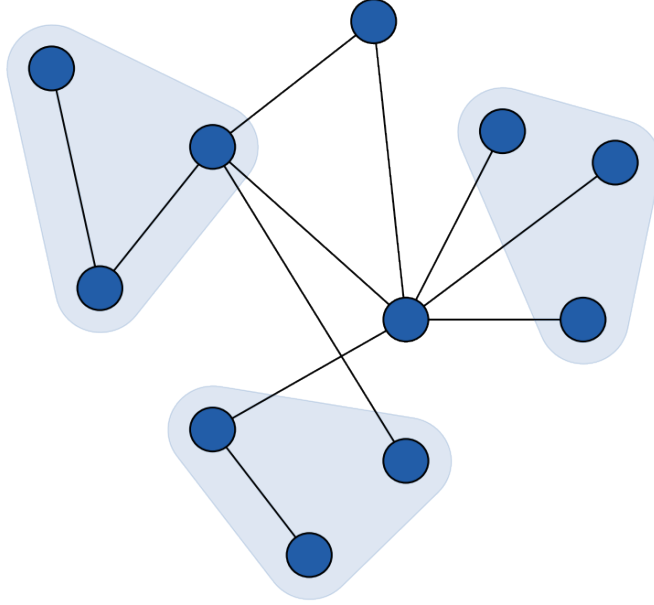
Figure 4.1: A graphical representation of the hypergraph considered to simulate Eqs. (4.20).

$c = 3.5$, the diffusion coefficients to $D_u^{(1)} = 0.1$, and $D_v^{(1)} = 2$, and the coupling strengths to $\sigma_1 = \sigma_2 = 1$. One can easily verify that with this setting conditions (4.17) hold, so Turing patterns can form. We consider a system of $N = 11$ coupled Brusselator models, interacting according to a generic higher-order structure, which is shown in Fig. 4.1. For this structure, we calculate the eigenvalues of the associated Laplacian matrix $\mathcal{L}$, and study whether there is at least one λ_i for which $\det \mathbf{J}^\alpha < 0$. The results obtained are shown in panel A of Fig. 4.2. In particular, the blue curve corresponds to the continuous dispersion relation, obtained by solving the eigenvalue problem (4.10) associated to system (4.20), while the orange dots are the values of $\text{Re}\Lambda_\alpha$ obtained for $\alpha = \sigma_1 \lambda_i$. We can observe that a few eigenvalues of $\mathcal{L}$ are such that the $\text{Re}\Lambda_\alpha > 0$, which is a sufficient condition for the formation of Turing patterns. To confirm whether patterns emerge, we perform simulation of system (4.20) on the hyper-
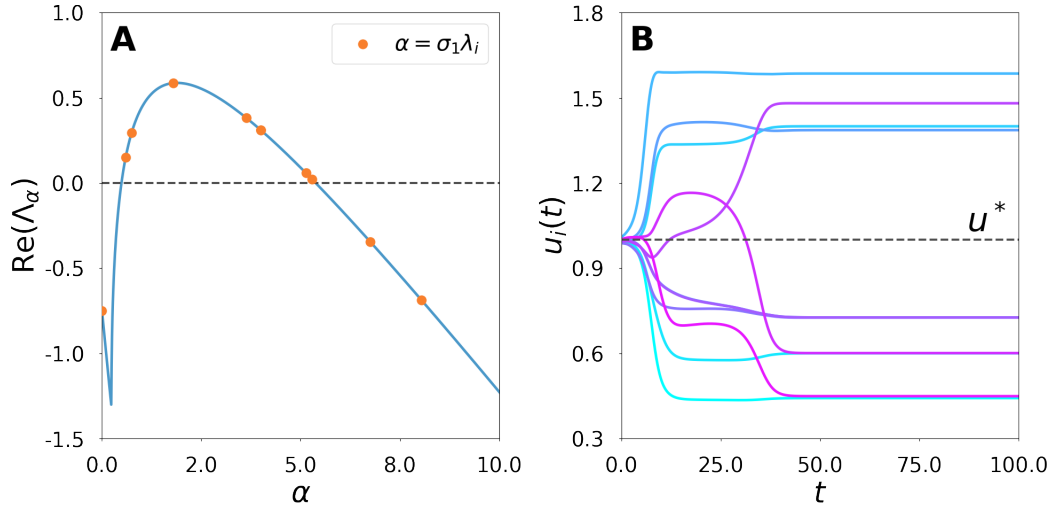
Figure 4.2: Formation of Turing patterns in higher-order structures under the natural coupling hypothesis. Panel A shows the dispersion relation $\text{Re}\Lambda_\alpha$ for system (4.20) (continuous blue line), as well as its value for $\alpha = \sigma_1 \lambda_i$ (orange dots) , where λ_i are the eigenvalues of the Laplacian matrix associated to the hypergraph shown in Fig. 4.1. Panel B shows the formation of Turing patterns on the u-component in the dynamics of (4.20), which has been simulated on the structure in Fig. 4.1. The panels are obtained by setting the Brusselator parameters to $b = 3$, and $c = 3.5$, the diffusion coefficients to $D_u^{(1)} = 0.1$, and $D_v^{(1)} = 2$, and the coupling strengths to $\sigma_1 = \sigma_2 = 1$.

graph shown in Fig. 4.1. We set each node to an initial condition close to the equilibrium point $[u^*, v^*]^T$, and we integrate Eq. (4.20) using a Runge-Kutta fourth-order method with integration time step $dt = 5 \cdot 10^{-3}$. The initial conditions of the oscillators are generated by perturbing the fixed point with a random perturbation of size 10^{-2}. Panel B of Fig. 4.2 shows the dynamics of the u-component for each node. As we can observe, each u_i converges to a value different from that of the equilibrium point, i.e., $u^* = 1$, and so patterns are formed. A similar result can be seen for the v-component of the oscillators, though this is not shown to avoid redundancy.

4.3 The case of commutative Laplacian matrices

We now move to the study of higher-order topologies whose associated Laplacian matrices commute, which still guarantees the possibility to derive a dispersion relation that determines the stability of the system. In particular, we will account for two structures, namely the 2-lattice and the simplicial complex where all two-body and three-body interactions are active. We again consider a system of N Brusselator models, coupled through cubic diffusive-like interaction functions, with no cross-diffusion terms. For two-body interactions we take $\mathbf{h}^{(1)}(u_j, v_j) = [D_u^{(1)} h_u^{(1)}(u_j), D_v^{(1)} h_v^{(1)}(v_j)]^T$, with $h_u^{(1)}(u_j) = u_j^3$ and $h_v^{(1)}(v_j) = v_j^3$, while for higher-order interactions we consider $\mathbf{h}^{(2)}(u_j, v_j, u_k, v_k) = [D_u^{(2)} h_u^{(2)}(u_j, u_k), D_v^{(2)} h_v^{(2)}(v_j, v_k)]^T$, with $h_u^{(2)}(u_j, u_k) = u_j^2 u_k$ and $h_v^{(2)}(v_j, v_k) = v_j^2 v_k$. Note that, differently from the case presented in the previous section, here we do not assume the equivalence of the diffusion coefficients at the various orders, meaning that in general we have $D_u^{(1)} \neq D_u^{(2)}$ and $D_v^{(1)} \neq D_v^{(2)}$. Under these assumptions, Eqs. (1.16) can be written as

$$
\begin{aligned}
\dot{u}_i =& 1 - (b+1)u_i + c u_i^2 v_i + \sigma_1 \sum_{j=1}^N a_{ij}^{(1)} D_u^{(1)} \left(u_j^3 - u_i^3 \right) + \\
& + \sigma_2 \sum_{j,k=1}^N a_{ijk}^{(2)} D_u^{(2)} \left(u_j^2 u_k - u_i^3 \right), \\
\dot{v}_i =& b u_i - c u_i^2 v_i + \sigma_1 \sum_{j=1}^N a_{ij}^{(1)} D_v^{(1)} \left(v_j^3 - v_i^3 \right) + \\
& + \sigma_2 \sum_{j,k=1}^N a_{ijk}^{(2)} D_v^{(2)} \left(v_j^2 v_k - v_i^3 \right).
\end{aligned}
\tag{4.22}
$$

Let us begin from the case of a system of oscillators coupled in a 2-lattice, for which we crucially have that $\mathbf{L}^{(2)} = 2\mathbf{L}^{(1)}$. By performing a linear stability analysis, so by linearizing Eqs. (4.22) around the fixed point $[u^*, v^*]^T = [1, b/c]^T$, following the steps detailed in Sec. 1.3.1, we obtain the block equation

$$
\delta \dot{\mathbf{x}} = \left[\mathbb{I}_N \otimes \mathbf{JF} - \sigma_1 \mathbf{L}^{(1)} \otimes \left(\mathbf{JH}^{(1)} + 2r_2 \mathbf{JH}^{(2)} \right) \right] \delta \mathbf{x},
\tag{4.23}
$$

where $\mathbf{JH}^{(1)}$ is the same as in Eq. (4.16), while $\mathbf{JH}^{(2)}$ is given by

$$\mathbf{JH}^{(2)} = 3 \begin{pmatrix} D_u^{(2)} & 0 \\ 0 & D_v^{(2)} \left(\frac{b}{c}\right)^2 \end{pmatrix}. \qquad (4.24)$$

For the case in exam, we can define two *effective diffusion coefficients*

$$\mathcal{D}_u^{\text{latt}} = D_u^{(1)} + 2r_2 D_u^{(2)} \text{ and } \mathcal{D}_v^{\text{latt}} = D_v^{(1)} + 2r_2 D_v^{(2)}, \qquad (4.25)$$

which allows us to write Eqs. (4.23) as

$$\delta \dot{\mathbf{x}} = \left[\mathbb{I}_N \otimes \mathbf{JF} - \sigma_1 \mathbf{L}^{(1)} \otimes \mathcal{JH}^{\text{latt}} \right] \delta \mathbf{x}, \qquad (4.26)$$

where

$$\mathcal{JH}^{\text{latt}} = \mathbf{JH}^{(1)} + 2r_2 \mathbf{JH}^{(2)} = 3 \begin{pmatrix} \mathcal{D}_u^{\text{latt}} & 0 \\ 0 & \mathcal{D}_v^{\text{latt}} \left(\frac{b}{c}\right)^2 \end{pmatrix}. \qquad (4.27)$$

Similarly to the case of natural coupling, Eqs. (4.26) are formally equivalent to Eqs. (4.6), obtained by considering pairwise interactions only. This time, however, conditions (4.17) are written in terms of the effective diffusion coefficients $\mathcal{D}_u^{\text{latt}}$ and $\mathcal{D}_v^{\text{latt}}$, namely

$$\begin{cases} (b-1)b^2 \mathcal{D}_v^{\text{latt}} - c^3 \mathcal{D}_u^{\text{latt}} > 0, \\ 4b^2c^3 \mathcal{D}_u^{\text{latt}} \mathcal{D}_v^{\text{latt}} - \left[(b-1)b^2 \mathcal{D}_v^{\text{latt}} - c^3 \mathcal{D}_u^{\text{latt}} \right]^2 < 0. \end{cases} \qquad (4.28)$$

Compared to Eqs. (4.17), we note that conditions (4.28) depend on the coupling coefficients, as the effective diffusion coefficients $\mathcal{D}_u^{\text{latt}}$, $\mathcal{D}_v^{\text{latt}}$ are functions of the ratio $r_2 = \sigma_2/\sigma_1$. Hence, a variation in the relative strength of the higher-order interactions with respects to the pairwise interactions can affect the formation of Turing patterns, either inducing or preventing it. Also in this case, from the first inequality of Eqs. (4.28) we can derive a compact necessary condition on the diffusive coefficients, which is

$$b^2(D_v^{(1)} + 2r_2 D_v^{(2)}) > c^2(D_u^{(1)} + 2r_2 D_u^{(2)}). \qquad (4.29)$$
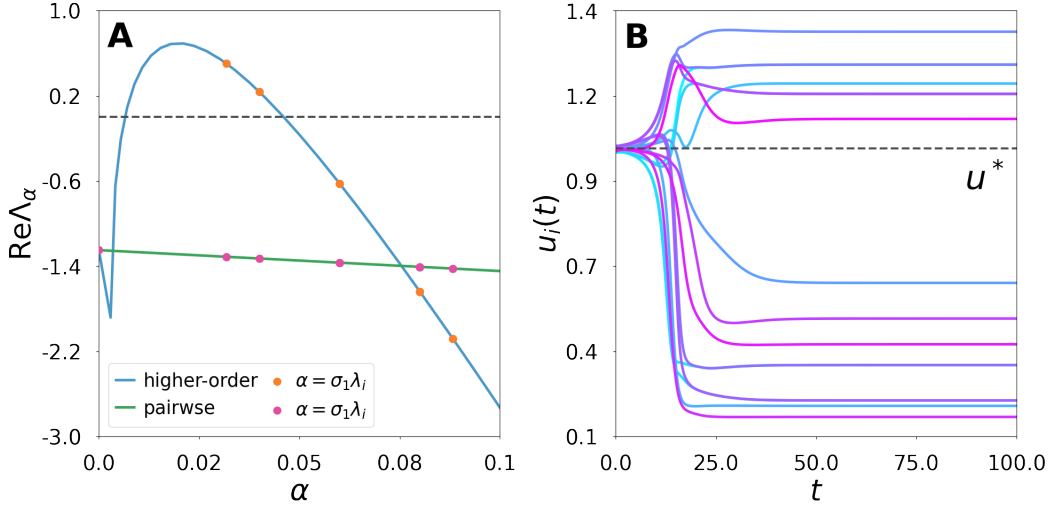
Figure 4.3: Formation of Turing patterns on a 2-lattice. Panel A displays the dispersion relations $\text{Re}(\Lambda_\alpha)$ associated to (4.20) (pairwise coupling only, continuous green line) and to system (4.22) (higher-order coupling, continuous blue line), as well as their value for $\alpha = \sigma_1 \lambda_i^{(1)}$ (orange and pink dots respectively), where $\lambda_i^{(1)}$ are the eigenvalues of the standard Laplacian matrix associated to a 2-lattice with $N = 16$ nodes and periodic boundary conditions. Panel B shows the formation of Turing patterns on the u-component in the dynamics of (4.22), simulated on the 2-lattice. The panels are obtained by setting the Brusselator parameters to $b = 5.5$, and $c = 7$, the pairwise diffusion coefficients to $D_u^{(1)} = 1$, and $D_v^{(1)} = 0.5$, the three-body diffusion coefficients to $D_u^{(2)} = 0.1$, and $D_v^{(2)} = 1$, and the coupling strengths to $\sigma_1 = 0.01$ and $\sigma_2 = 1$.

As an example, we analyze two settings of system (4.22). First, we study a case for which the presence of higher-order interactions allows for the formation of Turing patterns, under the assumption that no pattern emerges when considering pairwise interactions only. Then, we investigate the opposite scenario where three-body interactions suppress the formation of patterns induced by the two-body couplings. For the first, we set the parameters of the Brusselator model to $b = 5.5$, and $c = 7$, the pairwise diffusion coefficients to $D_u^{(1)} = 1$, and $D_v^{(1)} = 0.5$, the

higher-order coefficients to $D_u^{(2)} = 0.1$, and $D_v^{(2)} = 1$, while the coupling strengths are fixed to $\sigma_1 = 0.01$ and $\sigma_2 = 1$, which means $r_2 = 100$. We observe that conditions (4.17) do not hold, whereas conditions (4.28) are verified, meaning that Turing patterns can emerge only when three-body interactions are present. We consider a network of $N = 16$ coupled Brusselator models, arranged as a 2-lattice with periodic boundary conditions. For this latter, we evaluate the eigenvalues of the standard Laplacian matrix $\mathbf{L}^{(1)}$, and check if we have $\det \mathbf{J}^\alpha < 0$ for at least one of them. Panel A of Fig. 4.3 shows the results obtained when accounting for either the sole two-body interactions or two-body and three-body interactions together. As expected from the theory, while the dispersion relation associated to (4.15) lies below the axis $\mathrm{Re}\Lambda_\alpha = 0$ (green line), the one associated to system (4.22) crosses the axis (blue line), meaning that Turing patterns can emerge on a continuous support when higher-order interactions are active. The orange and the pink dots correspond to the values of $\mathrm{Re}\Lambda_\alpha$ obtained for $\alpha = \sigma_1 \lambda_i^{(1)}$, in the two settings considered. As we can observe, when we account for higher-order interactions, two eigenvalues of $\mathbf{L}^{(1)}$ yields $\mathrm{Re}\Lambda_\alpha > 0$, so Turing patterns can emerge on the 2-lattice. This is confirmed by the simulation of system (4.22). In facts, in panel B of Fig. 4.3 we observe that each u_i diverges from the equilibrium point $u^* = 1$, thus patterns are formed. The dynamics of u_i are obtained by fixing an initial condition close to the equilibrium point $[u^*, v^*]^T$, and integrating Eq. (4.22) using a Runge-Kutta fourth-order method with integration time step $dt = 5 \cdot 10^{-3}$. The initial conditions are generated by perturbing the fixed point with a random perturbation of size 10^{-2}.

For the second example, we set the Brusselator parameters to $b = 5.5$, and $c = 7$, the two-body and three-body diffusion coefficients to $D_u^{(1)} = 0.1$, $D_v^{(1)} = 1.5$, and $D_u^{(2)} = 1$, $D_v^{(2)} = 0.5$, respectively, and the coupling strengths to $\sigma_1 = 0.7$ and $\sigma_2 = 0.2$, yielding $r_2 = 0.29$. In this case, conditions (4.17) are verified, while conditions (4.28) are not, so we expect higher-order interactions to prevent the formation of Turing patterns, which would be allowed accounting for pairwise interactions only. Again, we consider a 2-lattice with $N = 16$ nodes, and periodic boundary conditions, and we calculate the eigenvalues of $\mathbf{L}^{(1)}$. Panel A of Fig. 4.4 shows the results obtained when accounting for either the sole
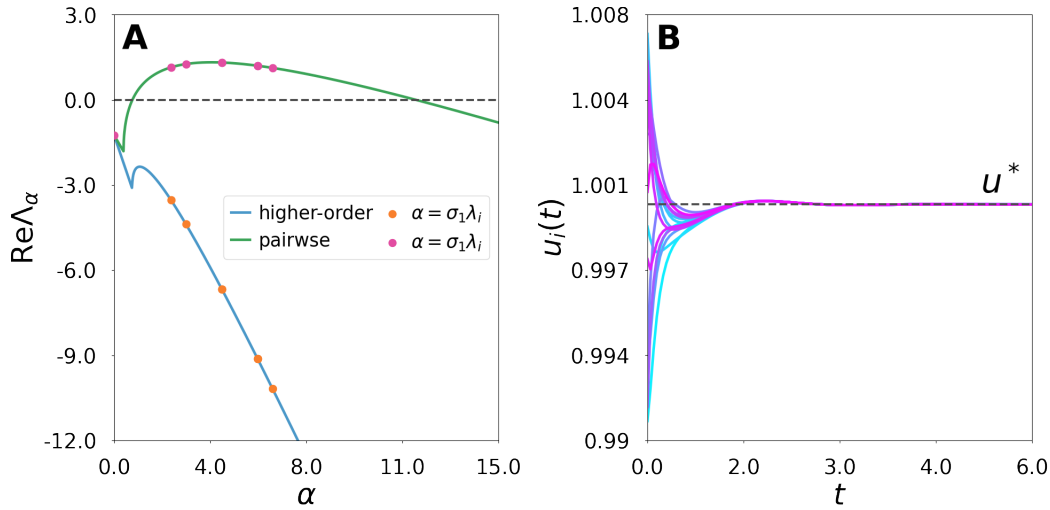
Figure 4.4: Suppression of Turing patterns on a 2-lattice. Panel A displays the dispersion relations $\mathrm{Re}(\Lambda_\alpha)$ associated to (4.20) (pairwise coupling only, continuous green line) and to system (4.22) (higher-order coupling, continuous blue line), as well as their value for $\alpha = \sigma_1 \lambda_i^{(1)}$ (orange and pink dots respectively), where $\lambda_i^{(1)}$ are the eigenvalues of the standard Laplacian matrix associated to a 2-lattice with $N = 16$ nodes and periodic boundary conditions. Panel B shows the formation of Turing patterns on the u-component in the dynamics of (4.22), simulated on the 2-lattice. The panels are obtained by setting the Brusselator parameters to $b = 5.5$, and $c = 7$, the pairwise diffusion coefficients to $D_u^{(1)} = 0.1$, and $D_v^{(1)} = 1.5$, the three-body diffusion coefficients to $D_u^{(2)} = 1$, and $D_v^{(2)} = 0.5$, and the coupling strengths to $\sigma_1 = 0.7$ and $\sigma_2 = 0.2$.

two-body interactions or two-body and three-body interactions together. We observe that the dispersion relation associated to (4.15) crosses the axis $\mathrm{Re}\Lambda_\alpha = 0$ (green line), while the one associated to system (4.22) does not (blue line), which means that Turing patterns can not emerge when higher-order interactions are present. Once again, we represent as orange and pink dots the values of $\mathrm{Re}\Lambda_\alpha$ obtained for $\alpha = \sigma_1 \lambda_i^{(1)}$, for the two settings considered. The temporal evolution of the u-component of system (4.22) is shown in panel B of Fig. 4.4. We note that all u_i converge to

the equilibrium point $u^* = 1$, confirming that higher-order interactions hamper the formation of Turing patterns. The dynamics is again obtained by fixing an initial condition close to the equilibrium point $[u^*, v^*]^T$, and integrating Eq. (4.22) using a Runge-Kutta fourth-order method with integration time step $dt = 5 \cdot 10^{-3}$. The initial conditions are generated by perturbing the fixed point with a random perturbation of size 10^{-2}.

We now take into account the all-to-all case. As explained in Sec. 1.3.1, for this latter we have that $\mathbf{L}^{(2)} = (N-2)\mathbf{L}^{(1)}$, so by linearizing Eqs. (4.22) around the fixed point $[u^*, v^*]^T = [1, b/c]^T$ we obtain the equation

$$\delta\dot{\mathbf{x}} = \left[\mathbb{I}_N \otimes \mathbf{JF} - \sigma_1 \mathbf{L}^{(1)} \otimes \left(\mathbf{JH}^{(1)} + (N-2)r_2\mathbf{JH}^{(2)} \right) \right] \delta\mathbf{x}, \qquad (4.30)$$

where $\mathbf{JH}^{(1)}$ and $\mathbf{JH}^{(2)}$ are the same as those of the previous example. For the case of all-to-all couplings, we can again define two effective diffusion coefficients

$$\mathcal{D}_u^{\mathrm{a2a}} = D_u^{(1)} + (N-2)r_2 D_u^{(2)} \text{ and } \mathcal{D}_v^{\mathrm{a2a}} = D_v^{(1)} + (N-2)r_2 D_v^{(2)}, \quad (4.31)$$

so to write Eqs. (4.30) as

$$\delta\dot{\mathbf{x}} = \left[\mathbb{I}_N \otimes \mathbf{JF} - \sigma_1 \mathbf{L}^{(1)} \otimes \mathcal{JH}^{\mathrm{a2a}} \right] \delta\mathbf{x}, \qquad (4.32)$$

where

$$\mathcal{JH}^{\mathrm{a2a}} = \mathbf{JH}^{(1)} + (N-2)r_2\mathbf{JH}^{(2)} = 3 \begin{pmatrix} \mathcal{D}_u^{\mathrm{a2a}} & 0 \\ 0 & \mathcal{D}_v^{\mathrm{a2a}} \left(\frac{b}{c} \right)^2 \end{pmatrix}. \qquad (4.33)$$

As for the 2-lattice, Eqs. (4.32) have the same form of Eqs. (4.6), which have been derived accounting for pairwise interactions only. Hence, conditions (4.17) are again written in terms of effective diffusion coefficients, in this case $\mathcal{D}_u^{\mathrm{a2a}}$ and $\mathcal{D}_v^{\mathrm{a2a}}$. We thus have

$$\begin{cases} (b-1)b^2\mathcal{D}_v^{\mathrm{a2a}} - c^3\mathcal{D}_u^{\mathrm{a2a}} > 0, \\ 4b^2c^3\mathcal{D}_u^{\mathrm{a2a}}\mathcal{D}_v^{\mathrm{a2a}} - \left[(b-1)b^2\mathcal{D}_v^{\mathrm{a2a}} - c^3\mathcal{D}_u^{\mathrm{a2a}} \right]^2 < 0. \end{cases} \qquad (4.34)$$

As for Eq. (4.28), conditions (4.34) depend on the ratio $r_2 = \sigma_2/\sigma_1$ through the effective diffusion coefficients $\mathcal{D}_u^{\mathrm{a2a}}$, $\mathcal{D}_v^{\mathrm{a2a}}$. However, it is worth remarking that differently from the case of the 2-lattice, conditions (4.34)
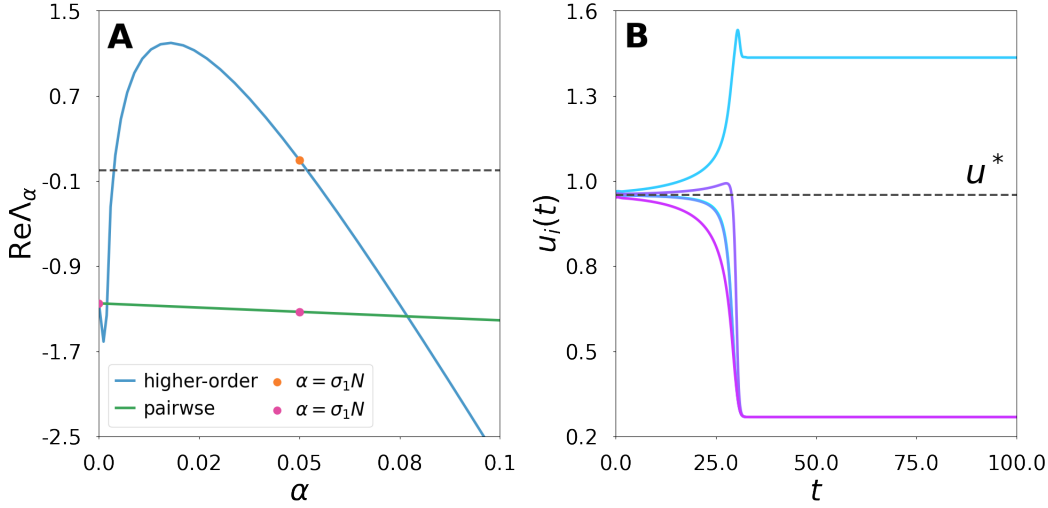
Figure 4.5: Formation of Turing patterns on the all-to-all simplicial complex of $N = 5$ nodes. Panel A displays the dispersion relations $\text{Re}(\Lambda_\alpha)$ associated to (4.20) (pairwise coupling only, continuous green line) and to system (4.22) (higher-order coupling, continuous blue line), as well as their value for $\alpha = \sigma_1 N$ (orange and pink dots respectively). Panel B shows the formation of Turing patterns on the u-component in the dynamics of (4.22), simulated on the all-to-all higher-order structure. The panels are obtained by setting the Brusselator parameters to $b = 5.5$, and $c = 7$, the pairwise diffusion coefficients to $D_u^{(1)} = 1$, and $D_v^{(1)} = 0.1$, the three-body diffusion coefficients to $D_u^{(2)} = 0.07$, and $D_v^{(2)} = 1$, and the coupling strengths to $\sigma_1 = 0.01$ and $\sigma_2 = 1$.

also depend on the number of nodes N. Lastly, we can then derive a necessary condition on the diffusive coefficients for the formation of Turing patterns, namely

$$b^2(D_v^{(1)} + (N-2)r_2 D_v^{(2)}) > c^2(D_u^{(1)} + (N-2)r_2 D_u^{(2)}). \qquad (4.35)$$

As an example, we analyze a configuration for which the higher-order interactions induce the emergence of Turing patterns, assuming that no patterns are formed when considering pairwise interactions only. We set the parameters of the Brusselator model to $b = 5.5$, and $c = 7$, the pairwise diffusion coefficients to $D_u^{(1)} = 1$, and $D_v^{(1)} = 0.1$, the higher-order

coefficients to $D_u^{(2)} = 0.07$, and $D_v^{(2)} = 1$, while the coupling strengths are fixed to $\sigma_1 = 0.01$ and $\sigma_2 = 1$, so that $r_2 = 100$. As regards the topology, we consider the all-to-all simplicial complex of $N = 5$ nodes. With this setting, conditions (4.17) do not hold, whereas conditions (4.34) do, meaning that Turing patterns can only form in presence of three-body interactions. The results obtained when accounting for either the sole two-body interactions or two-body and three-body interactions together are shown in Panel A of Fig. 4.5. We note that while the dispersion relation associated to (4.15) lies entirely below the axis $\text{Re}\Lambda_\alpha = 0$ (green line), the one associated to system (4.22) crosses the axis (blue line), which means that Turing patterns could emerge with the higher-order interactions active. The orange and the pink dots represent the values of $\text{Re}\Lambda_\alpha$ for $\alpha = \{0, \sigma_1 N\}$, being $\lambda_i^{(1)} = N$ the only nonzero eigenvalue of the standard Laplacian matrix in the all-to-all configuration. Such a value of α leads to $\text{Re}\Lambda_\alpha > 0$, so Turing patterns can form on the higher-order structure. As done before, we confirm this by simulating the dynamics of system (4.22), which is shown in panel B of Fig. 4.5. We observe that patterns are formed, as each u_i diverges from the equilibrium point $u^* = 1$. The dynamics of u_i are obtained by fixing an initial condition close to the equilibrium point $[u^*, v^*]^T$, and integrating Eq. (4.22) using a Runge-Kutta fourth-order method with integration time step $dt = 5 \cdot 10^{-3}$. The initial conditions are generated by perturbing the fixed point with a random perturbation of size 10^{-2}.

4.4   The general setting

In this last section, we concentrate on the most general setting of the problem, in which the Laplacian matrices associated to each order of interaction do not commute, and in which the coupling functions do not satisfy the natural coupling hypothesis. As discussed in Sec. 1.3, in this case it is not possible to derive analytically a dispersion relation that determines the stability of the system. However, it is still possible to analyze the conditions under which Turing patterns form numerically. In particular, we are here interested in studying how the presence of higher-order terms impact the emergence of patterns.

We consider a system of N Brusselator models, coupled through cubic diffusive-like interaction functions, with no cross-diffusion terms. For pairwise interactions we take $\mathbf{h}^{(1)}(u_j, v_j) = [D_u^{(1)} h_u^{(1)}(u_j), D_v^{(1)} h_v^{(1)}(v_j)]^T$, with $h_u^{(1)}(u_j) = u_j^3$ and $h_v^{(1)}(v_j) = v_j^3$, while for higher-order interactions we use $\mathbf{h}^{(2)}(u_j, v_j, u_k, v_k) = [D_u^{(2)} h_u^{(2)}(u_j, u_k), D_v^{(2)} h_v^{(2)}(v_j, v_k)]^T$, where we have $h_u^{(2)}(u_j, u_k) = u_j^2 u_k$ and $h_v^{(2)}(v_j, v_k) = v_j^2 v_k$, while we do not consider terms of order $D > 2$. Differently from the cases analyzed previously, we consider cases where $D_u^{(1)} \neq D_u^{(2)}$ and $D_v^{(1)} \neq D_v^{(2)}$, so that the natural coupling hypothesis does not hold, and account for an arbitrary higher-order structure, whose associated Laplacian matrices do not commute. In particular, we will consider the system to be arranged according to the hypergraph displayed in Fig. 4.1. The equations governing the dynamics of the system are formally equivalent to Eqs. (4.22), though the adjacency matrix $\mathbf{A}^{(1)}$ and the adjacency tensor $\mathbf{A}^{(2)}$ are those associated to the hypergraph in Fig. 4.1.

In this section, we are interested in studying whether higher-order interactions favor the formation of Turing patterns. In particular, we analyze if the region of the model parameters (b, c) for which the homogeneous solution is unstable can be expanded when considering three-body interactions. To begin with, we consider a setting for which Turing patterns can not emerge when considering two-body interactions only. We fix the pairwise diffusion coefficients to $D_u^{(1)} = 1$, and $D_v^{(1)} = 0.5$, the higher-order coefficients to $D_u^{(2)} = 0.1$, and $D_v^{(2)} = 2$, while the coupling strengths are fixed to $\sigma_1 = 0.1$ and $\sigma_2 = 1$. Note that conditions (4.17) never hold for any value of b and c, so pairwise interactions are not sufficient to yield the formation of patterns. In this setting, we integrate Eqs. (4.22) for different values of the Brusselator paramaters b and c, and we study the stability of the equilibrium point $[u^*, v^*]^T = [1, b/c]$. To assess the state of the system, we monitor the pattern amplitude of the stationary state [67], given by

$$A = \left\{ \sum_{i=1}^{N} \left[(u_i(\tau) - u^*)^2 + (v_i(\tau) - v^*)^2 \right] \right\}^{\frac{1}{2}}, \qquad (4.36)$$

where τ is a sufficiently large value of time for which the system has
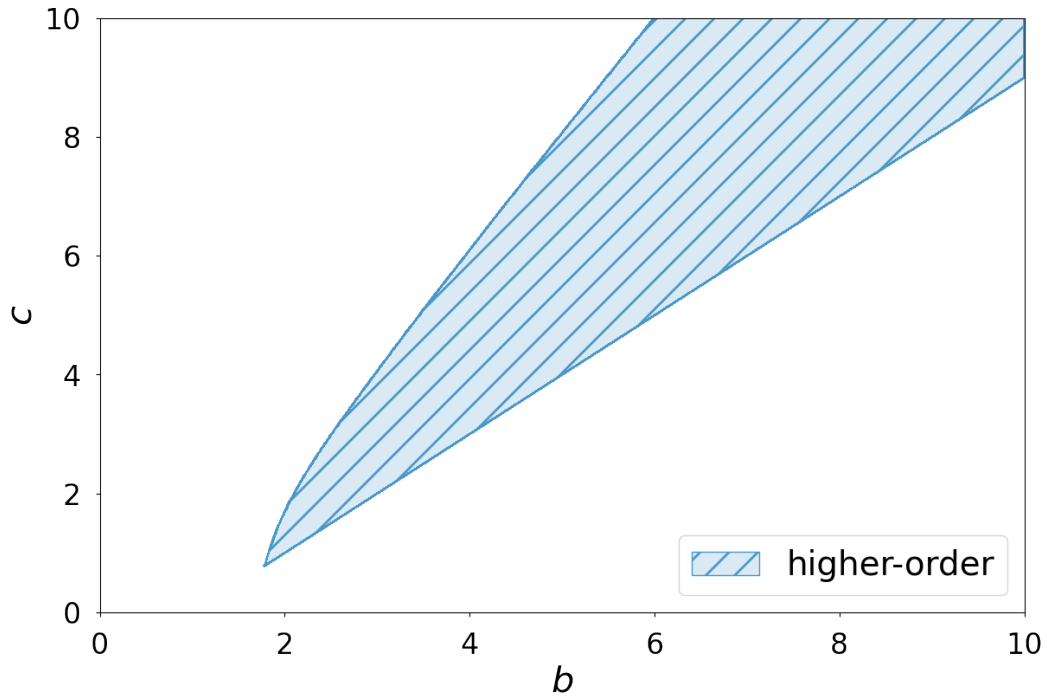
Figure 4.6: Instability region of the equilibrium point $[u^*, v^*]^T$ in the plane (b, c) for a system with higher-order interactions. The hatched blue area corresponds to the values of the Brusselator parameters where the pattern amplitude A is different from zero, while the white area corresponds to the region where $A = 0$. The two-body diffusion coefficients are set to $D_u^{(1)} = 1$, and $D_v^{(1)} = 0.5$, the three-body diffusion coefficients to $D_u^{(2)} = 0.1$, and $D_v^{(2)} = 2$, while the coupling strengths to $\sigma_1 = 0.1$ and $\sigma_2 = 1$.

reached a stationary state. For the present analysis, we integrate the system equations using a Runge-Kutta fourth-order method with integration time step $dt = 5 \cdot 10^{-3}$, for a time interval of length τ, where $\tau = 50$. The results obtained are shown in Fig. 4.6. Here, the hatched blue area corresponds to the region of the plane (b, c) for which the pattern amplitude A is different from zero, namely the parameter sets for which Turing patterns emerge, while the white area corresponds to the region where $A = 0$. The existence of such an area testifies that the presence of three-body interactions yields the formation of patterns, whereas the
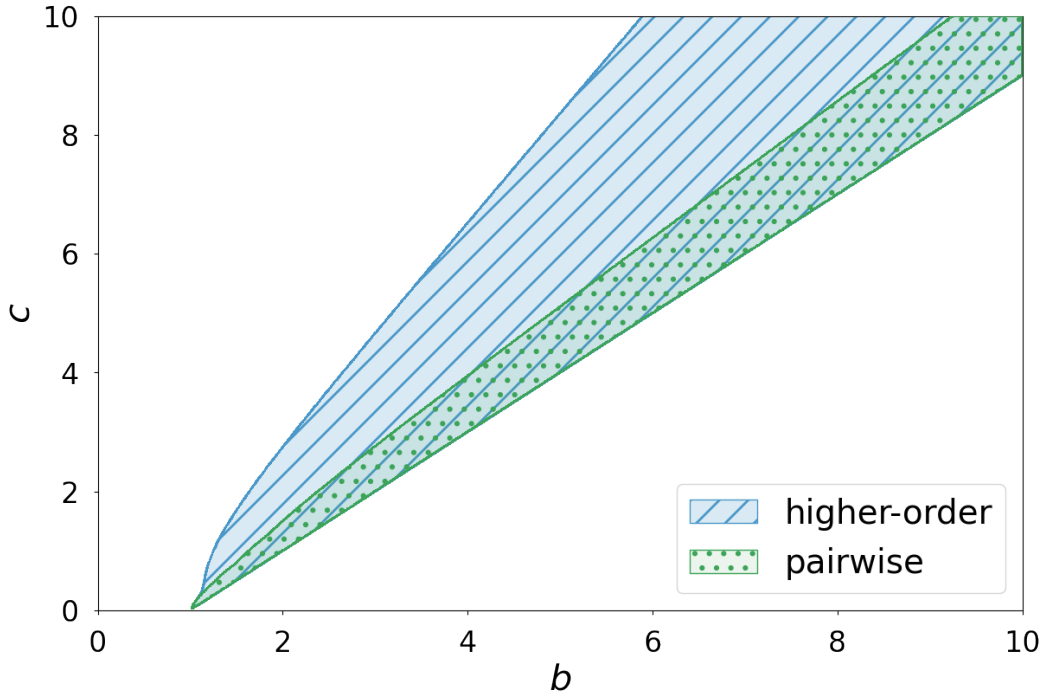
Figure 4.7: Expansion of the instability region of the equilibrium point $[u^*, v^*]^T$ in the plane (b, c) due to higher-order interactions. The hatched areas correspond to the values of the Brusselator parameters where the pattern amplitude A is different from zero. In green, it is represented the case of a system where only pairwise interactions are active, while the blue area refers to the case where both pairwise and higher-order interactions are considered. The white area corresponds to the region where $A = 0$. The two-body diffusion coefficients are set to $D_u^{(1)} = 0.1$, and $D_v^{(1)} = 0.5$, the three-body diffusion coefficients to $D_u^{(2)} = 0.01$, and $D_v^{(2)} = 1$, while the coupling strengths to $\sigma_1 = 0.2$ and $\sigma_2 = 1$.

sole two-body interactions do not allow for the onset of Turing instability. Hence, higher-order interactions can make Turing patterns emerge. More in general, higher-order terms can enlarge the region of instability in the space of parameters. To show this, we consider a new setting for which two-body interactions admit the formation of Turing patterns. In particular, we fix the pairwise diffusion coefficients to $D_u^{(1)} = 0.1$, and

$D_v^{(1)} = 0.5$, the higher-order coefficients to $D_u^{(2)} = 0.01$, and $D_v^{(2)} = 1$, while the coupling strengths are fixed to $\sigma_1 = 0.2$ and $\sigma_2 = 1$. With this configuration, conditions (4.17) hold for a few values of the Brusselator model parameters. Again, we integrate Eqs. (4.22) for different values of b and c, and we analyze the emergence of patterns by monitoring the pattern amplitude A. The results of such an analysis are shown in Fig. 4.7. Here, the hatched areas corresponds to the regions of the plane (b, c) for which $A \neq 0$, when considering pairwise couplings only (in green) or both pairwise and higher-order couplings (in blue), while the white area corresponds to the region where $A = 0$. We observe that three-body interactions favor the formation of Turing patterns, as their presence expand the parameter region for which the homogeneous solution $[u^*, v^*]^T$ is unstable. We conclude by remarking that, in analogy with the examples presented in the previous sections, it would be possible to find settings such that high-order interactions hamper the formation of Turing patterns, though not explicitly presented in this work.

In conclusion, the analyses presented in this chapter confirm the potential of our mathematical framework for studying the role of higher-order interactions in Turing pattern formation. We have explored how the presence of higher-order couplings modifies the conditions for the emergence of patterns. In particular, we have derived a new set of conditions in the special case of coupling functions respecting the natural coupling hypothesis, and in that of some higher-order topologies whose associated Laplacian matrices commute. For these latter, we have found that when considering general higher-order interaction functions the formation of Turing patterns depend on their relative strength, so that many-body interactions can either favor or prevent the emergence of patterns. Lastly, we have provided a few results relaxing the hypothesis on the coupling functions and on the interaction structure, showing how higher-order interactions can enlarge the region of Turing instability.

Conclusions

Some of the most fascinating and complex phenomena in nature emerge from the interactions among simple units. With this thesis, we provide our contribution to the study of complex systems and emergent collective behaviors. In particular, we have here formulated a general theory to characterize the dynamics of systems of coupled units, interacting not only via two-body interactions, but also through many-body interactions.

Specifically, we have described how to represent systems characterized by higher-order interactions using a graph theoretical approach. We have presented two higher-order network representations, i.e., simplicial complexes and hypergraphs, and we have introduced the main metrics for encoding their structure. In this context, we have developed a mathematical framework useful to investigate two emergent phenomena of major interest for various research fields, namely the synchronization of coupled oscillators, and the formation of patterns in reaction-diffusion systems. We have shown how these problem can be analyzed under the frame of a linear stability problem, extending to the case of higher-order structures both the Master Stability Function approach for synchronization, and Turing's instability theory for pattern formation.

With respect to synchronization, we have investigated under which conditions a system of coupled chaotic oscillators achieves a coherent state in presence of reciprocal many-body interactions. In particular, we have pointed out the role of higher-order couplings, showing, for instance, how they may enhance synchronization of neural activity, paving the way for future research on the topic. Furthermore, we have examined

the synchronizability of higher-order topologies, showing how many-body interactions can either be beneficial or detrimental for synchronization, with respect to the form of the coupling. We have concluded the analysis of reciprocal higher-order interactions by comparing simplicial complexes and hypergraphs, showing how their different structural features may impact the synchronization behavior of the system.

We have then studied the case of nonreciprocal higher-order interactions, showing how the presence of a privileged direction in the interaction may affect the synchronization behavior of a system of coupled chaotic oscillators. Specifically, we have demonstrated how directionality in hypergraphs can dramatically impact the dynamics of the system, either inducing its synchronization or the loss of coherence. Moreover, with the support of few results on random hypergraphs, we have shown how different topologies may be differently affected by the presence of non-reciprocal interactions. These results shed further light on the interplay between structural and dynamical features in the onset of synchronization.

With regards to Turing's instability theory, we have analyzed the conditions for the formation of patterns in higher-order reaction-diffusion systems. In particular, we have scrutinized the case of a system of Brusselators, a prototypical model for autocatalytic reactions, coupled through higher-order, nonlinear, diffusive-like functions. We have shown that many-body interactions can highly affect the conditions under which patterns emerge, either allowing them in cases where the sole pairwise diffusion is not sufficient, or impeding their formation in the opposite situation. The necessary conditions for which these opposite scenarios occur have been derived analytically for various topologies, and with different assumptions on the diffusion functions. In particular, in agreement with Turing's theory, we have demonstrated how the system behaviors ultimately depends on the relative strength of the diffusion coefficients, both pairwise and higher-order. Such a general theory paves the way for further studies on pattern formation in presence of higher-order interactions.

Our results lay the groundwork for new research on how complex, collective behaviors emerge from systems of interacting units. For instance, future studies can aim at using our formalism to analyze other

kinds of phenomena, such as cluster synchronization, Chimera states, and so on. Though the last years have witnessed a few attempts to extend the results obtained for networks [163], we believe the possibilities related to these research questions are substantial. Another interesting issue is whether higher-order interactions promote either synchronization or pattern formation [164]. A complete picture on this subject is still lacking, although the results here presented provide a few possible research directions. Then, there is the question of what structures are optimal for synchronization, a problem deeply studied for complex networks [142, 165], but still largely unexplored for higher-order topologies [166]. From that, it naturally follows the problem of controlling the dynamics of a system in presence of higher-order interactions, an aspect of potentially great interests in many research fields.

To properly answer these and other questions, we believe a few steps have to be taken, which may require to go beyond the mathematical framework presented in this thesis. First, we think it is crucial to fully understand if and how the two higher-order structures presented in this work, namely simplicial complexes and hypergraphs, yield different emerging collective behaviors. Second, to entirely grasp the role of many-body interactions in the dynamics of coupled systems, it may be necessary to develop methods that go beyond what we could define "the graph projection" of higher-order structure, namely beyond the linear stability analysis. A few crucial attempts in both directions have been already made [164, 167], but again, further research are needed.

Bibliography

[1] Stefano Boccaletti, Vito Latora, Yamir Moreno, Martin Chavez, and D-U Hwang, Physics reports **424**, 175 (2006).

[2] Luıs A Nunes Amaral, Antonio Scala, Marc Barthelemy, and H Eugene Stanley, Proceedings of the national academy of sciences **97**, 11149 (2000).

[3] Ian Dobson, Benjamin A Carreras, Vickie E Lynch, and David E Newman, Chaos: An Interdisciplinary Journal of Nonlinear Science **17**, 026103 (2007).

[4] Michalis Faloutsos, Petros Faloutsos, and Christos Faloutsos, ACM SIGCOMM computer communication review **29**, 251 (1999).

[5] Francisco Varela, Jean-Philippe Lachaux, Eugenio Rodriguez, and Jacques Martinerie, Nature reviews neuroscience **2**, 229 (2001).

[6] John Scott, Sociology **22**, 109 (1988).

[7] Stanley Wasserman, Katherine Faust, et al., (1994).

[8] Mark EJ Newman, SIAM review **45**, 167 (2003).

[9] Vito Latora, Vincenzo Nicosia, and Giovanni Russo, *Complex networks: principles, methods and applications* (Cambridge University Press, ADDRESS, 2017).

[10] Mark Newman, *Networks* (Oxford university press, ADDRESS, 2018).

[11] Philip W Anderson, Science **177**, 393 (1972).

[12] Mark A Bedau and Paul Ed Humphreys, *Emergence: Contemporary readings in philosophy and science.* (MIT press, ADDRESS, 2008).

[13] Benjamin Sacépé and Mikhail Feigel'man, .

[14] Michael E McHenry and David E Laughlin, *Physical Metallurgy* (Elsevier, ADDRESS, 2014), pp. 1881–2008.

[15] Thomas Caraco, Steven Martindale, and H Ronald Pulliam, Nature **285**, 400 (1980).

[16] Romualdo Pastor-Satorras, Claudio Castellano, Piet Van Mieghem, and Alessandro Vespignani, Reviews of modern physics **87**, 925 (2015).

[17] Oriol Artime and Manlio De Domenico, From the origin of life to pandemics: emergent phenomena in complex systems, 2022.

[18] Steven Strogatz, (2004).

[19] Serguei Saavedra, Kathleen Hagerty, and Brian Uzzi, Proceedings of the National Academy of Sciences **108**, 5296 (2011).

[20] Steven H Strogatz, Daniel M Abrams, Allan McRobie, Bruno Eckhardt, and Edward Ott, Nature **438**, 43 (2005).

[21] Zoltán Néda, Erzsébet Ravasz, Yves Brechet, Tamás Vicsek, and A-L Barabási, Nature **403**, 849 (2000).

[22] Akito Miura, Kazutoshi Kudo, Tatsuyuki Ohtsuki, and Hiroaki Kanehisa, Human movement science **30**, 1260 (2011).

[23] Werner Goebl and Caroline Palmer, Music Perception **26**, 427 (2009).

[24] Shir Shahal, Ateret Wurzberg, Inbar Sibony, Hamootal Duadi, Elad Shniderman, Daniel Weymouth, Nir Davidson, and Moti Fridman, Nature communications **11**, 1 (2020).

[25] Adilson E Motter, Seth A Myers, Marian Anghel, and Takashi Nishikawa, Nature Physics **9**, 191 (2013).

[26] Mattia Frasca, Lucia Valentina Gambuzza, Arturo Buscarino, and Luigi Fortuna, *Synchronization in networks of nonlinear circuits: Essential topics with MATLAB® code* (Springer, ADDRESS, 2018).

[27] Jürgen Kurths Arkady Pikovsky, Michael Rosenblum, *Synchronization. A universal concept in nonlinear sciences*, *Cambridge Nonlinear Science Series*, 1 ed. (Cambridge University Press, ADDRESS, 2001).

[28] Mauricio Barahona and Louis M Pecora, Physical review letters **89**, 054101 (2002).

[29] M Chavez, D-U Hwang, Arno Amann, HGE Hentschel, and Stefano Boccaletti, Physical Review Letters **94**, 218701 (2005).

[30] D-U Hwang, M Chavez, A Amann, and S Boccaletti, Physical review letters **94**, 138701 (2005).

[31] Stefano Boccaletti, D-U Hwang, Mario Chavez, Andreas Amann, Jürgen Kurths, and Louis M Pecora, Physical Review E **74**, 016102 (2006).

[32] Charo I Del Genio, Jesús Gómez-Gardeñes, Ivan Bonamassa, and Stefano Boccaletti, Science Advances **2**, e1601679 (2016).

[33] Ricardo Gutiérrez, Andreas Amann, Salvatore Assenza, Jesús Gómez-Gardenes, V Latora, and Stefano Boccaletti, Physical review letters **107**, 234103 (2011).

[34] Vanesa Avalos-Gaytán, Juan A Almendral, I Leyva, F Battiston, V Nicosia, V Latora, and S Boccaletti, Physical Review E **97**, 042301 (2018).

[35] Lucia Valentina Gambuzza, Alessio Cardillo, Alessandro Fiasconaro, Luigi Fortuna, Jesus Gómez-Gardenes, and Mattia Frasca, Chaos: An Interdisciplinary Journal of Nonlinear Science **23**, 043103 (2013).

[36] Vincenzo Nicosia, Miguel Valencia, Mario Chavez, Albert Díaz-Guilera, and Vito Latora, Physical review letters **110**, 174102 (2013).

[37] Louis M Pecora, Francesco Sorrentino, Aaron M Hagerstrom, Thomas E Murphy, and Rajarshi Roy, Nature communications **5**, 1 (2014).

[38] Francesco Sorrentino, Louis M Pecora, Aaron M Hagerstrom, Thomas E Murphy, and Rajarshi Roy, Science advances **2**, e1501737 (2016).

[39] Daniel M Abrams and Steven H Strogatz, Physical review letters **93**, 174102 (2004).

[40] Mark J Panaggio and Daniel M Abrams, Nonlinearity **28**, R67 (2015).

[41] Hongjie Bi, Xin Hu, S Boccaletti, Xingang Wang, Yong Zou, Zonghua Liu, and Shuguang Guan, Physical review letters **117**, 204101 (2016).

[42] Can Xu, Stefano Boccaletti, Shuguang Guan, and Zhigang Zheng, Physical Review E **98**, 050202 (2018).

[43] Hiroya Nakao, The European Physical Journal Special Topics **223**, 2411 (2014).

[44] Francesca Di Patti, Duccio Fanelli, Filippo Miele, and Timoteo Carletti, Chaos, Solitons & Fractals **96**, 8 (2017).

[45] Deniz Eroglu, Jeroen SW Lamb, and Tiago Pereira, Contemporary Physics **58**, 207 (2017).

[46] Louis M Pecora and Thomas L Carroll, Physical review letters **64**, 821 (1990).

[47] Michael G Rosenblum, Arkady S Pikovsky, and Jürgen Kurths, Physical review letters **76**, 1804 (1996).

[48] Louis M Pecora and Thomas L Carroll, Physical review letters **80**, 2109 (1998).

[49] Liang Huang, Qingfei Chen, Ying-Cheng Lai, and Louis M Pecora, Physical Review E **80**, 036204 (2009).

[50] James D Murray, *Mathematical biology II: spatial models and biomedical applications* (Springer New York, ADDRESS, 2001), Vol. 3.

[51] Alan Mathison Turing, Bulletin of mathematical biology **52**, 153 (1990).

[52] Shigeru Kondo and Takashi Miura, science **329**, 1616 (2010).

[53] Nature Computational Science **2**, 463 (2022).

[54] Ilya Prigogine and René Lefever, The Journal of Chemical Physics **48**, 1695 (1968).

[55] Vincent Castets, Etiennette Dulos, Jacques Boissonade, and Patrick De Kepper, Physical review letters **64**, 2953 (1990).

[56] Qi Ouyang and Harry L Swinney, Nature **352**, 610 (1991).

[57] Hans Meinhardt and Alfred Gierer, Bioessays **22**, 753 (2000).

[58] Matthew P Harris, Scott Williamson, John F Fallon, Hans Meinhardt, and Richard O Prum, Proceedings of the National Academy of Sciences **102**, 11734 (2005).

[59] Philip K Maini, Ruth E Baker, and Cheng-Ming Chuong, Science **314**, 1397 (2006).

[60] Alistair Boettiger, Bard Ermentrout, and George Oster, Proceedings of the National Academy of Sciences **106**, 6837 (2009).

[61] Akiko Nakamasu, Go Takahashi, Akio Kanbe, and Shigeru Kondo, Proceedings of the National Academy of Sciences **106**, 8429 (2009).

[62] M Mimura and JD Murray, Journal of Theoretical Biology **75**, 249 (1978).

[63] John L Maron and Susan Harrison, Science **278**, 1619 (1997).

[64] Yuki Fuseya, Hiroyasu Katsuno, Kamran Behnia, and Aharon Kapitulnik, Nature Physics **17**, 1031 (2021).

[65] Alfred Gierer and Hans Meinhardt, Kybernetik **12**, 30 (1972).

[66] Hans G Othmer and LE Scriven, Journal of theoretical biology **32**, 507 (1971).

[67] Hiroya Nakao and Alexander S Mikhailov, Nature Physics **6**, 544 (2010).

[68] Romualdo Pastor-Satorras and Alessandro Vespignani, Nature Physics **6**, 480 (2010).

[69] Malbor Asllani, Joseph D Challenger, Francesco Saverio Pavone, Leonardo Sacconi, and Duccio Fanelli, Nature communications **5**, 1 (2014).

[70] Malbor Asllani, Timoteo Carletti, Duccio Fanelli, and Philip K Maini, The European Physical Journal B **93**, 1 (2020).

[71] Riccardo Muolo, Malbor Asllani, Duccio Fanelli, Philip K Maini, and Timoteo Carletti, Journal of theoretical biology **480**, 81 (2019).

[72] Julien Petit, Ben Lauwens, Duccio Fanelli, and Timoteo Carletti, Physical review letters **119**, 148301 (2017).

[73] Malbor Asllani, Daniel M Busiello, Timoteo Carletti, Duccio Fanelli, and Gwendoline Planchon, Physical Review E **90**, 042814 (2014).

[74] Nikos E Kouvaris, Shigefumi Hata, and Albert Díaz Guilera, Scientific reports **5**, 1 (2015).

[75] Jonathan M Levine, Jordi Bascompte, Peter B Adler, and Stefano Allesina, Nature **546**, 56 (2017).

[76] Elad Ganmor, Ronen Segev, and Elad Schneidman, Proceedings of the National Academy of sciences **108**, 9679 (2011).

[77] Giovanni Petri, Paul Expert, Federico Turkheimer, Robin Carhart-Harris, David Nutt, Peter J Hellyer, and Francesco Vaccarino, Journal of The Royal Society Interface **11**, 20140873 (2014).

[78] Ann E Sizemore, Chad Giusti, Ari Kahn, Jean M Vettel, Richard F Betzel, and Danielle S Bassett, Journal of computational neuroscience **44**, 115 (2018).

[79] Alice Patania, Giovanni Petri, and Francesco Vaccarino, EPJ Data Science **6**, 1 (2017).

[80] Pavel S Aleksandrov, *Combinatorial topology* (Courier Corporation, ADDRESS, 1998), Vol. 1.

[81] Claude Berge, (1973).

[82] Federico Battiston, Giulia Cencetti, Iacopo Iacopini, Vito Latora, Maxime Lucas, Alice Patania, Jean-Gabriel Young, and Giovanni Petri, Physics Reports **874**, 1 (2020).

[83] Federico Battiston and Giovanni Petri, Higher-Order Systems, 2022.

[84] Guillaume St-Onge, Hanlin Sun, Antoine Allard, Laurent Hébert-Dufresne, and Ginestra Bianconi, Physical Review Letters **127**, 158301 (2021).

[85] Iacopo Iacopini, Giovanni Petri, Alain Barrat, and Vito Latora, Nature communications **10**, 1 (2019).

[86] Guilherme Ferraz de Arruda, Giovanni Petri, and Yamir Moreno, Physical Review Research **2**, 023032 (2020).

[87] Iacopo Iacopini, Giovanni Petri, Andrea Baronchelli, and Alain Barrat, Communications Physics **5**, 1 (2022).

[88] Michael T Schaub, Austin R Benson, Paul Horn, Gabor Lippner, and Ali Jadbabaie, SIAM Review **62**, 353 (2020).

[89] Timoteo Carletti, Federico Battiston, Giulia Cencetti, and Duccio Fanelli, Physical review E **101**, 022308 (2020).

[90] Timoteo Carletti, Duccio Fanelli, and Renaud Lambiotte, Journal of Physics: Complexity **2**, 015011 (2021).

[91] Leonie Neuhäuser, Andrew Mellor, and Renaud Lambiotte, Physical Review E **101**, 032310 (2020).

[92] Leonie Neuhäuser, Renaud Lambiotte, and Michael T Schaub, *Higher-Order Systems* (Springer, ADDRESS, 2022), pp. 347–376.

[93] Christian Kuehn and Christian Bick, Science advances **7**, eabe3824 (2021).

[94] Federico Battiston, Enrico Amico, Alain Barrat, Ginestra Bianconi, Guilherme Ferraz de Arruda, Benedetta Franceschiello, Iacopo Iacopini, Sonia Kéfi, Vito Latora, Yamir Moreno, et al., Nature Physics **17**, 1093 (2021).

[95] Megan Wang, Daniel Arteaga, and Biyu J He, Proceedings of the National Academy of Sciences **110**, E3350 (2013).

[96] R David Andrew, Mitchell Fagan, Barbara A Ballyk, and Andrei S Rosen, Brain research **498**, 175 (1989).

[97] Damon Centola, Joshua Becker, Devon Brackbill, and Andrea Baronchelli, Science **360**, 1116 (2018).

[98] Yoshiki Kuramoto, *Chemical oscillations, waves, and turbulence* (Springer, ADDRESS, 1984), pp. 111–140.

[99] Per Sebastian Skardal and Alex Arenas, Physical review letters **122**, 248301 (2019).

[100] Takuma Tanaka and Toshio Aoyagi, Physical Review Letters **106**, 224101 (2011).

[101] Per Sebastian Skardal and Alex Arenas, Communications Physics **3**, 1 (2020).

[102] Ana P Millán, Joaquín J Torres, and Ginestra Bianconi, Physical Review Letters **124**, 218301 (2020).

[103] Reza Ghorbanchian, Juan G Restrepo, Joaquín J Torres, and Ginestra Bianconi, Communications Physics **4**, 1 (2021).

[104] A Krawiecki, Chaos, Solitons & Fractals **65**, 44 (2014).

[105] Maxime Lucas, Giulia Cencetti, and Federico Battiston, Physical Review Research **2**, 033410 (2020).

[106] Timoteo Carletti, Lorenzo Giambagli, and Ginestra Bianconi, arXiv preprint arXiv:2208.14783 (2022).

[107] Timoteo Carletti, Duccio Fanelli, and Sara Nicoletti, Journal of Physics: Complexity **1**, 035006 (2020).

[108] Lorenzo Giambagli, Lucille Calmon, Riccardo Muolo, Timoteo Carletti, and Ginestra Bianconi, arXiv preprint arXiv:2207.07787 (2022).

[109] Guilherme Ferraz de Arruda, Michele Tizzani, and Yamir Moreno, Communications Physics **4**, 1 (2021).

[110] Ana Paula Millán, Juan G Restrepo, Joaquín J Torres, and Ginestra Bianconi, *Higher-Order Systems* (Springer, ADDRESS, 2022), pp. 269–299.

[111] Reza Olfati Saber and Richard M Murray, (2003).

[112] Alain Barrat, Marc Barthelemy, and Alessandro Vespignani, *Dynamical processes on complex networks* (Cambridge university press, ADDRESS, 2008).

[113] Sergio Barbarossa and Mikhail Tsitsvero, in *2016 IEEE International Conference on Acoustics, Speech and Signal Processing (ICASSP)*, IEEE (PUBLISHER, ADDRESS, 2016), pp. 6425–6429.

[114] Sergio Barbarossa and Stefania Sardellitti, IEEE Transactions on Signal Processing **68**, 2992 (2020).

[115] Fan Chung, Expanding graphs (DIMACS series) 21 (1993).

[116] Linyuan Lu and Xing Peng, in *International Workshop on Algorithms and Models for the Web-Graph*, Springer (PUBLISHER, ADDRESS, 2011), pp. 14–25.

[117] Solomon E Asch, Organizational influence processes **58**, 295 (1951).

[118] Steffen Klamt, Utz-Uwe Haus, and Fabian Theis, PLoS computational biology **5**, e1000385 (2009).

[119] Athel Cornish-Bowden, *Fundamentals of enzyme kinetics* (John Wiley & Sons, ADDRESS, 2013).

[120] Eric D Kelsic, Jeffrey Zhao, Kalin Vetsigian, and Roy Kishony, Nature **521**, 516 (2015).

[121] Monica I Abrudan, Fokko Smakman, Ard Jan Grimbergen, Sanne Westhoff, Eric L Miller, Gilles P Van Wezel, and Daniel E Rozen, Proceedings of the National Academy of Sciences **112**, 11054 (2015).

[122] Jürgen Jost and Raffaella Mulas, Advances in mathematics **351**, 870 (2019).

[123] Eleonora Andreotti and Raffaella Mulas, arXiv preprint arXiv:2005.14484 **9**, (2020).

[124] Aida Abiad, Raffaella Mulas, and Dong Zhang, Linear Algebra and its Applications **629**, 192 (2021).

[125] Giorgio Ausiello, Alessandro D'Atri, and Domenico Sacca, Journal of the ACM (JACM) **30**, 752 (1983).

[126] Giorgio Gallo, Giustino Longo, Stefano Pallottino, and Sang Nguyen, Discrete applied mathematics **42**, 177 (1993).

[127] Giorgio Ausiello and Luigi Laura, Theoretical Computer Science **658**, 293 (2017).

[128] Giorgio Gallo and Maria Grazia Scutella, Rivista di matematica per le scienze economiche e sociali **21**, 97 (1998).

[129] Giorgio Gallo and Giampaolo Urbani, The Journal of Logic Programming **7**, 45 (1989).

[130] Daniele Pretolani, European Journal of Operational Research **123**, 315 (2000).

[131] Effat A Saied, Applied Mathematics and Computation **98**, 103 (1999).

[132] A Sadighi and DD Ganji, Computers & Mathematics with Applications **54**, 1112 (2007).

[133] James G Berryman and Charles J Holland, Physical Review Letters **40**, 1720 (1978).

[134] RM Cherniha and ND Cherniha, Journal of Physics A: Mathematical and General **26**, L935 (1993).

[135] Niraj Kumar and Werner Horsthemke, Physica A: Statistical Mechanics and its Applications **389**, 1812 (2010).

[136] G Gambino, MC Lombardo, Mml Sammartino, and V Sciacca, Physical Review E **88**, 042925 (2013).

[137] Niraj Kumar and Werner Horsthemke, Physical Review E **83**, 036105 (2011).

[138] Duccio Fanelli, Claudia Cianci, and Francesca Di Patti, The European Physical Journal B **86**, 1 (2013).

[139] Dibakar Ghosh, Mattia Frasca, Alessandro Rizzo, Soumen Majhi, Sarbendu Rakshit, Karin Alfaro-Bittner, and Stefano Boccaletti, Physics Reports **949**, 1 (2022).

[140] Francesco Sorrentino, New Journal of Physics **14**, 033035 (2012).

[141] Stefano Boccaletti, Ginestra Bianconi, Regino Criado, Charo I Del Genio, Jesús Gómez-Gardenes, Miguel Romance, Irene Sendina-Nadal, Zhen Wang, and Massimiliano Zanin, Physics reports **544**, 1 (2014).

[142] Takashi Nishikawa and Adilson E Motter, Physical Review E **73**, 065106 (2006).

[143] Otto E Rössler, Physics Letters A **57**, 397 (1976).

[144] James L Hindmarsh and RM Rose, Proceedings of the Royal society of London. Series B. Biological sciences **221**, 87 (1984).

[145] Edward N Lorenz, Journal of atmospheric sciences **20**, 130 (1963).

[146] Julien Clinton Sprott, *Chaos and time-series analysis* (Oxford university press Oxford, ADDRESS, 2003), Vol. 69.

[147] Timothy J Buschman, Eric L Denovellis, Cinira Diogo, Daniel Bullock, and Earl K Miller, Neuron **76**, 838 (2012).

[148] Premysl Jiruska, Marco De Curtis, John GR Jefferys, Catherine A Schevon, Steven J Schiff, and Kaspar Schindler, The Journal of physiology **591**, 787 (2013).

[149] Robert S Fisher, Carlos Acevedo, Alexis Arzimanoglou, Alicia Bogacz, J Helen Cross, Christian E Elger, Jerome Engel Jr, Lars Forsgren, Jacqueline A French, Mike Glynn, et al., Epilepsia **55**, 475 (2014).

[150] Viktor K Jirsa, William C Stacey, Pascale P Quilichini, Anton I Ivanov, and Christophe Bernard, Brain **137**, 2210 (2014).

[151] Chad Giusti, Robert Ghrist, and Danielle S Bassett, Journal of computational neuroscience **41**, 1 (2016).

[152] Paul Expert and Giovanni Petri, in *Higher-Order Systems*, edited by Federico Battiston and Giovanni Petri (Springer International Publishing, Cham, 2022), pp. 401–415.

[153] Mukeshwar Dhamala, Viktor K Jirsa, and Mingzhou Ding, Physical review letters **92**, 074104 (2004).

[154] Fatemeh Parastesh, Mahtab Mehrabbeik, Karthikeyan Rajagopal, Sajad Jafari, and Matjaž Perc, Chaos: An Interdisciplinary Journal of Nonlinear Science **32**, 013125 (2022).

[155] Alan Wolf, Jack B Swift, Harry L Swinney, and John A Vastano, Physica D: nonlinear phenomena **16**, 285 (1985).

[156] Bernadette CM Van Wijk, Cornelis J Stam, and Andreas Daffertshofer, PloS one **5**, e13701 (2010).

[157] Fabrizio De Vico Fallani, Martina Corazzol, Jenna R Sternberg, Claire Wyart, and Mario Chavez, IEEE Transactions on Neural Systems and Rehabilitation Engineering **23**, 333 (2014).

[158] Mark EJ Newman and Duncan J Watts, Physical review E **60**, 7332 (1999).

[159] Paul Erdős and Alfréd Rényi, Publ. Math. Inst. Hung. Acad. Sci **5**, 17 (1960).

[160] Ilya Prigogine and Grégoire Nicolis, The Journal of Chemical Physics **46**, 3542 (1967).

[161] Gregoire Nicolis, Dissipative Structures to Order through Fluctuations 339 (1977).

[162] Richard P Boland, Tobias Galla, and Alan J McKane, Journal of Statistical Mechanics: Theory and Experiment **2008**, P09001 (2008).

[163] Anastasiya Salova and Raissa M D'Souza, arXiv preprint arXiv:2101.05464 (2021).

[164] Yuanzhao Zhang, Maxime Lucas, and Federico Battiston, arXiv preprint arXiv:2203.03060 (2022).

[165] Joseph D Hart, Yuanzhao Zhang, Rajarshi Roy, and Adilson E Motter, Physical review letters **122**, 058301 (2019).

[166] Ying Tang, Dinghua Shi, and Linyuan Lü, Communications Physics **5**, 1 (2022).

[167] Anastasiya Salova and Raissa M D'Souza, arXiv preprint arXiv:2107.13712 (2021).

Appendix A

Other works

In this appendix we collect the abstracts of the articles and the preprints published during the three years of the PhD programme that have not find space in this PhD thesis. The first article deals with the problem of identifiability in epidemic models for COVID-19. In particular, we show how the choice of the model, in relation with the quantity and the quality of available empirical data, can affect the ability of making reliable predictions on the epidemics. The study of the forecasting capabilities of epidemic models is also a relevant topic of the second article. In this latter, we show that a model that accounts for the dynamical correlations of the spreading process can give better performances, as long as data from contact tracing are available. The last article presents MultiSAGE, an algorithm developed to embed multiplex networks in vectorial spaces, with potentially important applications in de-anonymization of users in online social networks.

A.1　Lack of practical identifiability may hamper reliable predictions in COVID-19 epidemic models

Compartmental models are widely adopted to describe and predict the spreading of infectious diseases. The unknown parameters of these models need to be estimated from the data. Furthermore, when some of the model variables are not empirically accessible, as in the case of asymptomatic carriers of coronavirus disease 2019 (COVID-19), they have to be obtained as an outcome of the model. Here, we introduce a framework to quantify how the uncertainty in the data affects the determination of the parameters and the evolution of the unmeasured variables of a given model. We illustrate how the method is able to characterize different regimes of identifiability, even in models with few compartments. Last, we discuss how the lack of identifiability in a realistic model for COVID-19 may prevent reliable predictions of the epidemic dynamics.

A.2 Individual-and pair-based models of epidemic spreading: Master equations and analysis of their forecasting capabilities

Epidemic models are crucial to understand how an infectious disease spreads in a population and to devise the best containment strategies. Compartmental models can provide a fine-grained description of the evolution of an epidemic when microscopic information on the network of contacts among individuals is available. However, coarser-grained descriptions prove also to be useful in many aspects. They allow to derive closed expressions for key parameters, such as the basic reproduction number, to understand the relationship between the model parameters, and also to derive fast and reliable predictions of macroscopic observables for a disease outbreak. The so-called population models can be developed at different levels of coarse-graining, so it is crucial to determine: (i) to which extent and how the existing correlations in the contact network have to be included in these models and (ii) what is their impact on the model ability to reproduce and predict the time evolution of the populations at the various stage of the disease. In this work, we address these questions through a systematic analysis of two discrete-time SEAIR (susceptible-exposed-asymptomatic-infected-recovered) population models: the first one developed assuming statistical independence at the level of individuals, and the other one assuming independence at the level of pairs. We provide a detailed derivation and analysis of both models, focusing on their capability to reproduce an epidemic process on different synthetic networks, and then comparing their predictions under scenarios of increasing complexity. We find that, although both models can fit the time evolution of the compartment populations obtained through microscopic simulations, the epidemic parameters adopted by the individual-based model for this purpose may significantly differ from those of the microscopic simulations. However, pair-based model provides not only more reliable predictions of the dynamical evolution of the variables but also a good estimation of the epidemic parameters. The difference between the two models is even more evident in the particularly challenging scenario when one or more variables are not measurable, and therefore

are not available for model tuning. This occurs for instance with asymptomatic infectious individuals in the case of COVID-19, an issue that has become extremely relevant during the recent pandemic. Under these conditions, the pairwise model again proves to perform much better than the individual-based representation, provided that it is fed with adequate information which, for instance, to be collected, may require a more detailed contact tracing. Overall, our results thus hallmark the importance of acquiring the proper empirical data to fully unfold the potentialities of models incorporating more sophisticated assumptions on the correlations among nodes in the contact network.

A.3   MultiSAGE: a multiplex embedding algorithm for inter-layer link prediction

Research on graph representation learning has received great attention in recent years. However, most of the studies so far have focused on the embedding of single-layer graphs. The few studies dealing with the problem of representation learning of multilayer structures rely on the strong hypothesis that the inter-layer links are known, and this limits the range of possible applications. Here we propose MultiSAGE, a generalization of the GraphSAGE algorithm that allows to embed multiplex networks. We show that MultiSAGE is capable to reconstruct both the intra-layer and the inter-layer connectivity, outperforming GraphSAGE, which has been designed for simple graphs. Next, through a comprehensive experimental analysis, we shed light also on the performance of the embedding, both in simple and in multiplex networks, showing that either the density of the graph or the randomness of the links strongly influences the quality of the embedding.

Appendix B

List of publications

[1] Gambuzza L.V., Di Patti F., **Gallo L.**, Lepri S., Romance M., Criado R., Frasca M., Latora V. & Boccaletti S., *Stability of synchronization in simplicial complexes*, Nature Communications, 12 (1), 1-13, (2021)

[2] **Gallo L.**, Muolo R., Gambuzza L.V., Latora V., Frasca M. & Carletti T., *Synchronization induced by directed higher-order interactions*, Communications Physics, 5, 263 (2022)

[3] Muolo R., **Gallo L.**, Latora V., Frasca M. & Carletti T., *Turing patterns in systems with high-order interactions*, arXiv:2207.03985 (2022)

[4] **Gallo L.**, Frasca M., Latora V. & Russo G., *Lack of practical identifiability may hamper reliable predictions in COVID-19 epidemic models*. Science Advances, **8**(3), eabg5234, (2022)

[5] Malizia F., **Gallo L.**, Frasca M., Latora V. & Russo G., *Individual- and pair-based models of epidemic spreading: Master equations and analysis of their forecasting capabilities*. Physical Review Research, **4**, 023145, (2022)

[6] **Gallo L.**, Latora V & Pulvirenti A., *MultiSAGE: a multiplex embedding algorithm for inter-layer link prediction*. arXiv preprint, arXiv:2206.13223 (2022)